# Flows in Films and Over Flippers

A dissertation presented
by

Ernst Adriaan van Nierop

to
the School of Engineering and Applied Sciences
in partial fulfillment of the requirements
for the degree of
Doctor of Philosophy
in the subject of

Engineering Sciences

Harvard University
Cambridge, Massachusetts
May 2009

Thesis advisor

**Howard A. Stone**

Author

**Ernst Adriaan van Nierop**

**Flows in Films and Over Flippers**

# Abstract

Three topics in fluid mechanics are dealt with in this dissertation, namely (i) reactive spreading and recoil of oil on water, (ii) free film formation theory and experiment, and (iii) how humpback whale flippers delay stall.

Reactive spreading of an oil droplet on water is described in Chapter 1. Small amounts of acid and base were added to the oil and water respectively, such that a surfactant was produced at the interface between the oil and the water, greatly enhancing spreading rates. After the oil drop spreads out to some maximum radius, the drop recoils on a timescale that is indicative of a diffusive process redistributing the surfactant over the entire volume of water.

In Chapter 2, the theory of soap film formation by withdrawal from a bath of soapy liquid is reviewed, and the assumptions supporting Frankel's law are challenged. Stress balances that describe film evolution in either extensional or shear flow are rigorously derived and we find that the strength of surface stress terms pick the resulting flow type. With this background in mind, we describe in Chapter 3 how films were made using aqueous solutions of poly(ethylene oxide) or PEO with and *without* surfactant. The initial thickness of these films agrees well with existing data in the literature for overlapping ranges of the capillary number $C_a$. For larger $C_a$

numbers, we observe that (i) the addition of SDS results in *thinner* films, (ii) films can be made that are thicker than the wire thickness, and (iii) films swell in thickness when the withdrawal process stops. Some potential mechanisms are described to explain the novel swelling phenomenon.

Finally, in Chapter 4, we model the bumpy flipper of a humpback whale as a perturbed elliptic wing with Joukowski profiles of varying chord length, and combine this with lifting line theory as well as experimental stall characteristics of smooth wings. This model shows that the perturbations rearrange the downwash distribution on the wing, smoothing the transition to stall. Bump amplitude dominates the smoothing, while the wavelength of the bumps plays only a small role.

# Contents

# Previously Published Work

Chapter 1 appears in near entirety in

van Nierop, E. A., Ajdari, A. & Stone, H. A. 2006 Reactive spreading and recoil of oil on water. *Phys. Fluids* **18**, 038105.

Many of the ideas presented in Chapter 2 can also be found in

van Nierop, E. A., Scheid, B. & Stone, H. A. 2008*b* On the thickness of soap films: an alternative to Frankel's law. *J. Fluid Mech.* **602**, 119–127,

but note that the work presented in this dissertation corrects a mistake in that article.

Chapter 4 appears in near entirety in

van Nierop, E. A., Alben, S. & Brenner, M. P. 2008*a* How bumps on whale flippers delay stall: an aerodynamic model. *Phys. Rev. Lett.* **100**, 054502.

Finally, other work that does not make an appearance in this dissertation, but that was a part of my graduate research experience includes

Reyssat, M., Sangne, L. Y., van Nierop, E. A., Stone, H. A. 2009 Imbibition in layered systems of packed beads. *Europhys. Lett.*, accepted.

Bick, A. G., Ristenpart, W. D. R., van Nierop, E. A., Stone, H. A. 2009 Bubble formation via multi-drop impacts. In preparation.

# Acknowledgments

The past four and a half years have been, in one word, amazing. I have many people to thank for that, starting of course with my advisor, Howard Stone. I consider myself very lucky to have been a part of Howard's group and I'd like to thank Howard for always finding the right balance between hands-on and hands-off advising, always being available to meet and talk, and always willing to enthusiastically share new ideas and mysterious results. I admire Howard's capacity to balance work and family life, and hope to be as successful in that regard when my turn comes. I'd also like to thank Howard for letting me stray into the world of humpback whales for a while, and I'd like to thank Michael Brenner for his limitless enthusiasm in coaching that project to fruition. I would like to thank Peter Howell for taking on the task of joining my PhD committee very near the end of the trip, and for educating us all on the theory of flows in thin films.

Over the years I had the great fortune of working closely with many people who passed through the Stone lab, and I am grateful for those experiences. I thank Bill Ristenpart for attempting to teach me a new word in the English language every day for the two years that we were desk neighbors. In the end, I think the only words I will remember well are 'orange' and 'Venn diagram'. I thank Sigoléne for her attempts to make me understand that she never intended to replace Bill as my desk neighbor, and for bringing the minimum of French culture into our office. I'd like to thank Rachel for lending me her brain whenever I needed a second one, Jiandi for the jasmine tea and Wushu perspective on life, and all the other members of the Stone group whom I had the pleasure to learn from and laugh with. I'd also like to thank Kate Zirpolo for making all our lives so much easier.

I owe a special thanks to the people I worked most closely with, Silas on the humpback whales, Benoit on the theory of (soap) films (also thanks to Benoit for the great stories accompanying each holiday and so much more!). Thanks to Jim MacArthur for tirelessly building multiple sensor systems based on my latest whims, and I'd like to thank Dominik Keupp for his invaluable contributions to the free film project.

Outside of the lab, my experience at Harvard would not have been the same without the Dutch Cultural Society and the Harvard Energy Journal Club (HEJC). I would like to thank Harvard, and in particular Dan Schrag and the Center for the Environment, for generous support of the HEJC which nurtured my passion for energy related topics for the past three and a half years.

Finally, I would like to acknowledge the support of my dear family both near and far. In particular, I'd like to thank my supportive parents for passing on their curiosity for the natural world to me, and my sister for reminding me what life is like far away from ivory towers. For the past four and a half years my loving and supporting wife Rocío had to put up with many conversations about "pi and alpha", and I thank her for her patience and support, as well as for her attempts at making me a better man (please keep trying!).


Just a cartoon, or a unifying theme?

Cartoon by Christophe Granet from Hagen Cartoons

Reprinted with permission from the author.

Hagen Cartoons: www.hagencartoons.com

# Chapter 1

# Reactive Spreading and Recoil of Oil on Water

The majority of this chapter is reprinted with permission from van Nierop *et al.* (2006), which was co-authored with Armand Ajdari and Howard Stone (copyright (2006) by the American Institute of Physics). When we first started this project, M. Faivre and M. Abkarian had prior experience with the chemical reaction used in this work, and their helpful advice is gratefully acknowledged. Constructive feedback on the paper from O.E. Jensen is gratefully acknowledged.

## 1.1 Introduction

The literature on spreading of thin films is vast, due to many applications in the fields of medicine, coatings and detergency amongst others (de Gennes 1985; Afsar-Siddiqui *et al.* 2003). In this chapter, we describe an unusual case of surface-

tension-driven flow where changes in surface tension produced by a chemical reaction at an interface drive a non-volatile liquid droplet to spread into a thin film on a second immiscible non-volatile liquid. The droplet spreads rapidly, reaches a maximum radius, and then slowly recoils back to a compact liquid lens. Although work has been reported on a great variety of problems involving (im)miscible and/or (non-)volatile surfactants spreading and/or retracting (e.g. Sebba (1975); Foda & Cox (1980); Gaver & Grotberg (1992); Braun *et al.* (1995); Dussaud *et al.* (1998); Poulard *et al.* (2003); Chowdhury *et al.* (2004); Sumino *et al.* (2005); Stocker & Bush (2007)), to the best of our knowledge the spreading and retraction in the same system with non-volatile immiscible fluids has not been reported prior to this work.

## 1.2 Experimental Method

A sketch of the experimental setup is given in figure 1.1(a). Before each experiment, a sterile polystyrene petri dish (VWR 100 x 15 mm, inner diameter 86 mm) was cleaned using distilled water and ethanol. The petri dish was then filled with a weak aqueous solution of sodium hydroxide (NaOH, 0.5-1 mM) to a depth of $H = 2.6$ mm. Next, a droplet (approximate volume 0.1 $\mu$l) of white heavy mineral oil (CAS 8042-47-5, $\rho = 0.862$ g/ml) containing oleic acid (0.5-1 mM) was placed on the 'water' surface using a micropipette. Upon contact of the drop with the substrate, oleic acid at the liquid-liquid interface reacts with the sodium hydroxide in the substrate to create sodium oleate (NaOleate). Sodium oleate is a surfactant that decreases the local oil/water surface tension $\gamma_{ow}$ (figure 1.1(b)) (Fernandez & Homsy 2004). This saponification reaction has been used in various pendant-drop and viscous-fingering

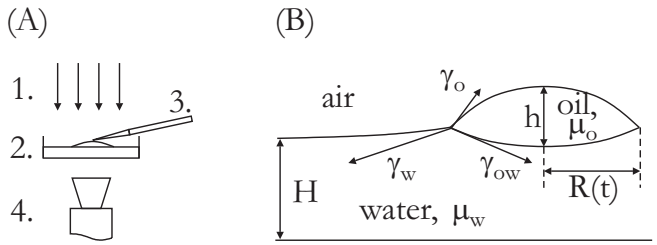


Figure 1.1: Sketch of (A) the experimental setup and (B) a liquid lens on a liquid substrate indicating the relevant surface tensions and dimensions. Setup: 1. light source, 2. petri dish with NaOH solution, 3. micropipette delivering oleic acid in an oil droplet, 4. video camera.

experiments (Touhami *et al.* 1998; Fernandez & Homsy 2003, 2004). In these systems it is known to decrease the oil-water interfacial tension as

$$\gamma_{ow} = \gamma_{ow,\infty} - (\gamma_{ow,\infty} - \gamma_{ow,0})e^{-k\,t} \tag{1.1}$$

with a rate coefficient $k \approx 0.1$ s$^{-1}$ that depends weakly on concentration (cf. Fernandez & Homsy (2003)). As a result, the spreading parameter $S = \gamma_w - (\gamma_o + \gamma_{ow})$ increases, thus providing the driving force necessary for the drop to spread. Spreading does not occur in the absence of the chemical reaction since $\gamma_o = 30.0$ mN/m and $\gamma_{ow} = 63.4$ mN/m (measured with pure oil and water using the pendant drop method) so that $S = constant < 0$, and a liquid lens forms.

We observed the oil droplets from below using a CCD camera with typical frame rates of 1-2 fps. Images of the spreading drop were analyzed using edge detection Matlab software. The error in the drop radius is estimated to be less than 5% (the error is largest for the smallest drops). In each sequence of images, '$t = 0$' corresponds to the image *prior* to the first available image in which the micropipette no longer touches the drop; the largest possible error in the time scale is one time step in the video, which is less than 1 s. The initial radius $R(0) = R_0$ was extrapolated from the

first six recorded radii by quadratic fitting.

## 1.3 Results

A typical sequence of images of an oil drop spreading and recoiling is shown in figure 1.2. This particular drop contained 0.5 mM oleic acid, while the substrate contained 1 mM NaOH. As indicated by the length scales in the image, the drop spreads from an initial radius $R_0 \approx 0.4$ mm to $R_{max} = 1.75$ mm, so that the thickness of the drop decreases to $h \approx 10$ $\mu$m. The times indicated in the images show how the spreading to $R_{max}$ takes about 15 seconds, after which the drop radius begins to decrease monotonically. The drop continues to recoil for many minutes until finally reaching a final radius similar to the initial radius. Note the visible appearance of the rim of the drop when it just reaches $R_{max}$ and is about to start recoiling. The images suggest that recoiling starts at the rim, and creates a 'tear'-like structure, which is thicker near the rim and thinner near the center of the drop. Though we have not systematically studied this phenomenon, this type of flow (near the rim only) corresponds to what is typically observed following film rupture (Brochard-Wyart *et al.* 1993; Breward 1999). Subsequent images at later times indicate that the tear-drop structure is likely a transient one; as viewed from above, the largest part of the recoil appears to occur with a drop shape that resembles a flat pancake (figure 1.2).

The spreading and recoiling data for four experiments with different combinations of the acid/base concentrations are shown in figure 1.3. The top graph shows the data on linear scales while the bottom graph uses logarithmic scales to identify any power-

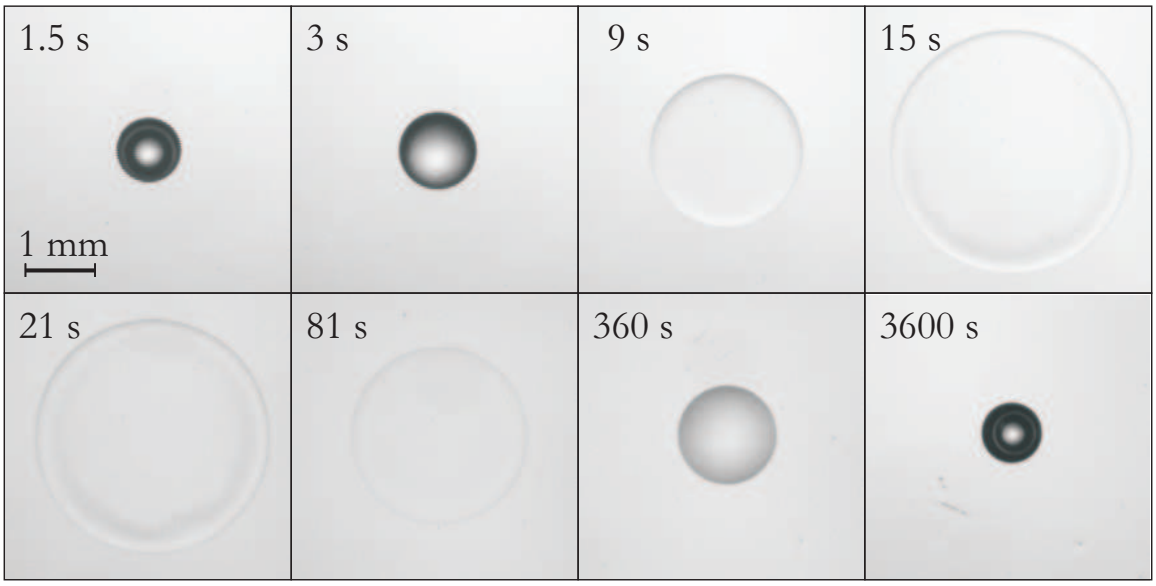


Figure 1.2: Images obtained from a typical experiment. A droplet with volume $\sim 0.1$ $\mu$l of 0.5 mM oleic acid was placed on 15 ml of 1 mM NaOH (2.6 mm deep). At about $t = 15$ s the drop has obtained its maximum size $R_{max} = 1.75$ mm, and a ring-like structure becomes apparent near the outer perimeter of the drop. The drop then recoils over a time on the order of minutes rather than seconds.

law-like dynamics. From this data we observe that the initial slopes of the spreading curves increase with increasing concentrations. The slowest spreading occurs for 0.5 mM acid on 0.5 mM base, and this also results in the smallest $R_{max}/R_0$. The fastest spreading occurs for 1.0 mM acid on 1.0 mM base, and this combination creates the largest maximum radius. The two 'in between' cases (0.5 mM acid on 1.0 mM base and 1.0 mM acid on 0.5 mM base) show quite similar spreading dynamics and maximum radii. We comment on the recoiling dynamics below.

Several control experiments were conducted to verify that the observed dynamics were indeed caused by the interfacial chemical reaction. In the first control, oil was placed on water (no reagents or surfactant present); the oil spread slowly, eventually reaching an equilibrium drop radius with $R_\infty/R_0 \approx 1.25$ (figure 1.3). As a second

control, oil was placed on NaOleate-containing water (at various concentrations). With 1 mM NaOleate in the water (this is just below the CMC), droplets of oil were seen to be emulsified rapidly, eventually disappearing from the surface entirely. For significantly lower concentrations of NaOleate ($\approx$ 0.05 mM), the drops did not dissolve, and again spread to $R_\infty/R_0 \approx 1.25$. Sodium oleate does not readily dissolve in mineral oil, so that it was not possible to perform a control in which NaOleate-containing oil would have been spread on water. In a third control, drops of mineral oil with 0.5-1.0 mM oleic acid were placed on pure water and again slow spreading was observed with $R_{max}/R_0 \approx 1.2$. As a fourth control, pure oleic acid was placed on water; very rapid spreading of a precursor film was observed indirectly using small bubbles as surface markers. Finally, in an otherwise 'normal' experiment (such as those in figure 1.3) talcum powder was spread on the substrate-surface prior to drop placement. No motion of the talc was observed, indicating that there is no precursor monolayer in this system. It is clear from these control experiments that a drop spreading with $R/R_0 > 2$, and reaching a maximum radius before finally recoiling, are consequences of adding an interfacial chemical reaction to the system.

Plotting the radius versus time on logarithmic scales as in figure 1.3 should reveal possible power-law spreading dynamics, if such dynamics are present. Rather than clear power-law dynamics (i.e. constant slopes for at least an order of magnitude on the time axis), we observe a gradually increasing spreading rate until the maximum radius is achieved. Force balances can be made for specialized spreading problems (e.g. de Gennes (1985); Lister & Kerr (1989)), and scaling arguments are employed to predict power-law spreading of the form $R(t) \propto t^\alpha$, where $R$ is the drop radius.

The physical responses of experimental systems are often more complex and, because of the interplay of various forces, only show power-law-like spreading for *finite* time intervals. In order to be able to make quantitative comparisons with existing work, we fit power-law curves to our data for finite time intervals during the rapid spreading and slow recoiling stages. In particular, we take only the data from half a decade in the time interval preceding $t_{max}$ (the time corresponding to $R = R_{max}$) and fit this data with straight lines (figure 1.3). We find that the average exponents are $0.64 < \alpha_{spread} < 0.89$, with $\alpha_{spread}$ being smaller for low concentrations of reactants (table 1.1). We can contrast this result with power-law spreading of a drop on a thin film, where the drop acts as a source of constant concentration (Jensen 1994), for which $R(t) \propto t^{1/2}$.

For recoil, taking just the data from $t_{max}$ to half a decade later in time and fitting as a power law shows that the average exponents are $-0.34 < \alpha_{recoil} < -0.14$ (table 1.1). Note the fairly large standard deviations in $\alpha_{recoil}$, indicating that some caution is necessary when drawing general conclusions about the recoiling process. Nevertheless, the data suggest that the qualitative recoiling behavior is correlated to the concentration of the base in the water phase and is typically faster in experiments with lower concentrations of NaOH.

## 1.4 Discussion

We observe three separate stages of the experiment to be discussed; (i) spreading, (ii) recoil, and (iii) the final equilibrium size of the lens.

| acid \ base | | 0.5 mM | 1.0 mM |
|---|---|---|---|
| 0.5 mM | $\alpha_{spread}$ | $0.64 \pm 0.06$ | $0.81 \pm 0.07$ |
| | $\alpha_{recoil}$ | $-0.34 \pm 0.09$ | $-0.14 \pm 0.04$ |
| | $R_{max}/R_0$ | $3.09 \pm 0.44$ | $3.88 \pm 0.45$ |
| 1.0 mM | $\alpha_{spread}$ | $0.88 \pm 0.06$ | $0.89 \pm 0.06$ |
| | $\alpha_{recoil}$ | $-0.22 \pm 0.10$ | $-0.14 \pm 0.08$ |
| | $R_{max}/R_0$ | $3.78 \pm 0.36$ | $4.16 \pm 0.62$ |

Table 1.1: Spreading and recoiling coefficients, as well as $R_{max}/R_0$ for various combinations of acid/base concentrations. Statistics were collected for 4-6 experiments at each set of concentrations. [average ± standard deviation]

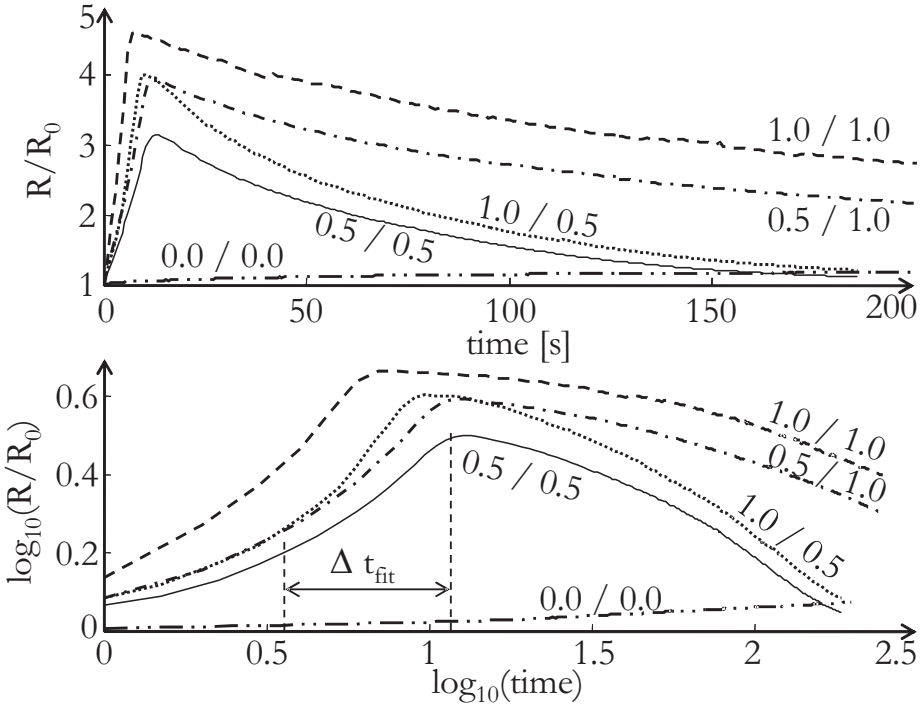


Figure 1.3: Typical results for various concentrations of NaOH and oleic acid. Solid line: 0.5 mM acid on 0.5 mM base, dotted line: 1.0 mM on 0.5 mM, dash-dot line: 0.5 mM on 1.0 mM, dashed line: 1.0 mM on 1.0 mM. There were slight variations in the initial radius of these four experiments, $R_0 = 0.58, 0.58, 0.45, 0.55$ mm respectively. The lowest curve (dash-dot-dot) is the control with oil on water. These curves were chosen from a larger data set to represent *typical* results. Also indicated is $\Delta t_{fit}$, the time interval over which a straight line was fitted to obtain $\alpha_{spread}$ for 0.5 mM on 0.5 mM spreading (table 1.1).

### 1.4.1 Spreading

We explain the observed spreading dynamics as follows. When the droplet is first placed on the NaOH/air interface, only a few oleic acid molecules are near the interface and readily react with the NaOH to produce the surfactant, NaOleate. As a result, the oil/water interface tension decreases, the spreading parameter $S$ increases but remains negative, and the drop spreads to a new (instantaneous) equilibrium radius. These first stages of spreading correspond to a quasi-static process which maintains equilibrium at the triple line. Balancing the surface tensions at the contact line and assuming that the droplet takes the shape of two spherical caps as in a liquid lens, gives an exact relationship between drop radius and $\gamma_{ow}$. Using (1.1) and expanding the resulting relationship for early times, we obtain $R(t) - R_0 \propto V^{1/3} k\, t$, which gives spreading rates of order 0.1 mm/s when $k \sim 0.1$ s$^{-1}$, in qualitative agreement with our experiments. Note that since the droplet is much more viscous than the water phase ($\mu_o/\mu_w \approx 10^2$), and despite the substrate being shallow (de Rycke 1997), order of magnitude estimates (Bacri *et al.* 1996) show that dissipation is dominated by viscous *stretching* of the oil droplet. Consequently, the dissipative stress is of order $\mathcal{O}(\mu_0 u/R)$, and weak during early stages of spreading, in agreement with the quasi-static spreading model.

This quasi-static process then proceeds, gradually reacting away all the oleic acid in the drop and increasing its surface area. If after some time the spreading parameter becomes positive, then there is no equilibrium radius and a stress balance with dissipative mechanisms is needed to find the spreading rate. If we assume that the quantitative results from the work of Fernandez & Homsy (2003) and (1.1) approxi-

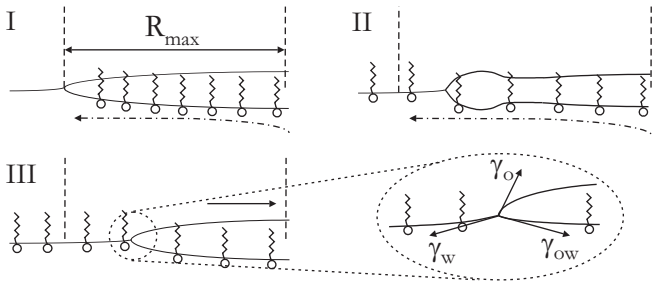


Figure 1.4: Sketch of the suggested mechanism for recoiling: I. Reaction goes to completion and the drop reaches a maximum radius; II. Surfactant diffuses beyond the maximum radius of the drop; III. $\gamma_w \approx \gamma_{wo}$ and so the spreading parameter reduces to $S \approx -\gamma_o$, and the drop recoils.

mately hold for this system, we expect $S$ to become positive after $t \sim 5$ s. For these longer times a different approach is then necessary, in which there is a balance between the driving and dissipative stresses acting on the drop. The main driving stress for spreading is surface tension (of order $\mathcal{O}(S/R)$), provided no precursor monolayer develops (Bacri *et al.* 1996). The gravity (of order $\mathcal{O}(\rho_o g h)$) and capillary stresses (of order $\mathcal{O}(\gamma_o h/R^2)$) are much weaker, since the drop height is always smaller than the capillary length (of order 1 mm) and the drop is generally quite flat. However, it is clear that more work is required to fully characterize the system in all spreading regimes. In particular, whether the spreading parameter stays negative at all times (with $R = R_{max}$ when $|S|$ is smallest) or whether $S > 0$ for some period of time (with $R = R_{max}$ when $S$ crosses through zero the second time) is an open question.

### 1.4.2 Recoil

In any case, at a certain time almost all the oleic acid in the drop will have reacted. As a result, a maximum radius is reached, and as diffusion overcomes the rate of production of surfactant at the interface the surface tensions in the neighborhood of

the contact line are modified, breaking mechanical equilibrium and causing the drop to recoil. A tentative mechanism for the recoiling is sketched in figure 1.4. After spreading to $R = R_{max}$, we assume that most of the NaOleate is 'trapped' at the oil/water interface (figure 1.4.I). Next, NaOleate diffuses to the air/water interface (figure 1.4.II), possibly assisted by weak advection due to a Marangoni flow that persists in the substrate until chemical equilibrium is reached. We estimate that the time scale for NaOleate to diffuse through the substrate (diffusivity in bulk water $\sim 10^{-5}$ cm$^2$/s), a distance comparable to the maximum radius of the drop, is of order $10^3$ s which compares favorably with the time scales in figures 1.2 and 1.3. Diffusion of surfactant effectively decreases $\gamma_w$ and increases $\gamma_{ow}$, thus tending to equalize $\gamma_w$ and $\gamma_{ow}$. As a result, mechanical equilibrium at the triple line is broken, and the drop recoils under the tension provided by $\gamma_o$ (figure 1.4.III). This diffusive mechanism is consistent with the observation that the surface tension of an oil/water interface, which has been treated with surfactant, can *increase* with time due to migration of surfactants away from the interface (Touhami *et al.* 1998). We suggest that the role of the concentration of NaOH on the recoiling dynamics (figure 1.3) lies in the fact that the Debye length varies as the inverse square root of the NaOH concentration. When fewer ions are present in the substrate, the polar heads of the NaOleate molecules repel each other more strongly at a given molecular spacing then when more ions are present to screen the charged heads. Hence, the diffusion of surfactant away from the oil/water interface is enhanced by the intermolecular repulsion the strength of which increases with lower concentrations of NaOH.

### 1.4.3 Equilibrium

Finally, it may be surprising that the final equilibrium radius of the lens is about equal to the initial radius (figure 1.2), despite the presence of surfactant in the system. Given a drop volume of 0.1 $\mu$l and concentration of 1 mM acid, we expect on the order of $10^{13}$ surfactant molecules. If these are evenly spaced at the oil/water interface, then given typical values of $R_{max}$ we expect intermolecular spacings of about 1 nm (i.e. smaller than the Debye length). Once the surfactant is spread out evenly over the entire surface of the petri dish however, the intermolecular spacing increases to roughly 30 nm. At such low surface concentrations, the surfactant hardly influences the surface tensions of the system, and we expect the final drop radius to be close to the initial radius.

## 1.5 Conclusions

To summarize, we have observed drops of oil spreading on water with an interfacial chemical reaction which altered the spreading dynamics such that (a) the rate of spreading is much faster than what is expected for surfactant spreading on a liquid, (b) this spreading rate depends on the concentrations used in the interfacial reaction, being faster for larger concentrations, (c) a maximum radius is reached 3-5 times the size of the initial drop radius and finally, (d) the drops recoil back to their initial radius over a much longer period of time than the time it takes to spread. We present arguments to provide a qualitative understanding of the physical mechanisms, but further modeling of this system is necessary for full understanding of the complex

interplay of various spreading and dissipation mechanisms.

# Chapter 2

# Free Film Formation: Theory & Background

Much literature has been devoted to 'thin film' dynamics, where either a thin film of liquid is supported by some solid substrate (e.g. plate coating, see figure 2.1(A)), or where there is no support for the film at all except at its borders (e.g. soap films, see figure 2.1(B)). We are primarily interested in the latter, 'free', film. Such free films occur in the formation of large soap films, or smaller films in foams, as well as in industrial processes spanning float-glass, polymer film-blowing, and for example the formation of solar panels from a bath of liquid silicon.

The physics and mathematics that describe such free films is naturally quite similar from one application to the next, and we have therefore focused our attention on a system that can be easily studied in the lab, namely the formation of a soap film. The current theory that predicts the thickness of soap films based on experimental parameters is referred to as Frankel's law. In this chapter, we review the main ideas

that go into the derivation of Frankel's law, and discuss some of the important system parameters that do *not* enter Frankel's law. In particular, this approach leads to a more general discussion of the type of flow that is to be expected to prevail inside a free film, either a shear-like or an extensional flow. Many of the ideas regarding Frankel's law and soap film formation were published in van Nierop *et al.* (2008*b*). Although later discussions with Benoit Scheid and Peter Howell uncovered a conceptual error in that original paper, much of the background remains unaltered and we therefore pursue it to better understand the role of surface properties in film formation.

In §2.2, starting from the Navier-Stokes equations, we investigate in more detail which system parameters (surface tension, surface viscosity, Marangoni stresses, etc.) dominate the formation and evolution of a film. By setting up appropriate stress balances for extensional and/or shear-like flows in films, it is straightforward to demonstrate that the strength of surface shear terms (introduced for example by Marangoni stresses or surface viscosity) 'pick' the correct stress balance to be used.

Following this theoretical discussion, in the next chapter we turn to experiments that extend the realm of conditions under which (soap) films have been made. As will be discussed in greater detail in the next chapter, by changing the (surface) properties of the fluids we can probe different film flow regimes, for example, by tuning the concentrations of dissolved polymer and surfactant.

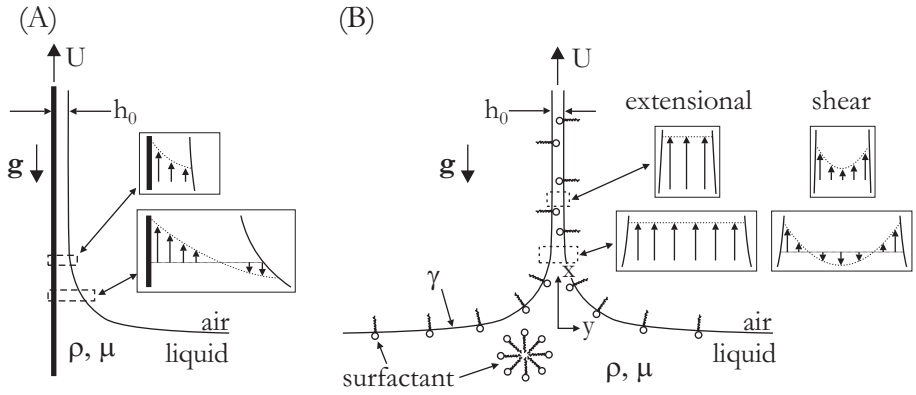


Figure 2.1: (A) Sketch of the typical LLD film-coating experiment, which can be performed with or without surfactants. The region connecting the 'static' meniscus to the film of uniform thickness is called the dynamic meniscus. The flow in the dynamic meniscus is shear-like, as sketched for two different positions in the film. (B) Sketch of a soap-film pulling experiment. In all reported experiments, the concentration of the surfactant is close to or above the critical micelle concentration (cmc), so micelles are present in the bulk. The flow can be either extensional (i.e. $u = u(x,t)$) or shear-like (i.e. $u = u(x,y,t)$), as illustrated by the insets.

## 2.1 Soap Films and Frankel's Assumptions

It is simple to make a soap film by withdrawing a wire frame from a bath of soapy water as sketched in figure 2.1(B). Whether demonstrating colorful interference patterns in a soap film or determining properties of an industrial foam, an accurate prediction of the soap film thickness is important. Frankel is credited with showing that if the soap film interfaces are assumed to be rigid and inextensible, then for withdrawal from a liquid bath the film thickness $h_0$ varies as (Mysels *et al.* 1959)

$$\frac{h_0}{\ell_c} = 1.89 \left( \frac{\mu U}{\gamma} \right)^{2/3} = 1.89\, C_a^{2/3} \,, \tag{2.1}$$

where $\ell_c = \sqrt{\gamma/\rho g}$ is the capillary length, $\mu$ is the viscosity of the liquid, $U$ is the speed at which the film is withdrawn from the bath, $\gamma$ is the surface tension and $C_a$ is the capillary number. The derivation of (2.1) is *identical* to that used in the

Landau-Levich-Derjaguin (LLD) problem where a flat plate is withdrawn from a bath of liquid as sketched in figure 2.1(A) (see e.g. de Gennes *et al.* (2004)). However, Frankel's model assumes that both film interfaces act as rigid plates moving up with constant speed $U$, hence the prefactor in (2.1) is twice as large as for the LLD result.

It is possible to examine this result using data spanning more than 40 years of work by independent research groups, as shown in figure 2.2. These experiments have confirmed that $h_0 \propto U^{2/3}$ over a large range of $U$, with deviations at both low speeds, when the film thickness $h_0 \leq 100$ nm and intermolecular forces play a role, and high speeds, when the film thickness saturates to the diameter of the wire frame. The spread in the pre-factor in the data in figure 2.2 is larger than can be attributed to the experimental error reported by the investigators and suggests that Frankel's law, with its sole viscous dependence on the shear viscosity of the liquid, may not be universally valid. The only way in which the properties of the specific surfactant in the soap film enters Frankel's law is through the surface tension.

The underlying assumptions in Frankel's analysis that the film interfaces are rigid and that the flow is therefore shear-like (as sketched in figure 2.1(B)) motivated us to explore this question in more detail. A model with extensible but viscous film interfaces can be expected to provide a better description of the physical processes that govern the thickness of a soap film during withdrawal. The concept of surface viscosity is explained in more detail in §2.1.2, and the question of the likely role of Marangoni stresses is addressed in §2.1.3. Then, in §2.2, we asymptotically analyze the Stokes equations (including both surface viscosity and Marangoni stresses in the boundary conditions) for small aspect ratios $\epsilon = h_0/\ell$, where $\ell$ is the length of the

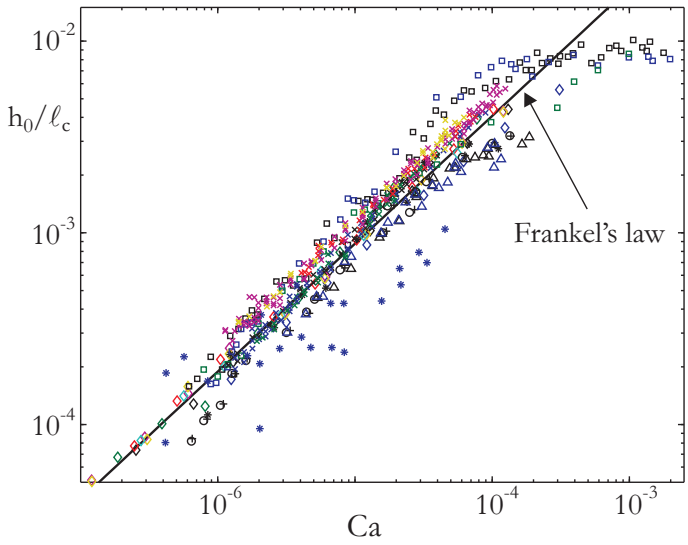


Figure 2.2: All existing data on soap film thicknesses; see table 2.1 for a full legend. Solid line: Frankel's law (2.1).

dynamic meniscus. The dynamic meniscus spans the region of fluid between the *static* meniscus and the film of constant thickness, and typically $h_0 \ll \ell \ll \ell_c$.

### 2.1.1 Soap films with polymers

To probe non-Newtonian effects, a number of authors have added various quantities of the water soluble polymer PEO (poly ethylene oxide) to solutions with 2% SDS. A summary of the solutions used in the various publications is listed in table 2.2. Note that the data in Bruinsma *et al.* (1992) was taken directly from Lionti-Addad & di Meglio (1992), so only the data from the paper by Lionti-Addad & di Meglio (1992) is reported in table 2.2. Likewise, some of the data reported in Lionti-Addad & di Meglio (1992) was repeated in Cohen-Addad & di Meglio (1994), so in table 2.2 we only list those solutions that were new in the 1994 publication.

From a comparison of figures 2.2 and 2.3, it is clear that the larger the concentra-

| | Source | $\mu$ mPa.s | $\gamma$ mN/m | Solutions |
|---|---|---|---|---|
| ◊ | Mysels & Cox (1962) | 0.9 | 38 | 0.25% commercial detergent |
| | | 0.9 | 31 | 1% comm.det. |
| | | 0.9 | 32 | 5% comm.det. |
| | | 0.9 | 50 | 0.29% SDS |
| | | 0.9 | 34 | 0.2% SDS + 0.01% dodecanol |
| | | 2.7 | 45 | 0.25% comm. det. + 37% glycerol |
| | | 14.5 | 51 | + 68% glycerol |
| + | Bruinsma *et al.* (1992) | 1 | 33 | 2% (8 × cmc) SDS (70% pure) |
| ○ | Lionti-Addad & di Meglio (1992) | 1.05 | 33 | 2% SDS (70% pure) |
| ∗ | Cohen-Addad & di Meglio (1994) | 1.1 | 17 | 0.01% (2.6 × cmc) "fluoro" (zwitter.) |
| | | 1.3 | 30 | 0.5% (250 × cmc) $C_{12}E_5$ (nonionic) |
| △ | Lal & di Meglio (1994) | 1.25 | 23 | 4% octanoic acid |
| | | 1.24 | 37 | 4% decanoic acid |
| □ | Adelizzi & Troian (2004) | 1 | 37 | 2% SDS + 4% glycerol |
| | | 1 | 36 | + 8% glycerol |
| | | 1 | 29 | 2% (12 × cmc) SDBS |
| × | Berg *et al.* (2005) | 1 | 50 | 0.08% SDS |
| | | 1 | 45 | 0.1% SDS |
| | | 1 | 39 | 0.4% SDS |
| | | 1 | 37 | 2% SDS |
| | | 1 | 37 | 2% SDS + 4% glycerol |
| | | 1 | 35 | + 8% glycerol |

Table 2.1: Solutions used for the data shown in figure 2.2. All solutions are aqueous and concentrations of surfactant are reported as weight %. Viscosities and surface tensions are all as reported, except for the data from Mysels & Cox for which $\gamma$ was calculated.

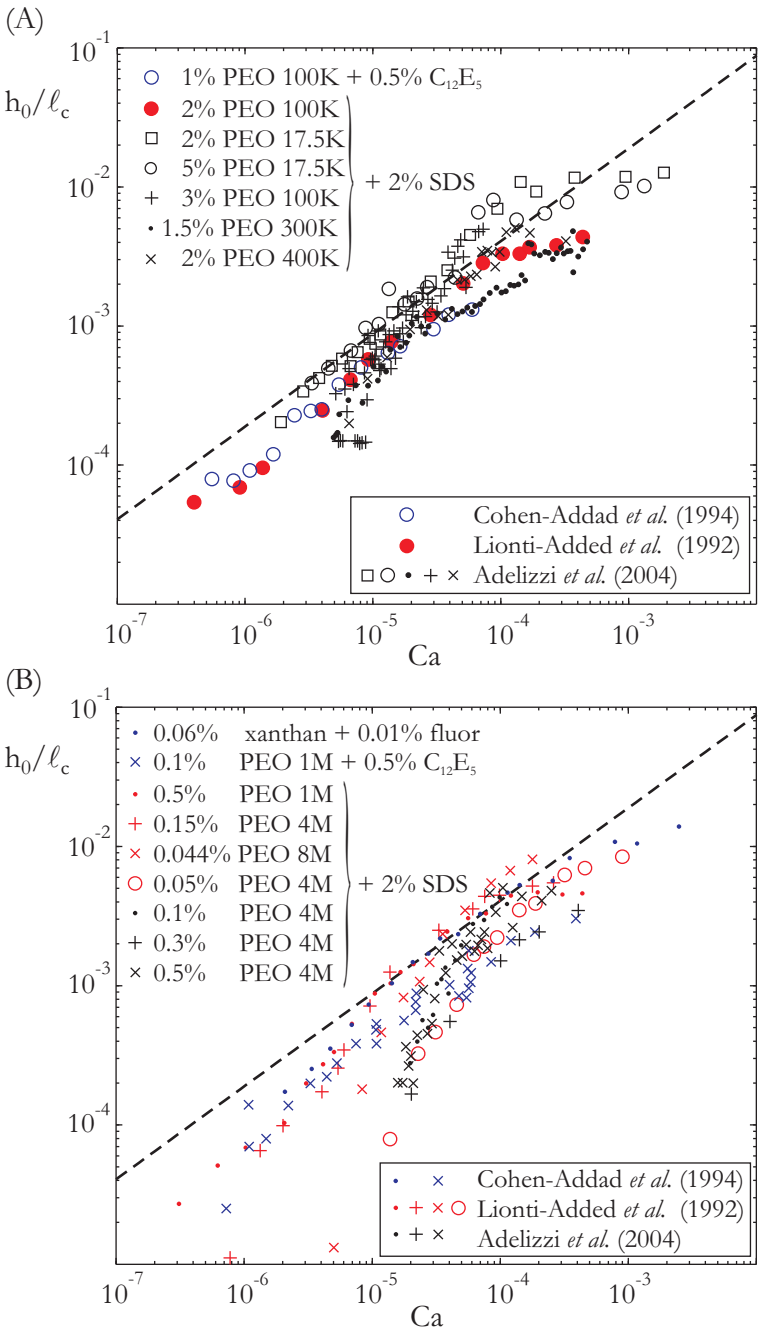


Figure 2.3: All existing data on soap films with added polymer. (A) low molecular weights, up to 400 kg/mol and (B) high molecular weights from 1000 kg/mol upwards. See table 2.2 for a more comprehensive legend. Dashed lines in both (A) and (B) correspond to Frankel's law (2.1).

tion and/or molecular weight of the polymer, the larger the deviations from Frankel's law. Bruinsma *et al.* (1992) explored the effects of including normal stresses in the stress tensor (since these can be supported by non-Newtonian fluids). They found that including normal stresses would over-predict the film thickness at any given $C_a$, and the agreement with Frankel's law should be recovered for the limit of $C_a \to 0$. Including the possibility that the soap film essentially consists of an outer rigid surfactant layer and an inner fluid polymer matrix, Bruinsma *et al.* (1992) also researched what the effect would be on Frankel's analysis if an effective slip length was attributed to the polymer matrix flowing over the surfactant layer. Although such an approach gave good qualitative agreement with experimental data, the required slip lengths are far larger than any existing theory could explain, since they are of the order of microns rather than 1-100 nm. Later work by Adelizzi & Troian (2004) expanded the range of polymer concentrations and molecular weights used in making films, but again a conclusive explanation of the deviation from Frankel's law proved to be elusive.

In §3.3, we show our own data obtained for solutions of PEO and SDS, as well as solutions that do not have SDS at all. For the latter type of solutions, there is no reason to expect that there would be a rigid surface layer on the film, and therefore it would also be more difficult to reason why the flow in the film is of a shear-like rather than an extensional nature.

### 2.1.2 The importance of surface viscosity

Frankel's law does not account for surface viscosity introduced by the presence of surfactant at the interface. Surface viscosity (denoted $\mu^* = \kappa_s + \mu_s$) is the 'viscosity'

| Source | Polymer | Surfactant | $\mu$ mPa.s | $\gamma$ mN/m | Symbol |
|---|---|---|---|---|---|
| Lionti-Addad & di Meglio (1992) | PEO | SDS 2% | | | |
| | 2%, 100K | | 4.5 | 32.9 | ● |
| | 0.05%, 4M | | 3.4 | 32.8 | · |
| | 0.1%, 4M | | 6.7 | 32.8 | + |
| | 0.3%, 4M | | 62 | 32.8 | × |
| | 0.5 %, 4M | | 154 | 32.8 | ○ |
| Cohen-Addad & di Meglio (1994) | PEO | $C_{12}E_5$ 0.5% | | | |
| | 1%, 100K | | 2.6 | 30.3 | ○ |
| | 0.1%, 1M | | 3.4 | 30.3 | · |
| | Xantham gum | Fluor | | | |
| | 0.06%, 2.5M | 0.01% | 14 | 20.3 | × |
| Adelizzi & Troian (2004) | PEO | SDS 2% | | | |
| | 2%, 17.5K | | 3 | 39.2 | □ |
| | 5%, 17.5K | | 10 | 38.9 | ○ |
| | 3%, 100K | | 13 | 37.1 | + |
| | 1.5%, 200K | | 10 | 37.1 | · |
| | 2%, 400K | | 69 | 37.9 | × |
| | 0.5%, 1M | | 130 | 37.5 | · |
| | 0.15%, 4M | | 103 | 36.2 | + |
| | 0.044%, 8M | | 43 | 36.4 | × |

Table 2.2: Solutions used for the data shown in figure 2.3. All solutions are aqueous and concentrations of surfactant are reported as weight %. Viscosities and surface tensions are all as reported.

associated with dilating ($\kappa_s$) or shearing ($\mu_s$) a 'populated' interface (Scriven 1960; Edwards *et al.* 1991). Including surface viscous effects in the dynamics of soap films is quite common, e.g. it has been used to model film drainage (Schwartz & Roy 1999; Naire *et al.* 2001), and it dominates foam relaxation times (Durand & Stone 2006).

The introduction of the surface viscosity $\mu^*$ naturally leads to two dimensionless parameters, namely the Boussinesq number $B_q = \mu^* / (\mu \ell)$ and the 'surface capillary' number $C_s = \mu^* U / (\gamma \ell) = C_a B_q$, where $\ell$ is a relevant length scale in the problem, for example the film thickness, capillary length or length of the dynamic meniscus (the latter depends on the capillary number). The Boussinesq number represents a balance between surface viscous stresses and (extensional) bulk viscous stresses, and can be quite large. Estimates of $\mu^*$ come from measurements of $\kappa_s$ which is typically orders of magnitude larger than $\mu_s$. Since $\kappa_s \sim 10^{-6} - 10^{-3}$ Pa.m.s (e.g. Fruhner *et al.* (1999); Liu & Duncan (2006)), we expect (picking $\ell = \ell_c$) $B_q \sim 1 - 10^3$, which emphasizes the relative importance of surface properties.

### 2.1.3 Time scales and Marangoni stresses

To determine the potential role of gradients of surface tension (Marangoni stresses) in soap film formation, it is useful to consider the time scales that dominate surfactant transport and adsorption, and to compare that to the rate of surface expansion (e.g. Shen *et al.* (2002)). If the surfactant moves to new parts of the interface very rapidly relative to the stretching rate of the interface, then it is reasonable to expect surface tension gradients to be negligible in the dynamics.

When new interface is generated by stretching on a time scale of $t_s = \ell / U$ (where

$\ell$ is the length of the dynamic meniscus), surfactant will populate the interface by diffusing there within a typical time $t_d = h_0^2/D$ (where $D$ is the diffusion coefficient) and then, for surfactants shown in table 2.1, adsorb in about $t_a \approx 4 \cdot 10^{-4}$ s (Shen *et al.* 2002). Since adsorption is almost never the rate-limiting step in the process, surface tension gradients can be assumed negligible if $t_d \ll t_s$.

In §2.2 it is shown that $\ell$ varies between $h_0/C_a$ and $h_0/C_a^{1/3}$, for extensional or shear flow respectively. Knowing at least empirically that $h_0 \sim \ell_c\, C_a^{2/3}$, we can thus estimate $t_d/t_s$ to be

$$\frac{t_d}{t_s} = \frac{h_0^2/D}{\ell/U} \sim \frac{h_0\, U\, C_a^n}{D} \sim \frac{\gamma\, \ell_c}{\mu\, D}\, C_a^{n+\frac{5}{3}}, \tag{2.2}$$

where $n$ is either 1 or 1/3, depending on $\ell$. Using $D \approx 10^{-9}$ m$^2$/s, and $\mu \approx 10^{-3}$ Pa.s, we thus see that Marangoni stresses are only negligible when

$$\frac{t_d}{t_s} \ll 1 \quad \Rightarrow \quad C_a \ll 10^{-7/2} \approx 3 \times 10^{-4} \qquad \text{for } n = 1/3 \qquad \text{(shear)} \tag{2.3}$$

$$C_a \ll 10^{-21/8} \approx 2 \times 10^{-3} \qquad \text{for } n = 1 \qquad \text{(extensional)} \tag{2.4}$$

Since all of the experimental withdrawal velocities were slow (between $\mu$m/s - mm/s), and surfactant concentrations were close to or larger than the critical micelle concentration (cmc), surfactant diffusion across the film and subsequent adsorption to the interface occur more rapidly than surface stretching. As a result, surface tension gradients are indeed expected to be negligible during film formation by withdrawal from a bath. However, we will retain the Marangoni terms in the analysis of the full equations, to demonstrate their importance in other systems with less concentrated surfactant and/or slower diffusion times. Also, we cannot dismiss *a priori* the possibility of having different time scales for diffusion and stretching along the length of

the film, since stagnation points may also occur at the interface, at least for shear-like flow (Ramé 2007).

## 2.2 Film Equations from the Navier-Stokes Equations

Here, we derive the equations that describe film evolution over time, starting from the Navier-Stokes equations. In particular, we are interested in the two distinguished limits, which were also discussed by Breward & Howell (2002), namely the limit of extensional flow, and the limit of shear flow. Although it would be relevant for strongly non-Newtonian fluids, we have restricted the analysis to regular Newtonian fluids for now.

As is shown below, the strength of the surface stresses (which enter the boundary conditions) dictate what type of flow the film experiences: extensional- or shear-like. When deriving evolution equations for thin films starting from the Navier-Stokes equations, it is common to non-dimensionalize the equations using known scales for pressure, velocities, etc. However, it is not always clear *a priori* which scales are the natural ones for the problem at hand. As discussed in earlier work by Breward & Howell (2002) and demonstrated here, for the case of flow in free films, the strength of the surface stresses will dictate the appropriate scale for pressure (all other scales having a natural choice).

### 2.2.1 From the Navier-Stokes equations to extensional or shear flows in thin films

To begin, we write the Navier-Stokes equations for an incompressible flow

$$\boldsymbol{\nabla} \cdot \mathbf{u} = 0 \tag{2.5a}$$

$$\rho \left( \mathbf{u}_t + \mathbf{u} \cdot \boldsymbol{\nabla}\, \mathbf{u} \right) = -\boldsymbol{\nabla} p + \mu \nabla^2 \mathbf{u} + \rho\, \mathbf{g}. \tag{2.5b}$$

Also, we have boundary conditions at the interface $y = h(x,t)$ where surface viscous terms are included (see e.g. Edwards *et al.* (1991) and Naire *et al.* (2001)),

$$\mathbf{n} \cdot (\boldsymbol{\tau} \cdot \mathbf{n}) = \kappa \gamma^* \tag{2.6a}$$

$$\mathbf{t} \cdot (\boldsymbol{\tau} \cdot \mathbf{n}) = \mathbf{t} \cdot \boldsymbol{\nabla}_s \gamma^* \tag{2.6b}$$

$$v|_{y=h} = h_t + u\, h_x \tag{2.6c}$$

$$v|_{y=0} = 0, \quad \left.\frac{\partial u}{\partial y}\right|_{y=0} = 0. \tag{2.6d}$$

Here $\gamma^* = \gamma + \mu^* \boldsymbol{\nabla}_s \cdot \mathbf{u}$ and $\mu^* = (\kappa_s + \mu_s)$ is the sum of surface dilatational and shear viscosities, $\kappa$ is twice the mean curvature of the interface, and $\mathbf{n}$ and $\mathbf{t}$ are the normal and tangent vectors to the interface respectively (see also figure 2.4), and $\boldsymbol{\nabla}_\mathrm{s}$ is the surface gradient operator. Note that we use the subscript '$s$' to denote surface terms while the subscripts '$x$', '$y$' and '$t$' denote partial derivatives in $x$, $y$ and $t$ respectively. Also note that we have used $h$ as the half-width of the film in equations (2.6c) and (2.6d), although we typically think of $h$ as the full-width (as sketched in figure 2.4 for example). Using $h$ as the half-width avoids the need to carry around factors of $\frac{1}{2}$, and we can switch back to a notation where $h$ is the full-width at any point in the derivation by simply substituting $h \to h/2$.

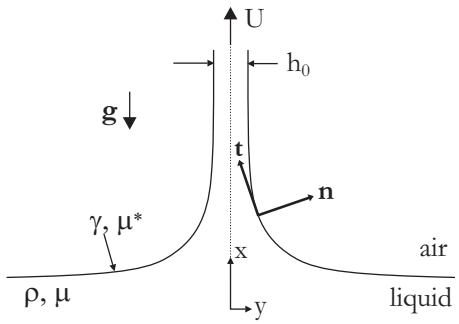


Figure 2.4: Sketch of film with relevant parameters for stress balance derivation.

We proceed by writing down the component form of the mean curvature and normal and tangent vectors,

$$\kappa = -\boldsymbol{\nabla}_s \cdot \mathbf{n} = \frac{h_{xx}}{(1+h_x^2)^{3/2}} \tag{2.7}$$

$$\mathbf{t} = \frac{1}{\sqrt{1+h_x^2}} \begin{bmatrix} 1 \\ h_x \end{bmatrix}, \qquad \mathbf{n} = \frac{1}{\sqrt{1+h_x^2}} \begin{bmatrix} -h_x \\ 1 \end{bmatrix}. \tag{2.8}$$

Similarly for the 2-D stress tensor and the surface gradient operator,

$$\boldsymbol{\tau} = \begin{bmatrix} -p + 2\mu u_x & \mu(u_y + v_x) \\ \mu(u_y + v_x) & -p + 2\mu v_y \end{bmatrix}, \quad \text{and} \tag{2.9}$$

$$\boldsymbol{\nabla}_s = \boldsymbol{\nabla} - \mathbf{nn} \cdot \boldsymbol{\nabla} = \mathbf{e}_i \frac{\partial}{\partial x_i} - n_i n_j \mathbf{e}_i \frac{\partial}{\partial x_j} \tag{2.10}$$

$$= \left[ \left(1 - n_x^2\right) \frac{\partial}{\partial x} - n_x n_y \frac{\partial}{\partial y} \right] \mathbf{e}_x + \left[ \left(1 - n_y^2\right) \frac{\partial}{\partial y} - n_x n_y \frac{\partial}{\partial x} \right] \mathbf{e}_y, \tag{2.11}$$

$$= \frac{1}{1+h_x^2} \left[ \left( \frac{\partial}{\partial x} + h_x \frac{\partial}{\partial y} \right) \mathbf{e}_x + \left( h_x \frac{\partial}{\partial x} + h_x^2 \frac{\partial}{\partial y} \right) \mathbf{e}_y \right]. \tag{2.12}$$

The left-hand side of (2.6) can be expanded quite straightforwardly to yield (cf.

Breward (1999))

$$\mathbf{n}\cdot\boldsymbol{\tau}\cdot\mathbf{n} = -p + 2\mu\frac{v_y - (u_y + v_x)\,h_x + u_x h_x^2}{1+h_x^2} \tag{2.13a}$$

$$\mathbf{t}\cdot\boldsymbol{\tau}\cdot\mathbf{n} = \mu\frac{(u_y + v_x)\,(1-h_x^2) - 2\,(u_x - v_y)\,h_x}{1+h_x^2}. \tag{2.13b}$$

Likewise, the right-hand side of (2.6) can be expanded; starting with

$$\boldsymbol{\nabla}_s\cdot\mathbf{u} = \frac{1}{1+h_x^2}\left(u_x + h_x\,v_x + h_x\,u_y + h_x^2\,v_y\right) \tag{2.14a}$$

$$\mathbf{t}\cdot\boldsymbol{\nabla}_s = \frac{1}{\sqrt{1+h_x^2}}\left(\frac{\partial}{\partial x} + h_x\,\frac{\partial}{\partial y}\right), \tag{2.14b}$$

where we have taken advantage of the fact that $\gamma$ is only a function of $x$. Note that (2.14b) simplifies considerably when considering surface variables that have no $y$ dependence. For example, using the notation $\partial_x = \frac{\partial}{\partial x}$, we note that $(\partial_x + h_x\,\partial_y)[u,v] = \partial_x[u_s, v_s]$ where $u_s \equiv u(x, y=h)$.

We non-dimensionalize the equations with substitutions that allow us to retain the more convenient lower-case symbols in the equations to follow:

$$x \to \ell x, \quad y \to \epsilon\ell y, \quad h \to \epsilon\ell h, \quad u \to u_0 u, \quad v \to \epsilon u_0 v,$$

$$t \to \frac{\ell}{u_0}t, \quad \gamma \to \gamma_0 + \Delta\gamma\,\Gamma, \quad p \to \frac{\mu u_0}{\ell\,\epsilon^\alpha}p$$

where $\Delta\gamma$ is a material property such that $\Gamma$ ranges roughly between 0-1 over the length scale $\ell$; and $\epsilon = h_0/\ell$. Note that the correct scaling for the pressure (i.e. the correct value to pick for $\alpha$) and the initially unknown length scale $\ell$ will be set by the specific conditions in the problem, as shown later.

Equations (2.5)(a)-(c) then become

$$u_x + v_y = 0 \tag{2.15a}$$

$$\epsilon^2 R_e \left(u_t + u\, u_x + v\, u_y\right) = -\epsilon^{2-\alpha}\, p_x + \epsilon^2 u_{xx} + u_{yy} - \epsilon^2 S_t \tag{2.15b}$$

$$\epsilon^{2+\alpha}\, R_e \left(v_t + u\, v_x + v\, v_y\right) = -p_y + \epsilon^{2+\alpha}\, v_{xx} + \epsilon^{\alpha}\, v_{yy}. \tag{2.15c}$$

Note that in this form, we have explicitly assumed a vertical film where $x$ is the vertical coordinate as sketched in figure 2.4. The boundary conditions in (2.6) are non-dimensionalized also, to become

$$\begin{aligned} -p + \frac{2\epsilon^{\alpha}}{1+\epsilon^2 h_x^2}\left[v_y - \left(u_y + \epsilon^2\, v_x\right) h_x + \epsilon^2\, u_x\, h_x^2\right] = \\ \frac{h_{xx}}{\left(1+\epsilon^2 h_x^2\right)^{3/2}}\left[\frac{\epsilon^{1+\alpha}}{C_a} + \epsilon^{1+\alpha}\, M_a\, \Gamma + \epsilon^{1+\alpha}\, B_q\, \frac{\partial_x u_s + \epsilon^2\, h_x\, \partial_x v_s}{1+\epsilon^2 h_x^2}\right] \end{aligned} \tag{2.16a}$$

$$\begin{aligned} \frac{\left(u_y + \epsilon^2\, v_x\right)\left(1-\epsilon^2\, h_x^2\right) - 2\left(u_x - v_y\right)\epsilon^2\, h_x}{\sqrt{1+\epsilon^2 h_x^2}} = \\ \epsilon M_a\, \Gamma_x + \epsilon\, B_q\, \frac{\partial}{\partial x}\left[\frac{\partial_x u_s + \epsilon^2 h_x\, \partial_x v_s}{1+\epsilon^2 h_x^2}\right] + \frac{\epsilon}{\mu\, \ell}\frac{\partial \mu^*}{\partial x}\, \frac{\partial_x u_s + \epsilon^2 h_x \partial_x v_s}{1+\epsilon^2 h_x^2}. \end{aligned} \tag{2.16b}$$

Finally the kinematic condition at the interface and the symmetry condition at $y = 0$,

$$v|_{y=h} = h_t + u\, h_x, \quad \text{and} \quad u_y|_{y=0} = 0. \tag{2.17}$$

In writing equations (2.15a)-(2.16b) we made use of the following dimensionless groups

$$R_e = \frac{\rho u_0 \ell}{\mu}, \quad S_t = \frac{\rho g \ell^2}{\mu u_0}, \quad C_a = \frac{\mu u_0}{\gamma_0}, \quad M_a = \frac{\Delta\gamma}{\mu u_0}, \quad B_q = \frac{\mu^*}{\mu\, \ell}.$$

**Pressure scale and the length scale of the dynamic meniscus**

The choice of $\alpha$ is not arbitrary; rather, it is set by the strength of surface stress terms. To illustrate this point, consider the leading order $x$-momentum balance and

tangential boundary conditions, keeping $\alpha$ arbitrary at first and setting $M_a \sim \epsilon^\beta$ while setting $B_q \sim \epsilon$ for simplicity but without loss of generality. At leading and second order in $\epsilon$ we retain from (2.15b) and (2.16b)

$$(x\text{-momentum}) \quad 0 = -\epsilon^{2-\alpha}\, p_x + \epsilon^2 u_{xx} + u_{yy} \tag{2.18}$$

$$(\text{tangential b.c.}) \quad u_y|_{y=h} = \epsilon^{1+\beta}\, \Gamma_x. \tag{2.19}$$

If $\beta = -1$, i.e. in the case of strong Marangoni stresses, we retain a surface stress at leading order of $\epsilon$. Choosing $\alpha = 0$ in this case would lead to a contradiction, since (2.18) would reduce to $u_{yy} = 0$, which, when integrated, cannot simultaneously satisfy the boundary condition at the interface as well as the symmetry condition at $y = 0$. Hence, for $\beta < 0$ we are forced to choose $\alpha = 2$ and we thus recover $u_{yy} = p_x$ at leading order in (2.18). This is the classical lubrication approximation, as also employed in the Landau-Levich problem, and by Frankel. Similarly, if Marangoni stresses are very small, e.g. $\beta \geq 1$, then (2.19) becomes $u_y|_{y=h} = 0$ which is consistent with $u_{yy} = 0$, and indeed inconsistent with $\alpha = 2$. Thus $\alpha = 0$ and $\alpha = 2$ form the distinguished limits for these equations, as pointed out by Breward & Howell (2002).

Although we only used Marangoni stresses as an example, clearly any surface stress that alters the tangential boundary condition to leading order will have the same effect. The results of these ideas are summarized in table 2.3.

To correctly capture the shape and dynamics of a free film connected to a larger reservoir, pressure and capillarity must always balance to leading order in the normal boundary condition. This balance is the case in soap film formation, in plate coating, or even for drainage of a foam lamella into a Plateau border; and it follows directly from the need to match the shape of the film far from the large reservoir to that large

| strength of surface stress | $M_a$ and/or $B_q \sim \epsilon$ | $M_a$ and/or $B_q \sim 1/\epsilon$ |
|---|---|---|
| tangential b.c. | $u_y\|_{y=h} = 0$ | $u_y\|_{y=h} \neq 0$ |
| $x$-momentum | $u_{yy} = 0$ | $u_{yy} = p_x$ |
| $\alpha$ | 0 | 2 |
| flow-type | extensional | shear |

Table 2.3: Strength of the surface stress sets the relevant flow-type.

reservoir. Hence, even though the capillary term is small whenever the curvature is small, it is required for matching purposes to stay in the equations at leading order. Hence we demand that the pressure balances the capillary term in (2.16a), and having chosen $\alpha$ on the basis of surface stresses, $\ell$ is now set as a function of the $C_a$-number;

$$\alpha = 0: \quad \varepsilon \sim C_a \;\Rightarrow \ell \sim \frac{h_0}{C_a} \quad \text{(extensional)} \tag{2.20}$$

$$\alpha = 2: \quad \varepsilon^3 \sim C_a \;\Rightarrow \ell \sim \frac{h_0}{C_a^{1/3}} \quad \text{(shear)} \tag{2.21}$$

Note that the familiar scaling $\ell \sim \ell_c\, C_a^{1/3}$ for the Landau-Levich problem is retrieved. Also note that the dynamic meniscus will tend to be much larger in extensional flow, indeed potentially being many times *larger* than $\ell_c$.

### 2.2.2 Stress balance for extensional flow

Proceeding now with the analysis for the specific case of relatively weak surface stresses, i.e. $\alpha = 0$, we aim to derive the widely used stress balance for a free film with extensional flow. Writing $u, v$ and $p$ in orders of $\epsilon$, i.e.

$$(u, v, p) = (u_0, v_0, p_0) + \epsilon^2 (u_2, v_2, p_2) + \ldots,$$

and expanding (2.15) to leading order ($\epsilon^0$) gives

$$u_{0_x} + v_{0_y} = 0 \tag{2.22a}$$

$$u_{0_{yy}} = 0 \tag{2.22b}$$

$$v_{0_{yy}} = p_{0_y} \tag{2.22c}$$

$$-p_0 + 2v_{0_y} - 2u_{0_y} h_x = \mathcal{C}\, h_{xx} \tag{2.22d}$$

$$u_{0_y} = 0 \tag{2.22e}$$

$$v_0 = h_t + u_0\, h_x \tag{2.22f}$$

where $\mathcal{C} = \epsilon/C_a$. Integrating (2.22b) twice and applying (2.22e) we see that to first order the flow is purely extensional as expected, i.e. $u_0 = u_0(x,t)$. Integrating (2.22a) with respect to $y$, and using (2.22f) we get

$$v_0 = -u_{0_x}\, y + c_1(x,t), \quad \text{but } c_1(x,t) = 0 \quad \text{since } v(0) = 0$$

$$\Rightarrow h_t + (u_0 h)_x = 0 \quad \text{and} \tag{2.23}$$

$$v_0 = -u_{0_x}\, y. \tag{2.24}$$

Proceeding with pressure, since $v_{0_{yy}} = 0$, then $p_0 = c_2(x,t)$ (from (2.22c) and using (2.22d)) so that

$$p_0 = c_2(x,t) = -2u_{0_x} - \mathcal{C}\, h_{xx}. \tag{2.25}$$

To close the equations for $p, u_0$ and $h$, we need one more equation in addition to (2.25) and (2.23), and so we need to go to the next order in the expansion. Assuming that

$R_e \ll 1$ so that inertial terms can be safely neglected, we find

$$u_{2_x} + v_{2_y} = 0 \tag{2.26a}$$

$$u_{2_{yy}} = p_{0_x} - u_{0_{xx}} + S_t \tag{2.26b}$$

$$-p_{2_y} + v_{2_{yy}} = v_{0_{xx}} \tag{2.26c}$$

$$\begin{aligned} -p_2 + 2v_{2_y} - 2u_{2_y}h_x = 2v_{0_x}h_x - 2\left(u_{0_x} - v_{0_y}\right)h_x^2 + \\ \mathcal{M}\,\Gamma h_{xx} - \frac{3}{2\mathcal{C}}h_x^2 h_{xx} + \mathcal{B}\,u_{0_x}h_{xx} \end{aligned} \tag{2.26d}$$

$$u_{2_y} = \mathcal{M}\,\Gamma_x + \mathcal{B}\,u_{0_{xx}} - v_{0_x} + 2\left(u_{0_x} - v_{0_y}\right)h_x \tag{2.26e}$$

$$v_2 - u_2 h_x = 0, \tag{2.26f}$$

where $\mathcal{M} = M_a/\epsilon$ and $\mathcal{B} = B_q/\epsilon$. To complete the stress balance we only need (2.26b) and (2.26e). Integrating (2.26b) once with respect to $y$, then evaluating it at $y = h$ using (2.26e),

$$\left(p_{0_x} - u_{0_{xx}} + S_t\right)h + c_2(x,t) = \mathcal{M}\,\Gamma_x + \mathcal{B}\,u_{0_{xx}} - v_{0_x} - 2h_x\left(v_{0_y} - u_{0_x}\right), \tag{2.27}$$

remembering that $u_y(0) = 0$ for reasons of symmetry so that $c_2 = 0$, and knowing that $\left(v_{0_y} - u_{0_x}\right) = -2u_{0_x}$ and $\left(p_{0_x} - u_{0_{xx}}\right) = -3u_{0_{xx}} - \mathcal{C}\,h_{xxx}$, one arrives at the stress balance

$$\mathcal{M}\,\Gamma_x + \mathcal{B}\,u_{0_{xx}} + 4\left(hu_{0_x}\right)_x + \mathcal{C}\,h\,h_{xxx} - hS_t = 0. \tag{2.28}$$

It is straightforward to put back the dimensions in (2.28), and by also substituting $h \to h/2$ (going from a representation where $h$ is the half-width of the film to one where it is the whole width), we recover the full stress balance and continuity equation

that dictate (to leading order) the evolution of a free film with extensional flow:

$$h_t + (u\,h)_x = 0 \tag{2.29a}$$

$$2\gamma_x + 2\mu^* u_{xx} + 4\mu\,(hu_x)_x + \frac{\gamma}{2} h\,h_{xxx} - \rho g h = 0. \tag{2.29b}$$

**Derivation of the extensional stress balance 'by inspection'**

It can be helpful to 'derive' some of the terms in (2.29) by inspection for a unidirectional flow, rather than by rigorous asymptotics. Figure 2.5 shows a free-body diagram for a small part of the film; surface tension, bulk viscous stresses $\tau_{xx}, \tau_{yy}$ and surface viscous stresses $\tau_s$ (i.e. the deviatoric part of $\boldsymbol{\tau}_s$ below) are indicated. Curvature induced stresses ($\sim h\,(\gamma h_{xx})_x$) and Marangoni stresses ($\sim \gamma_x$) are readily constructed from the sketch. For bulk viscous stresses note that by definition

$$\tau_{xx} = -p_0 + 2\mu\,u_x, \quad \text{and} \quad \tau_{yy} = -p_0 + 2\mu\,v_y = -p_0 - 2\mu\,u_x \tag{2.30}$$

where continuity has been used in the last expression. In an extensional flow, stress in the $y$-direction is constant and (therefore) equal to the ambient pressure $p_a$. Without loss of generality, we can consider ambient pressure to be 0, so that $\tau_{yy} = 0$ and $p_0 = -2\mu\,u_x$, and it thus follows from (2.30) that $\tau_{xx} = 4\mu\,u_x$. Since fluids flow in response to stress gradients, the bulk viscous term in (2.29) is $(h\,\tau_{xx})_x$. Similarly, surface viscous stress depends on surface velocity gradients, i.e. $\tau_s \propto \mu^* u_x$, and hence the surface viscous term in (2.29) looks like $\sim \mu^*\,(u_x)_x$. Note that the factor 2 in the first two terms of (2.29) accounts for the fact that there are two surfaces.

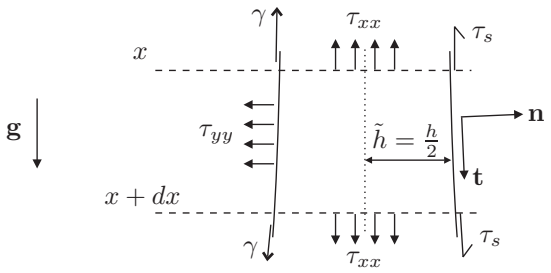


Figure 2.5: Illustration of main sources of stress in a fluid film element. For clarity surface tension is only shown on the left and surface viscous stresses are only shown on the right. Likewise, $\tau_{yy}$ acts equally and oppositely on the right film interface as well.

### A note on $\mu^*$ and the lack of pure dilatation in unidirectional flow

It may be counter-intuitive that even when the flow in a film is extensional in nature, the surface viscosity will always appear as $\mu^*$, as it does in (2.29b), instead of using just the dilatational surface viscosity, $\kappa_s$. Why would a film undergoing extensional flow, clearly having the surface stretch in one direction, retain a shear component of the surface viscosity? The answer is, that since the surface is expanding in one direction only (the direction of film withdrawal), it is not a purely dilatational motion which requires dilation in all directions.

A comparison of the stress tensor for a 3D Newtonian fluid and a 2D 'Newtonian surface' helps reveal why $\mu^*$ involves surface shear viscosity. For a Newtonian fluid, the constitutive equation for the stress is

$$\boldsymbol{\tau} = -\left(p_0 - \kappa\left(\boldsymbol{\nabla}\cdot\mathbf{u}\right)\right)\mathbf{I} + 2\mu\left(\mathbf{E} - \frac{1}{3}\boldsymbol{\nabla}\cdot\mathbf{u}\,\mathbf{I}\right), \tag{2.31}$$

where $\mathbf{E} = \frac{1}{2}\left(\boldsymbol{\nabla}\mathbf{u} + \boldsymbol{\nabla}\mathbf{u}^T\right)$ is the rate of strain tensor and $\kappa$ is the 'second coefficient of viscosity' which relates only to pure dilatation of the bulk fluid (not to be confused with the mean curvature). In the case of incompressible flows, naturally $\boldsymbol{\nabla}\cdot\mathbf{u} = 0$

and the stress tensor simplifies. Scriven (1960) extended the ideas that go into the construction of (2.31) to surfaces. Without doing Scriven's seminal work justice, (2.31) can be recast into a 2D version for surfaces by 'replacing' the internal pressure $p_0$ by surface tension and using surface operators where appropriate, i.e.

$$\boldsymbol{\tau}_s = \left(\gamma + \kappa_s \left(\boldsymbol{\nabla}_\mathrm{s} \cdot \mathbf{u}\right)\right) \mathbf{I}_s + 2\mu_s \left(\mathbf{E}_s - \frac{1}{2}\left(\boldsymbol{\nabla}_\mathrm{s} \cdot \mathbf{u}\right)\, \mathbf{I}_s\right), \tag{2.32}$$

where $\mathbf{I}_s = \mathbf{I} - \mathbf{nn}$ is the surface projection operator, and $\mathbf{E}_s$ is just the 2D version of $\mathbf{E}$, evaluated at the interface. For a unidirectional extensional flow with velocity $u$ in the $x$-direction, $\mathbf{E}_s \propto u_x$ and $\boldsymbol{\nabla}_\mathrm{s} \cdot \mathbf{u} = u_x$ so (2.32) reduces to

$$\boldsymbol{\tau}_s = \left(\gamma + \left(\kappa_s + \mu_s\right) u_x\right) \mathbf{I}_s, \tag{2.33}$$

where $u_x = \frac{\partial u}{\partial x}$. Thus, (2.33) clearly shows why $\mu^*$ will contain contributions from surface shear, even in a unidirectional extensional flow.

### 2.2.3 Stress balance for shear flow

For the case of relatively strong surface stresses, i.e. $\alpha = 2$, we repeat the analysis by starting again at leading order ($\epsilon^0$),

$$u_{0_x} + v_{0_y} = 0 \tag{2.34a}$$

$$0 = -p_{0_x} + u_{0_{yy}} \tag{2.34b}$$

$$0 = -p_{0_y} \tag{2.34c}$$

$$-p_0 = \mathcal{C}\, h_{xx} \tag{2.34d}$$

$$u_{0_y} = \mathcal{M}\Gamma_x + \mathcal{B}\partial_{xx} u_{s,0} + \mathcal{B}\,\tilde{\mu}_x^*\, \partial_x u_{s,0} \tag{2.34e}$$

$$v_0 = h_t + u_0\, h_x \tag{2.34f}$$

where now $\mathcal{C} = \epsilon^3/C_a$, $\mathcal{M} = \epsilon\, M_a$ and similarly $\mathcal{B} = \epsilon\, B_q$. Also, we have kept here the possible gradient in surface viscosity, using the substitution $\mu^* \to \mu^*\,\tilde{\mu}^*$, where $\tilde{\mu}^*$ is a function of $x$, of order unity. From (2.34c) we know that $p_0 = p_0(x)$, and hence we integrate (2.34b) twice with respect to $y$ to get

$$u_0 = \frac{1}{2}\, p_{0_x}\, y^2 + c_1(x). \tag{2.35}$$

By applying the symmetry condition $u_{0_y}|_{y=0} = 0$ and the tangential boundary condition (2.34e), we obtain an expression for $p_{0_x}$ in terms of $\mathcal{M}$ and $\mathcal{B}$. We eliminate pressure as a variable using (2.34d) to get

$$\mathcal{M}\Gamma_x + \mathcal{B}\,(\partial_{xx} u_{s,0} + \tilde{\mu}^*_x\, \partial_x u_{s,0}) + \mathcal{C}\, h\, h_{xxx} = 0, \tag{2.36}$$

which is the stress balance for shear-like flows. Note that it is almost identical to (2.28), except for the lack of the bulk viscous term (and we kept track of surface viscosity gradients here while dropping gravity, without loss of generality). Since the surface velocity is the one that appears in (2.36), we need another expression coupling $u_{s,0}$ to $h$. We do this by recognizing that

$$\begin{aligned}
\int_0^y u(x,y)\, dy &= \bar{u}(x)\, h \\
&\Rightarrow u_0 = \bar{u}(x) + \frac{1}{2} p_{0_x} \left( y^2 - \frac{1}{3} h^2 \right) \\
&\Rightarrow u_{s,0} = u_0|_{y=h} = \bar{u}(x) - \frac{1}{3}\frac{\epsilon^3}{C_a}\, h^2\, h_{xxx}.
\end{aligned} \tag{2.37}$$

Combining continuity with the kinematic boundary condition similar to the case for extensional flow, we retrieve the leading order kinematic boundary condition

$$h_t + (\bar{u}\, h)_x = 0 \tag{2.38}$$

which closes the set of equations for $\bar{u}$, $u_{s,0}$ and $h$. In the case of steady state flows where $\bar{u}\,h = 1$, the system can be reduced to two coupled ODE's for $u_{s,0}$ and $h$,

$$h_{xxx} = \frac{3C_a}{\epsilon^3}\frac{\bar{u} - u_{s,0}}{h^2} \tag{2.39a}$$

$$\mathcal{B}\left(\partial_{xx}u_{s,0} + \tilde{\mu}_x^*\,\partial_x u_{s,0}\right) = \frac{3}{h}\left(u_{s,0} - \bar{u}\right) - \mathcal{M}\,\Gamma_x. \tag{2.39b}$$

## 2.3 Future Directions: Towards Solidification

A particular problem of interest for future research both experimentally and theoretically, is that of solid film formation from a melt. In this case there will be an enormous variation of viscosity over the length of the dynamic meniscus, as the fluid in the film goes from a liquid state to a solid state. The solidification process can be driven by, for example, cooling of a molten liquid in which case it will be necessary to also solve the heat transport equation in addition to the Navier-Stokes equations; or it could be due to, for example, UV-curing of a polymer in the liquid in which case the rate of curing will have to be accounted for. In this section we explore a few key ingredients of these problems, such as the influence of including a spatially varying viscosity, and the issues that arise when coupling with the heat equation.

### 2.3.1 Position-dependent viscosity

Since the Navier-Stokes equations involve the divergence of the stress tensor $\boldsymbol{\tau}$, which in turn involves viscosity, we go back to (2.5a) and (2.5b) and adapt these to

include viscosity gradients. For the divergence of the stress tensor, note that

$$\begin{aligned}\nabla \cdot \boldsymbol{\tau} &= \nabla \cdot \left(-p\,\mathbf{I} + \mu\left(\nabla\mathbf{u} + \nabla\mathbf{u}^T\right)\right) \\ &= -\nabla p + \nabla\mu \cdot \nabla\mathbf{u} + \mu\nabla^2\mathbf{u} + \nabla\mu \cdot \nabla\mathbf{u}^T + \mu\nabla\underbrace{(\nabla \cdot \mathbf{u})}_{=0} \\ &= \begin{bmatrix} -p_x + 2\left(\mu u_x\right)_x + \left(\mu(u_y + v_x)\right)_y \\ -p_y + 2\left(\mu v_y\right)_y + \left(\mu(u_y + v_x)\right)_x \end{bmatrix}\end{aligned} \tag{2.40}$$

Taking this 'new' version of the right hand side of (2.5b), and ignoring inertial terms altogether, the continuity and momentum equations become (non-dimensionalized with $\mu \to \mu_0\,\Lambda$)

$$u_x + v_y = 0 \tag{2.41a}$$

$$0 = -\epsilon^{2-\alpha} p_x + 2\epsilon^2\left(\Lambda\, u_x\right)_x + \left(\Lambda\, u_y + \epsilon^2 \Lambda\, v_x\right)_y \tag{2.41b}$$

$$0 = -p_y + 2\epsilon^\alpha\left(\Lambda\, v_y\right)_y + \epsilon^\alpha\,\left(\Lambda\, u_y + \epsilon^2\Lambda\, v_x\right)_x \tag{2.41c}$$

$$-p + 2\epsilon^\alpha\Lambda\left[v_y - u_y\, h_x + \epsilon^2\left(\ldots\right)\right] = h_{xx}\,\left[\frac{\epsilon^{1+\alpha}}{C_a} + \ldots\right] \tag{2.41d}$$

$$\Lambda u_y\,\left[1 + \epsilon^2\left(\ldots\right)\right] = \epsilon\, M_a\,\Gamma_x + \ldots, \tag{2.41e}$$

where the boundary conditions were written in condensed form, focusing attention on the leading order and order $\epsilon^2$ terms only. Since we've introduced a new scaling for the viscosity, all dimensionless parameters involving viscosity are now based on $\mu_0$.

One might expect that in some cases where $\Lambda_y$ can be assumed to be negligible; in the absence of surface stresses, the flow will once again be of an extensional nature, similar to the flows in for example the glass float process (Scheid *et al.* 2009) or glass capillary fabrication (Howell *et al.* 2007).

### 2.3.2 Coupling with heat transfer

Building on the work from the previous sections, we now turn to heat transfer and the energy equation to keep track of temperature in the film (for viscosity) and temperature at the surface (for heat transfer rates and thermal surface tension gradients). Scheid *et al.* (2009) analyze the relevant set of coupled equations for the case of a cooling sheet of liquid with extensional flow, in the absence of capillary terms (i.e. no Marangoni stresses or curvature terms). The additional ingredient comes only from temperature which is transported according to

$$\rho\, c_p \left(T_t + \mathbf{u}\cdot\nabla T\right) = k\,\nabla^2 T \tag{2.42}$$

$$\text{with boundary condition} \quad k\,\mathbf{n}\cdot\nabla T|_{y=h} = \hbar\left(T|_{y=h} - T_a(x)\right), \tag{2.43}$$

where $\rho$, $c_p$, and $k$ are the density, specific heat capacity and thermal conductivity of the liquid respectively and $\hbar$ is the heat transfer coefficient which will depend on the manner in which the liquid is cooling (i.e. radiative, natural / forced convection, etc.). By defining $T(x, y = h) \equiv T_s(x)$ and making the usual substitutions to non-dimensional variables for $x$, $y$, $u$, $v$ as well as $T \to T_0\, T$ for all temperature variables, (2.42) becomes

$$\epsilon\, P_e \left(T_t + u\, T_x + v\, T_y\right) = \epsilon^2 T_{xx} + T_{yy} \tag{2.44a}$$

$$\frac{1}{\left(1+\epsilon^2\, h_x^2\right)^{1/2}}\left(T_y - \epsilon^2\, h_x\, T_x\right) = -B_i\left(T_s - T_a\right), \tag{2.44b}$$

where $P_e = \rho\, c_p\, u_0\, h_0/k$ is the Péclet number and $B_i = \hbar\, h_0/k$ is the Biot number. Based on estimates of typical orders of magnitude, we proceed to analyze the case of relatively large Péclet numbers when $\epsilon\, P_e \sim 1$. As before, we expand the variables in orders of $\epsilon$, and analyze the film in the case of extensional or shear-like flow.

In the work by Scheid *et al.* (2009) the ansatz is made that the temperature profile is parabolic, i.e. $T(x,y,t) = g(x,t)\,y^2 + f(x,t)$, where the functions $g(x,t)$ and $f(x,t)$ are easily found from (2.44),

$$g(x,t) = -\frac{B_i}{2}\frac{\theta(x,t)}{h(x,t)} \qquad\qquad f(x,t) = T_s + \frac{B_i}{2}\,\theta(x,t)\,h(x,t) \tag{2.45}$$

where $\theta = T_s - T_a$. Whether it is reasonable or not to drop the terms involving $\Lambda_y$ in the momentum equations should depend on the relative strength of longitudinal and transverse temperature gradients. Estimating these gradients in non-dimensional terms, we find

$$\begin{aligned} T_x &\sim B_i\,\theta\,h_x + \partial_x T_s \\ T_y &\sim B_i\,\theta \\ \Rightarrow T_x/T_y &\gg 1 \quad \text{if} \quad \partial_x T_s \gg B_i\,\theta. \end{aligned} \tag{2.46}$$

Assuming initially that we fulfill this requirement, and that longitudinal temperature gradients are still weak enough to prevent strong Marangoni stresses from developing, then we can also assume that we will be in a regime of extensional flow, i.e. $u = u(x,t)$, and the analysis follows closely that of Scheid *et al.* (2009) in terms of coupling the temperature equation to the momentum equations.

# Chapter 3

# Free Film Formation: Experimental

As discussed in the previous chapter, past experiments with films formed by withdrawal of fluid from a bath have focused on soap films as in Lionti-Addad & di Meglio (1992); Adelizzi & Troian (2004); Berg *et al.* (2005). Most of these experiments were conducted with concentrated solutions of the 'mobile' surfactant sodium dodecyl sulfate (SDS). Such soap films could be withdrawn from a bath at speeds between microns and millimeters per minute, and the thickness of the film at $t = 0$ was typically found to scale proportional to the withdrawal velocity $U^{2/3}$. When PEO was added to these solutions of SDS, film thickness scaled anywhere between $\sim U^{2/3} - U^2$ as shown in figure 2.3.

We repeated a number of these experiments, and expanded the explored phase space by changing polymer and surfactant concentrations, wire thicknesses and pulling speeds. Initial experiments with very viscous silicon oils were inconclusive, as the

films either ruptured very quickly (for low viscosity or low withdrawal speeds) or otherwise the combination of viscosity and withdrawal speed was such that $C_a \geq 1$; which is far beyond the range of validity of the analysis in the previous chapter. Subsequently, experiments were performed using aqueous solutions of PEO, with and *without* additional surfactant (SDS). Although PEO itself is slightly surface active, this approach allowed us to probe the specific influence of polymers on film thickness and evolution.

The organization of this chapter is as follows. First, we discuss the non-trivial properties of solutions of PEO in §3.1. Next, a number of experimental methods for determination of film thickness are reviewed, including our final choice of absorbance of transmitted light. Finally, experimental results of initial film thicknesses and film evolution are presented in §3.3. These results have not yet been published elsewhere. We acknowledge Gareth McKinley for helpful discussions and for pointing out useful references regarding the properties of polymer solutions.

## 3.1 Properties of PEO Solutions

Poly(ethylene oxide), or PEO for short, is a popular polymer in research and industry. The lower molecular weights are often referred to as poly(ethylene glycol) (PEG), and can be found for example in humectants and cosmetics. Higher molecular weights find applications in lubricating flows, and turbulence reduction in pipe flow. For an astonishing example of the latter, see the picture in Bailey & Koleske (1976) of flow through fire hoses: when 30 ppm PEO high molecular weight is added to the water, the jet from the fire hose reaches twice as far for a given applied pressure. From a chemical and physical perspective PEO is popular partially due to its ability to dissolve in both aqueous and organic solvents. This property is related to the structure of PEO, the monomer -$[CH_2$-$CH_2$-$O]_n$- is itself amphiphilic.

### Structure of the solution and relaxation times

Depending on the choice of molecular weight and concentration of polymer in solution, the solution may be in one of five regimes as outlined by Graessley (1980) and Heo & Larson (2005). As long as the concentration of polymer stays below 10% by weight, the solutions are either dilute, semidilute unentangled, or semidilute entangled, where 'semidilute' refers to concentrations that are larger than the polymer overlap concentration

$$c^* \equiv \frac{M_\mathrm{w}}{N_A R_g^3}, \tag{3.1}$$

where $M_\mathrm{w}$ is the molecular weight of the polymer, $N_A$ is Avogadro's constant, and $R_g$ is the radius of gyration of the polymer (Rubinstein & Colby 2003; Heo & Larson 2005). Devanand & Selser (1991) characterized aqueous solutions of PEO with $M_\mathrm{w} \sim$

$10^5 - 10^6$, and found

$$R_g = 0.0215\, M_{\mathrm{w}}^{\nu} \quad [\mathrm{nm}] \tag{3.2}$$

where $\nu$ is the excluded volume exponent. The excluded volume exponent depends on solvent quality; for the specific case of aqueous solutions of PEO of relatively high molecular weights, $\nu = 0.583 \pm 0.031$, which qualifies water as a 'good' solvent for PEO (Devanand & Selser 1991).

In the dilute regime ($c < c^*$), hydrodynamic interactions between individual polymer chains dominate the dynamics (Rubinstein & Colby 2003). Zimm's theory of polymer dynamics applies in this limit, and the time scale $\tau_Z$ for a polymer to diffuse a distance $R_g$ is

$$\begin{aligned} \tau_Z &= \frac{R_g^2}{D_Z} = \frac{R_g^2}{k_B\, T/\eta_s R_g} = \frac{\eta_s R_g^3}{k_B\, T} \\ &\approx 75\,\mu\mathrm{s} \text{ (for } M_{\mathrm{w}} = 10^6 \text{ at } 298\ K\text{, in water)} \end{aligned} \tag{3.3}$$

where $D_Z$ is the diffusivity in this limit, which is set by hydrodynamic resistance of the motion of the entire polymer of size $R_g$ through a solvent of viscosity $\eta_s$, and $k_B$ and $T$ are Boltzmann's constant and temperature respectively. In the other limit of concentrated but unentangled polymer solutions, Rouse theory assumes that hydrodynamic interactions on the scale of monomers dominate the dynamics (Rubinstein & Colby 2003). In the Rouse model, the polymer is seen as a chain of $N$ beads connected by springs, and each bead (of size $b$, the Kuhn length) experiences hydrodynamic resistance. Hence the diffusivity of the entire polymer chain is expected to

scale with the number of beads per polymer and the time scale of diffusion is set by

$$\tau_R = \frac{R_g^2}{D_R} = \frac{R_g^2}{k_B\,T/(\eta_s\,N\,b)} = \frac{\eta_s\,R_g^3}{k_B\,T}\left(\frac{M_\mathrm{w}}{M_0}\right)^{1-\nu} \tag{3.4}$$

$$\approx 3\,\mathrm{ms\ for}\ M_\mathrm{w} = 10^6\ \mathrm{at}\ 298\ K \tag{3.5}$$

where $D_R$ is the diffusivity of $N$ beads of size $b$ in a solvent of viscosity $\eta_s$ and we have used $R_g = b\,N^\nu$ with $N = M_\mathrm{w}/M_0$, and $M_0$ is the mass of the hydrodynamically independent unit ($M_0 = 137$ for PEO, or about 3.5 monomers (Rubinstein & Colby 2003)).

At the molecular weights and concentrations that we chose to use in our experiments, the PEO solutions are considered to be semidilute unentangled solutions (Graessley 1980; Heo & Larson 2005). In this regime, the dynamics are modeled best by a combination of the Rouse and Zimm models. The polymer can be seen as a collection of 'blobs' of length scale $b < \xi < R_g$, where each 'blob' primarily contains a single polymer chain. Within the 'blob', hydrodynamic interactions between different monomers are important, i.e. the Zimm model for dilute solutions works well on length scales smaller than $\xi$. On the scale of several (unentangled) 'blobs', hydrodynamic interactions on the monomer scale are negligible with respect to interactions between 'blobs', i.e. the dynamics on this larger scale are better captured by the Rouse model (Rubinstein & Colby 2003; Heo & Larson 2005). As a result, the time scale of relaxation of an entire chain becomes (see Rubinstein & Colby (2003) for

details)

$$\begin{aligned} \tau_{su} &= \frac{\eta_s R_g^3 N^{2-3\nu}}{k_B T} \phi^{(2-3\nu)/(3\nu-1)} \\ &\approx \frac{\eta_s R_g^3}{k_B T} \left(\frac{M_\mathrm{w}}{M_0}\right)^{2-3\nu} c^{(2-3\nu)/(3\nu-1)}, \\ &\approx 0.04 - 0.35\,\mathrm{ms} \text{ for } c \text{ from } 0.01 \text{ to } 10\% \end{aligned} \tag{3.6}$$

where $\phi$ is the volume fraction occupied by the polymer ($= c/\rho$, recognizing that $\phi = 0.1$ corresponds to $c = 10\%$ by weight in solutions where the density varies very little).

There is a large range of actual relaxation timescales reported in the literature, that do not always coincide well with theory. For example, Ortiz *et al.* (1994) calculate that for a 2% solution of PEO of $M_\mathrm{w}$ $10^6$ in water, the 'characteristic time' is about 9 ms, suggesting Rouse-like dynamics rather than semidilute unentangled dynamics. Further experimental evidence for much longer relaxation times is found for instance in the work by Lance-Gomez & Ward (1986). Lance-Gomez & Ward subjected high concentration (1-5%) PEO solutions of relatively high $M_\mathrm{w}$ (in the range 0.6-5 $\times 10^6$) to gentle shearing flows in a cone - plate geometry rheometer. After shearing for some time at typical shear rates between 1-5 $\mathrm{s}^{-1}$, they would stop the cone from rotating, and read out the residual stress in the fluid which was interpreted as an apparent viscosity. Decay times of this apparent viscosity ranged from 1-100 seconds; many orders of magnitude larger than the longest timescale of relaxation according to even the Rouse model. Relaxation depended strongly on concentration of PEO, for example $\tau_r \sim 59$ s for a 5% solution of $M_\mathrm{w}$ 900 kg/mol, while it was only $\tau_r \sim 1$ s for a 2% solution of the same polymer. Likewise, Lance-Gomez & Ward (1986) show that adding salt and/or an anionic surfactant can have a significant effect on $\tau_r$,

although less pronounced than the effect of concentration. On a cautionary note, Lance-Gomez & Ward (1986) point out that the variability in stress relaxation rates was larger between different batches of the same polymer weight and concentration, than it was between batches of different molecular weights.

Some other observations regarding PEO solutions are repeated here for the sake of completeness. All of this information is due to Devanand & Selser (1991) and Heo & Larson (2005) unless indicated otherwise. These authors found the entanglement concentration $c_e$,

$$\begin{aligned} c_e &= \frac{n_e^{(3\nu-1)}}{M_{\rm w} A_2} \quad \text{with} \\ n_e &= \frac{M_e}{m_0} \quad \text{and} \quad M_e = 4400 \text{ g/mol, and} \\ A_2 &= 1.84 \times 10^{-2} M_{\rm w}^{-0.20\pm0.06} \quad \text{ml.mol/g}^2, \\ \text{so} \quad c_e &\approx 2.7 \text{ g/dl or } 2.7\% \text{ for } M_{\rm w} = 10^6 \end{aligned} \tag{3.7}$$

where $n_e$ is the number of monomers in a 'blob' that becomes entangled, $M_e$ is the weight of that blob, and $m_0$ is the monomer weight; $A_2$ is the second virial coefficient. For convenience, we noted the concentration in units of g/deciliter, since that is numerically the same as concentration by weight for most aqueous solutions. Devanand & Selser (1991) also measured the hydrodynamic radius of PEO along with its diffusivity, and found

$$R_h \equiv \frac{k_B T}{6\pi\eta_s D_0} = 0.145\, M_{\rm w}^{0.571\pm0.009}, \tag{3.8}$$

so that the diffusivity $D_0 \propto M_{\rm w}^{-0.57}$, of order $10^{-7}$ cm$^2$/s for $M_{\rm w}$ around $10^5$. As more and more PEO is dissolved in water the density stays remarkably constant, but the

index of refraction $n$ does increase:

$$\frac{\mathrm{d}n}{\mathrm{d}c} = 0.135 \quad [\mathrm{ml/mg}] \text{ at } \quad \lambda = 632.8 \text{ nm}. \tag{3.9}$$

At the concentrations we used there is no significant change in reflectivity and/or absorbance coefficient, as confirmed by control experiments.

**Shear viscosity**

In this section, we denote viscosity by $\eta$ to be aligned with the convention in polymer literature. Note however that in all other parts of this dissertation, viscosity is denoted by $\mu$.

It can be shown (see e.g. Heo & Larson (2005)) that for solutions in the semidilute unentangled regime, the viscosity scales as

$$\eta_{Rouse} = \eta_s \left[1 + \left(\frac{c}{c^*}\right)^{1/(3\nu-1)}\right]. \tag{3.10}$$

Furthermore, the intrinsic viscosity at zero shear $[\eta]$ is directly related to $c^*$ through (cf. Heo & Larson (2005); Rubinstein & Colby (2003))

$$c^* = \frac{4.6}{[\eta]}, \quad \text{where } [\eta] \text{ is defined by} \tag{3.11}$$

$$\eta = \eta_s \left(1 + [\eta]\, c + o(c^2)\right). \tag{3.12}$$

Hence, we can directly find $\eta$ by substituting (3.1) and (3.2) into (3.11). The viscosity of the solution is thus predicted to depend on concentration and molecular weight according to

$$\eta = \eta_s \left(1 + 2.753 \times 10^{-4}\, M_{\mathrm{w}}^{3\nu-1}\, c\right) \quad [c \text{ in g/dl},] \tag{3.13}$$

although there is some ambiguity as literature sources report a variety of intrinsic viscosities, e.g.

$$\begin{aligned} [\eta] &= 2.75 \times 10^{-4}\, M_{\mathrm{w}}^{0.749} \quad \text{(as in (3.13))} \\ [\eta] &= 1.22 \times 10^{-4}\, M_{\mathrm{w}}^{0.78-0.80} \quad \text{(Bailey \& Koleske 1976)} \\ [\eta] &= 7.20 \times 10^{-4}\, M_{\mathrm{w}}^{0.65} \quad \text{(Tirtaatmadja } et\ al. \text{ 2006)} \end{aligned} \tag{3.14}$$

In the last reference the regression also included mixtures of glycerol and water as solvents. When either surfactant or salt is added, these intrinsic viscosities are altered, as discussed below.

In figure 3.1, we compare the theoretical viscosity to the viscosities measured for the solutions we used in our experiments. Note that solutions of PEO are known to be shear thinning and extensional thickening; the viscosities reported in figure 3.1 were measured using a cone and plate geometry at shear rates of 10 $s^{-1}$ or less if the solution permitted (lower shear rates led to more uncertainty in the measurement). These shear rates are low enough that they correspond to 'zero-shear' viscosities reported elsewhere. Later viscosity measurements with a double-walled Couette geometry, sweeping shear rates from $10^{-3}$ to $10^{4}$ $s^{-1}$ confirmed that the solutions used in our experiments are essentially Newtonian between shear rates from (10)-1000 $s^{-1}$. The lower bound is written in brackets to indicate the lack of confidence in the rheometer's ability to accurately measure viscosities below this shear rate. In actual soap films, we have typical withdrawal velocities $u_0 \sim 1$ mm/s, thicknesses $h \sim 1$ $\mu$m and capillary lengths $\ell_c \sim 2.5$ mm. Hence, if the flow is found to be shear-like, an upper bound on the shear rate may be estimated as $u_0/h \sim 10^3$ $s^{-1}$. Likewise, if the flow is found to

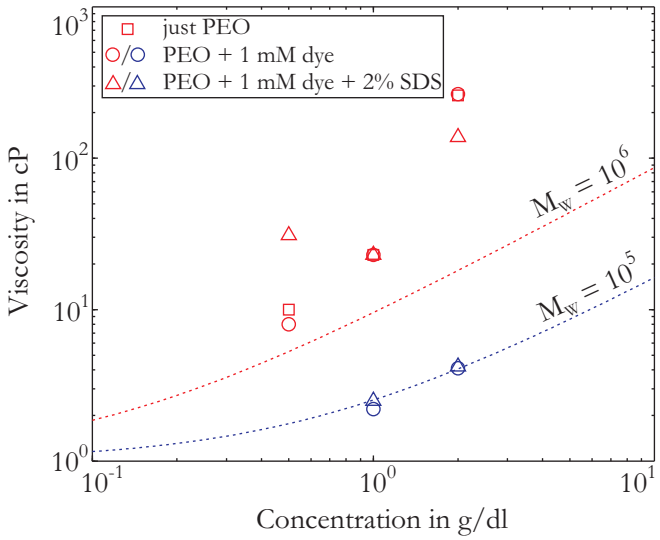


Figure 3.1: Viscosity of various aqueous PEO solutions; the dashed lines correspond to (3.13) for two different molecular weights, and the symbols are measured values. Note that (3.13) is strictly only valid for very small $c$, so the dashed lines serve as a lower limit of possible viscosities. Red corresponds to $M_w = 10^6$ and blue corresponds to $M_w = 10^5$.

be extensional in nature, a typical extension rate could be constructed as $u_0/\ell_c \sim 1$ $s^{-1}$.

### Extensional viscosity

When PEO solutions are subjected to straining or extensional flows, the apparent viscosity can increase by a factor of about 100 or more (Amarouchene *et al.* 2001; Cooper-White *et al.* 2002). These large Trouton ratios or extensional viscosities are typically measured at relatively large extension rates and low polymer concentrations. For example, in recent work by Tirtaatmadja *et al.* (2006) large effective relaxation times were measured when stretching thin liquid bridges of elastic fluid (at very low concentrations of PEO, $c < c^*$). These unexpectedly large relaxation times were attributed to molecular interactions between polymers that are not accounted for in

either the Zimm or Rouse models. Such strong interactions occur in areas of high extensional strain, e.g. in the neck of a stretching liquid bridge. Their results cannot simply be extrapolated to higher concentrations, but it is worth noting that within the small range of concentrations and molecular weights that were probed, the effective relaxation time scale increased by a factor of 13 in some cases.

The earlier work by Amarouchene *et al.* (2001) showed similarly strong extensional thickening of PEO solutions in stretching flows. In particular, Amarouchene *et al.* (2001) note that the polymer interacts strongly with the flow when the stretching rate $\dot{\epsilon}$ exceeds the relaxation rate of the polymer, i.e. $\dot{\epsilon} > 1/\tau_Z$ forcing a coil-stretch transition. A specific measurement of extensional viscosity, Trouton ratios, or relaxation times at the high concentrations used in our experiments (0.5-2% by weight, $M_\mathrm{w}$ from $10^5$ to $10^6$ g/mol) was not found in the literature.

**Solution preparation & degradation**

Solutions of PEO can degrade over time (Bailey & Koleske (1976); Devanand & Selser (1991)) especially with UV-light and/or bacterial growth. A number of organic solvents (isopropanol, chloroform, etc.) can be added to aqueous solutions to counter both bacterial growth and the formation of peroxide radicals (e.g. by UV light) which can cleave polymer chains. Degradation is worse in the presence of heavy metal ions and/or strong acids, and at some large shear rates ($\sim 1000\ \mathrm{s}^{-1}$) mechanical degradation has also been observed (Bailey & Koleske 1976).

On the topic of solution preparation, Bailey & Koleske (1976) note that the inverse solubility of PEO (it is less soluble at high temperatures) can be used to disperse PEO

powder in hot water such that it will indeed disperse rather than clump together and slowly dissolve. When the temperature is then dropped e.g. by addition of colder water, the individual PEO powder grains rapidly dissolve without clumping. This technique was used with success a number of times for our experiments, but in any case the PEO solutions had to be stirred continuously for multiple days to fully dissolve.

In our experiments, no special precautions were taken to prevent degradation. Measurement of the pH showed that despite the vernacular name of the blue dye used in our experiments (erioglaucine disodium salt is also known as "Acid Blue 9"), solutions never exhibited a pH below 6 so degradation by strong acid action was unlikely. Regularly spaced shear viscosity measurements (e.g. one week apart) of PEO solutions with dye, and with or without surfactant could be used to study in more detail if degradation is a relevant issue in our experiments. Viscosity measurements which were performed serendipitously for the same solutions multiple weeks apart showed less than 5% variation, but later shear viscosity measurements with equivalent batches of liquids showed larger deviations which could be attributed to either small differences in the preparation of the solution, operation of the rheometer, or the effects of uncalibrated degradation. As Lance-Gomez & Ward (1986) point out somewhat dryly,

> "The entire interactive system with salts, surfactants, and PEO is probably a complex structure, highly shear dependent and variable with temperature and concentration. Anomalous results coming from viscosity measurements on such systems are the rule rather than the exception."

Since the solutions we prepared typically had either a dye, or a dye and an anionic surfactant in them, slightly anomalous results are indeed to be expected, and it is

difficult to attribute any given viscosity measurement to any one underlying cause. We therefore decided to measure the viscosity of the solutions as close as possible to the day that they were used to make films.

### 3.1.1 PEO with surfactant

The addition of surfactants to solutions of PEO has a profound effect on the solution properties. For example, adding sodium dodecyl sulfate (SDS) will alter the viscosity, solubility, and surface tension (Chari *et al.* 1994; Smitter *et al.* 2001; Péron *et al.* 2007; Torres *et al.* 2008).

When SDS is first added to a PEO solution, the polymer and surfactant molecules do not interact as they are in dilute solution. As the concentration of SDS ($c_{\mathrm{SDS}}$) is increased, some of the SDS starts to form micelles in solution, and/or PEO/micelle complexes as sketched in figure 3.2. The process of complexation is enthalpically driven for high $M_{\mathrm{w}}$ polymers as little entropy is lost by forming complexes (long polymers have low translational / rotational entropy to begin with), and there is an enthalpic gain (Bailey & Koleske 1976). In the absence of PEO, the concentration at which SDS molecules start to aggregate into micelles (cmc: critical micelle concentration) is 7.2 mM in water. In the presence of PEO, however, the concentration at which aggregation starts (cac: critical aggregation concentration) is typically lower than the cmc. The cac depends on PEO concentration, e.g. it is 5.1 mM for a 0.025% solution of PEO with $M_{\mathrm{w}} = 4 \times 10^6$ (Torres *et al.* 2008).

As SDS molecules begin to associate themselves with the PEO, the polymer uncoils or swells (see e.g. Chari *et al.* (1994); Smitter *et al.* (2001); Torres *et al.* (2008)).

Consequently, the viscosity increases and the solubility tends to decrease. As more and more surfactant is added, the polymer becomes saturated with surfactant micelles (at the so-called 'polymer saturation point' or psp, typically ∼10 mM), and there is evidence to suggest that the viscosity peaks at this point (Chari *et al.* 1994). Further addition of SDS increases the ionic strength of the solution (since SDS dissociates in water into a $Na^+$-ion and the anionic surfactant chain), which reduces the Debye screening length, screening electrostatic repulsion between the aggregated micelles on the polymer chain, and allowing the polymer coil to shrink or collapse to some extent. Consequently, the viscosity of the solution decreases, although Cooper-White *et al.* (2002) suggest that this is due more to a conformational change in the PEO-SDS complex than to straightforward coil collapse and electrostatic screening. In the case of SDS, a ten or hundred-fold increase of SDS concentration beyond the psp, the SDS micelles begin to re-arrange into rod-like rather than sphere-like micelles, and the viscosity of the solution increases dramatically (Chari *et al.* 1994).

The polymer saturation point is essentially independent of molecular weight, but is a linear function of the polymer concentration by weight. In the absence of salt, Chari *et al.* (1994) and Smitter *et al.* (2001) find

$$\text{psp} = 11 + 126.5\, c_{\text{PEO}} \quad \text{and} \tag{3.15}$$

$$\text{psp} = 8.2 + 55\, c_{\text{PEO}}, \tag{3.16}$$

respectively.The intrinsic viscosity of PEO + SDS solutions depends on surfactant

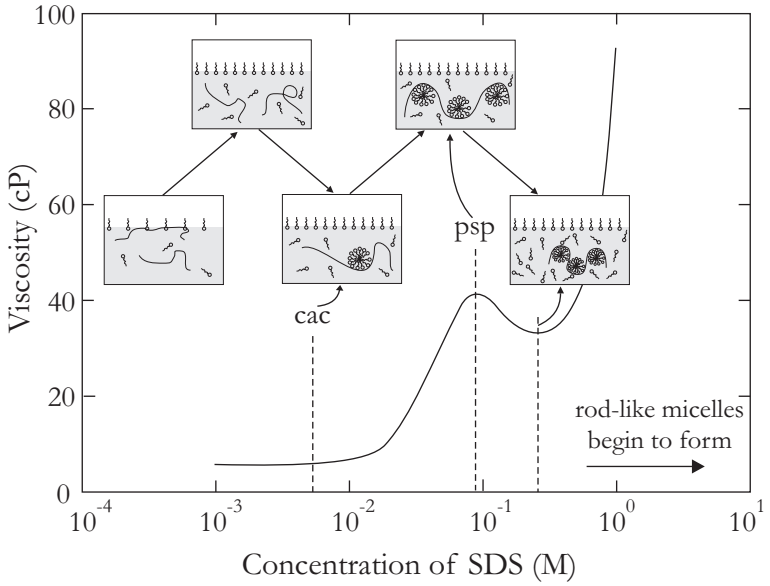


Figure 3.2: Sketch of PEO + SDS complexation at increasing concentrations of SDS. This sketch is based on experimental data from Chari *et al.* (1994), interpretation of surface rheometry data from Péron *et al.* (2007) and interpretations of bulk measurements by Smitter *et al.* (2001). The curve is not an exact representation of measured data, but approximately follows the data obtained by Chari *et al.* (1994) for a 0.5 % solution of PEO of $M_{\mathrm{w}}$ 800k.

(all reported in [dl/g]);

$$
\begin{aligned}
[\eta] &= 2.15 \times 10^{-4}\, M_{\mathrm{w}}^{0.74} \quad \text{without SDS} \\
[\eta] &= 0.69 \times 10^{-4}\, M_{\mathrm{w}}^{0.94} \quad \text{with SDS at } c_{\mathrm{SDS}} = \text{psp} \\
[\eta] &= 1.60 \times 10^{-4}\, M_{\mathrm{w}}^{0.84} \quad \text{with SDS at unknown } c_{\mathrm{SDS}},
\end{aligned}
$$

where the first two are due to Chari *et al.* (1994) and the last is due to Francois *et al.* (1985). In other words, when surfactant is added, the excluded volume exponent increases to roughly $\nu = 0.65$ (0.58 without SDS), which is another indication of polymer swelling.

**Extensional viscosity**

The influence of surfactant on *extensional* rheology was investigated by e.g. Smitter *et al.* (2001) and Cooper-White *et al.* (2002). Although Smitter *et al.* (2001) and Cooper-White *et al.* (2002) used different techniques, their results agree qualitatively. Upon addition of SDS to a PEO solution, extension thickening sets in at a lower extension rate and thickening 'strength' is larger also. The technique used by Smitter *et al.* (2001) did not allow them to measure Trouton ratios directly, but they reason that the onset of extensional thickening probably corresponds to an increase in (dis)entanglement time of the polymer/surfactant complexes. If the inverse strain rate is taken as the typical entanglement time, then these are on the order of 0.1-10 ms for PEO concentrations up to about 0.05% (at $M_{\mathrm{w}}$ of $4 \times 10^6$). Actual Trouton ratios were measured by Cooper-White *et al.* (2002), and they found ratios up to ∼100 for extension rates of order $\sim 10^2 - 10^4$ s$^{-1}$, for solutions of 0.15% PEO of $M_{\mathrm{w}} \sim 10^6$ and SDS concentrations ranging from 8-30 mM.

The solutions we used have far higher concentrations of polymer (1-2%), but are exposed to far smaller extension rates, of order $u_0/\ell_c \sim 1\ \mathrm{s}^{-1}$. Unfortunately no data could be found in the literature spanning this regime of low extension rates at high concentrations; except in settings of shear flow, such as in the work by Lance-Gomez & Ward (1986). Their experiments involved the surfactant alkylbenzene sulfonate (ABS) which, like SDS, is anionic. They found that the addition of ABS either increased stress relaxation time scales in the case of fairly monodisperse polymer solutions, or decreased the relaxation time in highly polydisperse polymer solutions. How this ambiguous effect can be explained in terms of polydispersity, and how it may translate to PEO-SDS complexes remains uncertain. In any case, the relaxation times measured by Lance-Gomez & Ward are of the order of tens of seconds.

**Interfacial properties**

Poly(ethylene oxide) by virtue of its amphiphilic nature also exhibits surfactant-like behaviour at certain concentrations and molecular weights. A number of studies have specifically addressed interfacial activity of PEO with and without the presence of surfactant, see e.g. the work by Cooper-White *et al.* (2002); Gilányi *et al.* (2006); Péron *et al.* (2007) and references therein. From a variety of techniques employed over the past 50 years or so, it has become clear that PEO itself exhibits some level of surface activity, reducing the surface tension of water from roughly 72 mN/m down to about 60 mN/m. The rate at which it does so is controlled by diffusion of the surfactant to the interface, as the adsorption at the interface is quite rapid (Cooper-White *et al.* 2002). Dynamic surface tension measurements reveal that it takes on

the order of 1000 seconds for a new air/solution interface to reach its equilibrium tension in the presence of $4 \times 10^{-3}$ g/l PEO of $M_w = 8000$ (Gilányi *et al.* 2006). That same work demonstrated that the equilibrium surface tension of PEO solutions is remarkably independent of PEO concentration, as long as the molecular weight is above $\sim 10^5$. Tirtaatmadja *et al.* (2006) measured the dynamic surface tension for high $M_w$ polymer solutions at concentrations up to 0.1% by weight. Equilibrium surface tension was reached within 1 s for these solutions. Later research showed that when SDS is added to these PEO solutions, it preferentially displaces the PEO at the interface even at relatively low concentrations of SDS (Péron *et al.* 2007), although it must be noted that those measurements were done in the presence of 0.1 M NaBr. For another comparison of the relevant time scales involved in reaching equilibrium surface tensions, note that Cooper-White *et al.* (2002) used the maximum bubble pressure method to determine that an aqueous solution of just SDS reaches its equilibrium surface tension after about 10 s. Upon adding 0.15% PEO ($M_w = 3 \times 10^5$), these time constants were only changed by a small amount. Cooper-White *et al.* (2002) used a fitting function due to Hua & Rosen (1988) to determine the time scale of surface tension equilibration,

$$\gamma(t) - \gamma_e = \frac{\gamma_s - \gamma_e}{1 + (t/t^*)^n} \tag{3.17}$$

where $\gamma$ is the surface tension at time $t$, $\gamma_e$ is the final equilibrium surface tension, $\gamma_s$ is the solvent surface tension and $t^*$ and $n$ are fitting parameters. For solutions of 80 mM SDS without PEO, they find $n = 0.50$ and $t^* = 0.50$ ms, whilst the addition of PEO results in $n = 0.49$ and $t^* = 0.48$ ms. In our experiments we use 2%SDS, which corresponds to about 70 mM. Given the results of Gilányi *et al.* (2006), Péron

*et al.* (2007) and Tirtaatmadja *et al.* (2006), we expect equilibrium to be reached even faster for higher concentrations of PEO and indeed pendant drop measurements taken over time periods of several minutes never showed an appreciable deviation from the equilibrium surface tension of about 60 mN/m.

### 3.1.2 PEO with surfactant and salt

Adding salt (for example in the form of a dye) to the already complicated solutions of surfactant and polymer has a number of effects. For one, salt changes the ionic strength of the solution, and so it is observed that both the cmc (in absence of polymer) and the cac decrease roughly as the square root of salt concentration, which is reminiscent of the effects of Debye screening in the reactive drop spreading recoil process. Torres *et al.* (2008) measured the cac to be only 0.88 mM for a solution of 0.025% PEO ($M_{\mathrm{w}} = 4 \times 10^6$) and 0.1 M NaCl (was 5.1 mM without salt). For comparison, the cmc in the absence of polymer drops from 7.2 mM without salt to 1.8 mM in a 0.1 M NaCl solution. In the absence of surfactant, the addition of salt to a solution of PEO results in shrinking of the PEO coils, as the electronegativity of the oxygen atoms is effectively screened between monomers. The viscosity therefore decreases, but so does the temperature at which the polymer will tend to precipitate out of solution Bailey & Koleske (1976). In fact, it is not the ionic strength of the solution which dictates changes in viscosity and precipitation temperature, but rather it depends on the specific anion in the salt. Similar to the Hofmeister series of ions for protein solubility, PEO is most sensitive to the anions $OH^-$, $F^-$,$CO_3^{2-}$, and so forth; see Bailey & Koleske (1976) for a full list.

Francois *et al.* (1985) and Torres *et al.* (2008) demonstrated that for very low concentrations of polymer and high concentrations of salt, there is a minimum in the solution intrinsic viscosity right around the surfactant cac, but much below the psp. The psp itself is seen to shift to lower concentrations of SDS with increasing salt concentration (Francois *et al.* 1985), although there seems to be some disagreement in the literature about this. Measurements done at much higher concentrations of polymer by Chari *et al.* (1994) show that the psp is 'erased' entirely by the addition of 0.1 M salt. The disagreement may stem from the disparity in polymer concentrations; and indeed it could be a manifestation of the non-linear effect of concentration on viscosities. In any case, the dye that was used in the film pulling experiments (erioglaucine disodium salt, also known as Acid Blue 9 or FD&C Blue 1) was never used at concentrations that would have a noticeable effect on the solution properties (typically $\sim$1 mM). Measurements of surface tension and viscosity showed no discernable difference between solutions with and solutions without dye.

**Extensional viscosity**

Lee & Berman (1996) measure the extensional viscosity of PEO with some dyes and salts. They find in general that addition of either salt or dye is detrimental to the extensional thickening of these solutions; i.e. it has an opposite effect from addition of SDS. However, for one particular dye, namely Congo Red, they found a significant enhancement of extensional viscosity. No literature was found that specifically describes erioglaucine disodium salts in relation with PEO.

## 3.2 Techniques to Measure Thin Films

All measured film thicknesses to date, as shown in figures 2.2 and 2.3 were measured using interferometry. This technique was explored for the current set of experiments as well, but found to be inadequate when films are too thick, or when they exhibit strong convective flows. Also, the final thickness of the film just prior to rupture must be known to allow reconstruction of the thickness at all previous times. For very viscous films and films made without surfactant, most of these conditions are not met. It was therefore necessary to test a number of different possible methods to measure film thickness. Here, we briefly review the classic interferometric methods, as well as capacitive and absorption methods. Each method has its own advantages and pitfalls, as detailed in the next sections.

### 3.2.1 Interferometry

A number of possible interferometric setups are sketched in figure 3.3, including back-reflection (A), Mach-Zehnder (B) and Michelson (C). Back-reflection is the method most often associated with soap film thickness measurements, (see e.g. Lionti-Addad & di Meglio (1992); Adelizzi & Troian (2004); Berg *et al.* (2005)) and it is elegant in its optical simplicity. The laser hits the front surface of the film, where a small percentage reflects back to the source and is deflected to a detector via the beam-splitter. Some of the light that is transmitted through the film then reflects off the back surface of the film, and returns to the detector also. This light has therefore passed through the film twice, such that the optical path length difference between the two reflected beams is exactly $2nh$ where $n$ is the refractive index of the film and

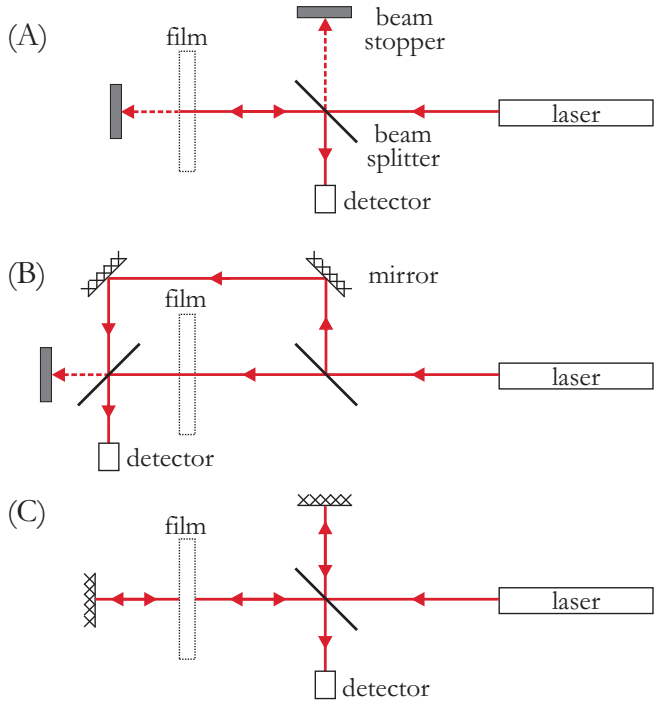


Figure 3.3: Common geometries for interferometric setup: (A) Back-reflection, (B) Mach-Zehnder, and (C) Michelson interferometer. See text for details.

$h$ its thickness. One drawback of the back-reflection method is that it uses only a few percent of the laser power, and can therefore be very sensitive to ambient light. The signal-to-noise ratio of the detected light is typically enhanced using a lock-in amplifier (Lionti-Addad & di Meglio 1992; Adelizzi & Troian 2004; Berg *et al.* 2005).

In both the Mach-Zehnder and Michelson geometries, roughly half the laser light reaches the detector where a reference beam interferes with the beam that passes through the film. These geometries are both quite insensitive to the angle of incidence of the light on the film, which is an additional advantage of geometries involving transmittance rather than reflectance. The Mach-Zehnder geometry has been used in soap film experiments to study 2D turbulence, where slight changes in film thickness were tracked by rapidly adjusting the optical path length of the reference beam using piezo-activated mirrors (Greffier *et al.* 2002) such that the signal at the detector remained constant. We initially chose to measure film thickness using the Michelson geometry, which minimizes optical components and allows two passes of the light through the film, thus doubling the sensitivity of the detector.

In all interferometric setups, as the film thickens or thins, the relative optical path length changes and the detector records alternatingly constructive and destructive interference. One can reconstruct film thickness evolution back to the time where the film was first made by counting interference peaks (see figure 3.4). The film thickness is then calculated as

$$h = \frac{\lambda}{4n} + \frac{\lambda(N-1)}{2n}, \tag{3.18}$$

where $N$ is the $N^{th}$ peak in figure 3.4A starting with the last one (see e.g. Adelizzi & Troian (2004)). As mentioned before, this method never allows one to determine the

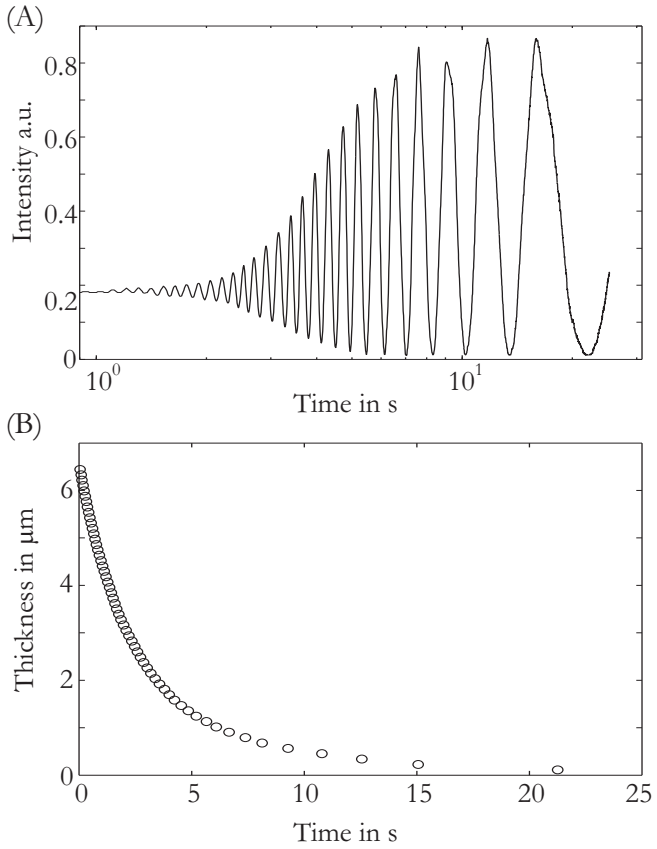


Figure 3.4: A. Typical signal as obtained from an interferometric measurement of film thickness and B. reconstructed drainage curve with assumed film rupture at $\lambda/4$ and $t = 0$ corresponding to the first maximum in $I$. This particular film was made with Si-oil of 30,000 cSt, with a pulling speed of 0.27 mm/s.

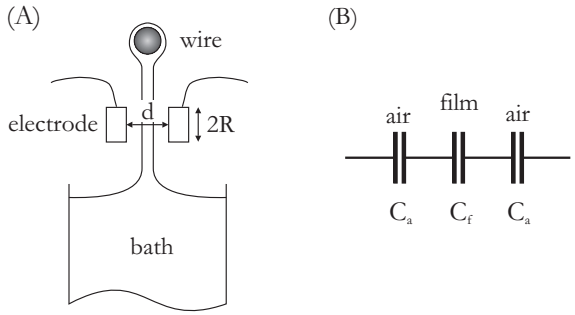


Figure 3.5: A. Sketch of capacitive film thickness measurement technique. B. Modeling the system as three capacitors in series.

absolute thickness of the film from a single intensity measurement. Rather, it allows one to monitor the drainage of the film until it ruptures. In the case of steady soap films, drainage will eventually lead to a black film, with maximum thickness $h < \lambda/4$ (Mysels *et al.* 1959; Isenberg 1992). However, not all soap films are so stable that they reach the black-film limit without premature rupture, and not all liquids make films that are stable down to the black film limit in the first place. In fact, films made of polymer solutions never evolved down to stable black films, and because of clear convective motions that disturbed classical optical interference methods of measuring film thickness, alternative methods were explored.

### 3.2.2 Capacitance

Since water has a large dielectric constant ($\epsilon_r = 81$), capacitive methods are sometimes used to determine the thickness (or height) of a water layer, or to measure foam density (e.g. Hutzler *et al.* (1995)). With a setup such as the one sketched in figure 3.5 it may be possible to measure absolute film thicknesses by capacitance. The system can be described as three capacitors in series, two with the dielectric constant of air,

and the middle one with the dielectric constant of the film material. Assuming initially that the capacitors are essentially thin plate capacitors with circular electrodes of radius $R$ and separation $d$, the capacitance should be

$$C_0 = \frac{\epsilon\, A}{d} = \epsilon_0 \epsilon_r \frac{\pi R^2}{d}, \tag{3.19}$$

where $\epsilon_0$ is the permittivity of free space and $\epsilon_r$ is the dielectric constant of the material between the capacitor plates. The total capacitance of the air-film-air system (see figure 3.5) is therefore

$$C_{tot} = \left( \frac{2}{C_a} + \frac{1}{C_f} \right)^{-1}, \tag{3.20}$$

where $C_f$ is the film capacitance, and $C_a$ is the capacitance of the air gaps, assumed to be of equal gap width for now. These capacitances are readily calculated using (3.19) to be

$$\begin{aligned} C_a &= \frac{2\epsilon_0 A}{d-h}, \quad \text{and} \quad C_f = \frac{\epsilon_0 \epsilon_r A}{h} \\ \text{so that} \quad C_{tot} &= \frac{\epsilon_0 \epsilon_r A}{h + \epsilon_r\,(d-h)}, \end{aligned} \tag{3.21}$$

where $d$ is the total gap width and $h$ is the film thickness. The thickness should therefore be directly obtainable from (3.21) as long as $d$ and $\epsilon_r$ are known to sufficient accuracy. The expected sensitivity of this method is found by inspecting the derivative of $C_{tot}$ with respect to $h$,

$$\frac{\mathrm{d}C_{tot}}{\mathrm{d}h} = C_{tot}^2 \frac{(\epsilon_r - 1)}{\epsilon_0 \epsilon_r A}, \tag{3.22}$$

i.e. sensitivity scales as $A/d^2$. It is a mechanical challenge to develop a setup where $d$ is kept as small as possible, while allowing the sensor to move down with the bath of liquid as the film is drawn, to let it eventually settle at a given vertical position

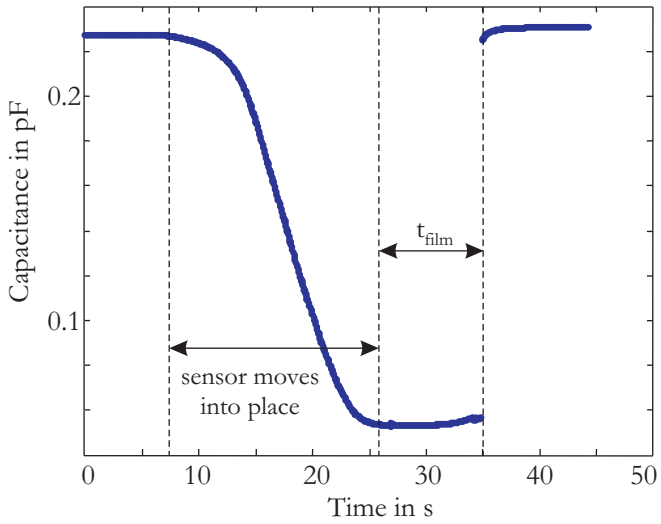


Figure 3.6: Typical result from capacitance measurement. Initial drop in capacitance corresponds with the capacitive sensor moving into place as the bath moves down. A short-lived film is observed followed by rupture. For this particular case the liquid is 1% PEO of $M_w = 10^6$ (no dye), and the pulling speed is 0.47 mm/s.

to interrogate the film thickness over time. The capacitor area $A$, restricts the 'spot' size of the measurement and causes the capacitive measurement to be an average over the area $A$.

Initial testing indicated that films of (silicon) oils did not produce a strong enough capacitive signal to be recorded by the (very) sensitive sensor; the dielectric constant of most oils is only about 2-4. Further testing with aqueous films containing surfactant (with $\epsilon_r = 81$) did produce a clear signal as shown in figure 3.6. However, the capacitance was observed to *decrease* instead of increase in the presence of a film. This unusual observation is explained by two main factors, namely anomalous capacitance scaling due to fringe fields and effects of conductance and grounding.

**Anomalous scaling & grounding effects**

For the system sketched in figure 3.5 it is typically possible to achieve $d \sim R/4$ or slightly better. However, (3.19) is valid for far smaller gap widths, and in fact extensive simulations have shown that capacitance does not scale as $1/d$ when $d/R$ becomes too large. For example, Nishiyama & Nakamura (1993) used simulations to find

$$C_d = \frac{\epsilon \pi R^2}{d} \left[ 1 + 1.298 \left( \frac{d}{R} \right)^{0.867} \right] \quad \text{for} \quad 0.01 < \frac{d}{R} < 1, \tag{3.23}$$

which clearly shows that fringe fields associated with the edges of the capacitor plates increase the overall capacitance. What is perhaps surprising is that (3.19) underestimates actual capacity by about 10% when $d/R = 0.05$. Over any limited range of $d/R$, (3.23) can be represented as $C_d = f(\epsilon, R)\, d^{-\alpha}$ where $\alpha < 1$. As a result, when a capacitor gap of size $d$ and capacitance $C_d$ is split into two smaller gaps each of size $d/2$ by insertion of e.g. a thin metallic film, the total capacitance $C_{tot}$ is surprisingly reduced (i.e. $C_{tot} < C_d$). The total capacitance is now set by two capacitors in series (call these $C_{d/2}$), and the total capacitance becomes

$$\begin{aligned} C_{tot} &= \left( \frac{2}{C_{d/2}} \right)^{-1} \quad \text{and} \quad C_{d/2} \sim \frac{1}{(d/2)^{\alpha}} \quad \text{such that} \\ C_{tot} &\sim \frac{2^{\alpha-1}}{d^{\alpha}} < \frac{1}{d^{\alpha}} \quad \text{if } \alpha < 1. \end{aligned} \tag{3.24}$$

To first order, the aqueous film is a very thin conducting plate, and hence the observed decrease in capacitance could have been anticipated. However, the actual capacitance is smaller still than what could be expected from (3.23), and this is most likely due to the conductive nature of the aqueous film.

To get a better understanding of the effect of placing a conducting sheet of liquid

(or any other material) between the plates of a disk capacitor, simulations were performed using Maxwell2D (freeware). These simulations showed excellent agreement with (3.23), and also indicated that the conductance of any ungrounded sheet of material placed between the two electrodes should not have any effect on the observed capacitance. However, when the sheet of material was set to ground, e.g. as would be the case if the aqueous films were held in a metallic bath connected to the rest of the setup, the calculated capacitance was essentially nil.

The profound effect of grounding has to do in part with the way in which capacitance is measured in our setup (and calculated in Maxwell2D). The device as sketched in figure 3.5 has one active electrode with an applied AC voltage at 32 kHz, while the other electrode is passive. Capacitance is measured by registering the induced current from the passive electrode; but if there is a grounded sheet of material placed between the electrodes, the passive electrode will only ever see ground, and hence no current is induced. None of this should matter however, if the film is ungrounded.

In our experiments, the film was electrically isolated from ground, but connected to a relatively large conductive body of liquid ($\sim$ 30 ml) as well as to the steel frame holding the film. The results shown in figure 3.6 suggest that despite our efforts to electrically insulate the film, it acts as a grounded conductor. This raises an interesting question: how large does a conductive body need to be to act as ground locally? Exploration of this capacitance method as a way to measure film thickness indicates that with very careful design, both mechanical and electrical, it may be possible to measure soap film thicknesses. However, it is certainly not as simple as the following and final method we discuss here, namely absorbance.

### 3.2.3 Absorbance

Film thickness can be measured directly by absorbance, which follows the Beer-Lambert law

$$\frac{I}{I_0} = 10^{-\epsilon_\lambda c \ell}, \tag{3.25}$$

where $I/I_0$ is the ratio of absorbed to initial light intensity, $\epsilon_\lambda$ is the wavelength-dependent absorption coefficient (in units of $\mathrm{M^{-1}cm^{-1}}$), $c$ is the concentration of dye (or other absorbing species), and $\ell$ is the pathlength of the light through the absorbing medium. Adding dye to the solution potentially alters the surface tension, as well as the rheological properties of the solution. Such complications can, in principle, be avoided by use of infra-red light (IR), which is absorbed strongly by aqueous films. In that case, $\epsilon_\lambda$ is simply in units of $\mathrm{cm^{-1}}$. Some preliminary attempts were made to use IR, but alignment issues of the optical system (complicated by the invisible IR light source) led us to opt for a dye instead. For the experiments described hereafter, we used a 1 W, AlInGaP-based red LED light source (emission peak and half-widths at 645±10 nm) and a blue dye (erioglaucine disodium salt CAS 3844-45-4) which absorbs strongest in the red part of the visible spectrum, namely at 630±24 nm (Geethakrishnan & Palanisamy 2006). Use of a bandpass filter of 633±10 nm in front of the photo-detector in conjunction with the relatively strong LED light source ensured a high signal-to-noise ratio, even with some background lighting. Care was taken to minimize ambient air currents around the LED which affect the temperature and thus the intensity of the light source.

Although $\epsilon_\lambda$ is independent of dye concentration, at high concentrations of dye, the *effective* absorption coefficient can be smaller than one would expect. This phe-

nomenon can have multiple origins including (i) electrostatic interactions between dye molecules in solution (affecting their absorption spectra), (ii) polychromatic radiation, and (iii) stray light. According to Skoog & Leary (1992) electrostatic interactions typically play no role as long as $c < 0.01$ M. Our solutions were prepared with 1 mM dye, and we did not observe any influence from stray light. Our setup, however, does have a polychromatic light source, and it effectively 'samples' the part of the absorption curve of the dye that lies between $\lambda = 633 - 643$ nm, given the light source and filter characteristics. To illustrate the effect of polychromatic radiation, suppose that we had just two wavelengths of light in our source, e.g. one at 633 nm and the other at 643 nm. In that case, the observed intensity would be

$$\begin{aligned} I &= I_{0,633} 10^{-\epsilon_{633}\, c\, \ell} + I_{0,645} 10^{-\epsilon_{645}\, c\, \ell} \\ &= (I_{0,633} + I_{0,645}) 10^{-\epsilon_{\text{eff}}\, c\, \ell}. \end{aligned} \tag{3.26}$$

Figure 3.7 illustrates shows that $\epsilon_{\text{eff}}$ is always a decreasing function of $c$.

Careful calibration experiments with a wide range of dye concentrations and well-defined path lengths $\ell$ showed that $\epsilon_\lambda$ actually decreases with $c$, as shown in figure 3.8.

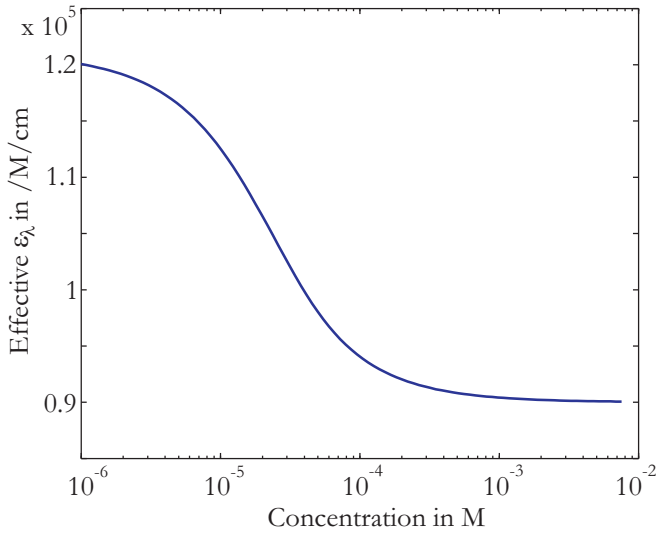


Figure 3.7: Effective absorption coefficient $\epsilon_{\text{eff}}$ as calculated in (3.26). For the purposes of this illustration $I_{0,645} = 2I_{0,633}$ and $\epsilon_{633} = 2\epsilon_{645} = 183000$ $\text{M}^{-1}\text{cm}^{-1}$, with a path length of 1 cm.

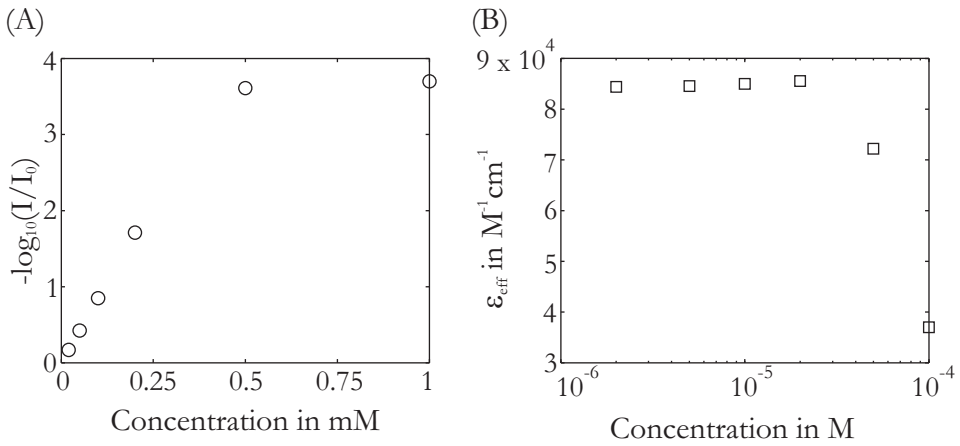


Figure 3.8: Calibration of absorbance setup. (A) absorption vs. dye concentration in water and (B) $\epsilon_{\text{eff}}$ vs. dye concentration. The dye is erioglaucine disodium salt, a common blue food dye.

## 3.3 Results

As discussed in §2.1.1, some data exists in the soap film literature involving solutions of PEO. These solutions always contained some small amount of polymer, and a large amount of SDS. As most of the data in figure 2.3 shows, low molecular weights and low concentrations of polymer generally result in reasonable agreement between measured film thicknesses and Frankel's law. Deviations come into play when the molecular weight is increased, and much thinner films are made at similar $C_a$ numbers. We sought to expand the available data for films made with PEO, with and without SDS added.

In §3.3.4 we discuss precisely those results, and in §3.3.5 we discuss a surprising feature in the dynamics of these films, namely film swelling. But first, we discuss how to pick or define 'initial thickness' for a film that is recorded during all stages of its formation, including the stage where it is so close to the bath that it is essentially part of a meniscus, and not yet a film.

### 3.3.1 Defining 'initial' thickness and $t = 0$

A film of liquid that is withdrawn from a bath could, in principal, be drawn out forever in a steady process. It is for this idealized case that theory has been developed to find expected film thicknesses; and the theory often refers not to *initial* thickness, but to *constant* film thickness, which corresponds to the limit of film thickness far away from the bath. In a laboratory setting, however, even the thinnest films will be subject to capillary-driven drainage towards the Plateau borders around the wire frame, marginal regeneration, gravity drainage and finite withdrawal lengths that

can be achieved in the setup. As a result, there can be some ambiguity about which recorded film thickness counts as the 'initial' one.

Lionti-Addad & di Meglio (1992) and Berg *et al.* (2005) explain the most common experimental approach to this ambiguity. They, as well as most of the soap film literature before them, record the thinning of a soap film over time (measured by interference), and then extrapolate backwards in time. The time $t = 0$ is commonly taken to be the first moment that the detector records a non-zero signal. At that point, the film is flat enough to have back reflections reach the detector and a film is 'born'. In the case of transmittance methods such as Michelson interferometry, absorbance, and even capacitance, there is almost always a non-zero signal that does not necessarily correspond to the presence of a flat film, and some other consistent moment in the evolution of a film must be chosen as $t = 0$.

Consider the evolution of the film thickness at a given distance $\ell$ below the withdrawal wire, as sketched in figure 3.9. In order to see a film at all, we must view the film roughly a distance $\ell \approx \ell_c$ (the capillary length) below the wire to avoid large effects due to the Plateau border at the wire. Take $\ell_b$ to be the distance that the bath needs to travel in order for the bottom of the beam to be visible above the rim of the bath, as sketched in figure 3.9. Withdrawing a film at some speed $U$ starting at $t = 0$ means that we may expect a film to be seen at $\ell_b$ at time $t_1 = \ell_b/U$. However, at $t = t_1$, the film thickness is still somewhat undefined since we are essentially observing a curved static meniscus that connects the bath to the film. Therefore, a proper film cannot be observed until the wire has been withdrawn a further distance $\ell_m$ of order $\ell_c$, which is the typical scale of a static meniscus. Hence, '$t = 0$' from the perspective

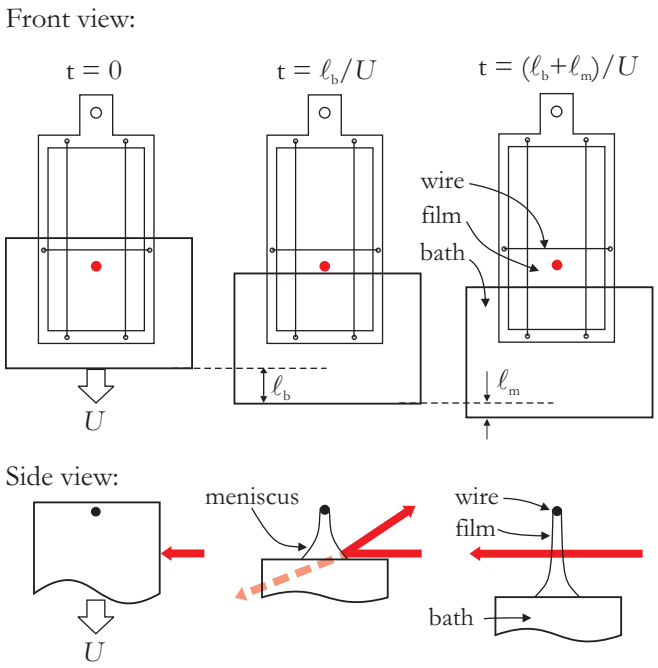


Figure 3.9: Determining $t = 0$ in the reference frame of the film. The beam of light is fully visible after the bath has dropped a distance $\ell_b$ which corresponds to the sum of the beam diameter and the distance between the wire and the beam (assuming that the liquid is initially flush with the top of the bath). The bath needs to drop a further distance $\ell_m$ so that the light beam hits above the meniscus of the liquid, and the film is sufficiently flat so a thickness can be recorded. In our experiments, the beam has a diameter of $\sim$3 mm, and it is placed $\sim$5 mm below the wire, so that $\ell_b = 8$ mm; and we choose $\ell_m = \sqrt{2}\,\ell_c$.

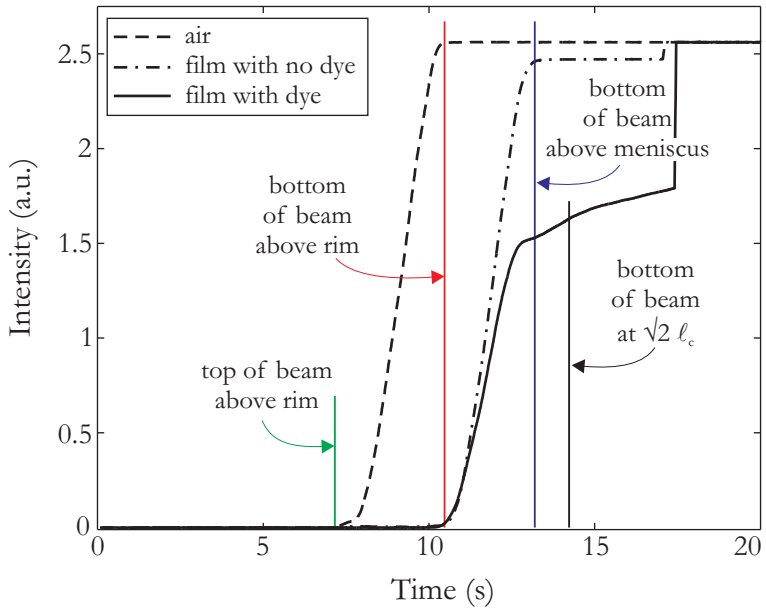


Figure 3.10: Calibration in air and without dye. The film thickness is sampled when the bottom of the light beam is $\sqrt{2}\ell_c$ above the bath, as indicated by the black vertical line. The solutions used for the dash-dotted and solid lines contained 1% PEO of $M_w$ $10^6$, where 1 mM dye was added to the solution used for the solid line.

of a newly formed film at position $\ell_b$ corresponds to a time $t' = (\ell_b + \ell_m)/U$ after withdrawal starts.

In the laboratory, this question is further complicated by the finite size of whatever probe is used to measure film thickness, be it a laser beam, a capacitor plate, etc. In all experiments that follow, we choose $t = 0$ to correspond to $t' = (\ell_b + \sqrt{2}\,\ell_c)/U$ since a static meniscus with zero contact angle will reach a maximum height at a distance of $\sqrt{2}\,\ell_c$ above the bath. By using this definition systematically, we may confidently compare trends of 'initial' film thickness and evolution as the withdrawal speed or liquid properties are varied.

A calibration experiment aimed at clarifying the distorting role of the meniscus is shown in figure 3.10. From the observation of light intensity in the absence of a

film, we know at what times (i.e bath positions) the light should be fully visible. In a subsequent experiment with a film (without dye), the meniscus strongly distorts the observed light intensity as sketched in figure 3.9, and we observe that this meniscus extends roughly $\ell_c$ above the bath as expected. The experiment without dye also shows that some light is reflected off the film, representing a loss of the order of 3.5% of the light, which is accounted for in the analysis of subsequent experiments. Finally, an experiment is shown for a film pulled at the same speed and with the same solution, with added dye.

### 3.3.2 Measured solution properties

In our experiments, we used both a "thick" and a "thin" wire, to probe differences induced by wire thickness. The thick wire had a diameter of 200 $\mu$m and was made of nylon, while the thin wire had a diameter of 25 $\mu$m and was made of nickel chromium alloy. With the nylon wire it was not possible to make films with simple SDS and glycerol solutions, presumably due to unfavorable wetting characteristics. With the NiCr wire, there were no wetting issues.

We initially restricted the experiments to be conducted with two molecular weights of PEO, namely $10^5$ and $10^6$ g/mol (also referred to as 100k and 1M in the figures). For each molecular weight, we made aqueous solutions with 0.5, 1 and 2% by weight. We then added 1 mM blue dye to each solution, and split the obtained stock solution into two parts. To one half of the stock, we added a further 2% by weight SDS.

Table 3.1 summarizes the measured properties of the solutions used in our experiments. Surface tensions were measured using the pendant drop method, viscosities

| $M_w$ g/mol | $c_{PEO}$ % | $c_{SDS}$ % | $\epsilon_{eff}$ $M^{-1}cm^{-1}$ | $\gamma$ mN/m | $\mu$ mPa.s | $\rho$ $kg/m^3$ | pH |
|---|---|---|---|---|---|---|---|
| $10^5$ | 0.5 | 0 | 73200 | 61.8 | 1.2 | 964 | 7.6 |
| | 0.5 | 2 | 77500 | 35.9 | 1.6 | 964 | 7.4 |
| | 1 | 0 | 71300 | 57.0 | 2.2 | | 7.8 |
| | 1 | 2 | 68400 | 37.0 | 2.5 | | 7.9 |
| | 2 | 0 | 70600 | 57.3 | 4.1 | | 8.1 |
| | 2 | 2 | 69800 | 38.4 | 4.2 | | 8.2 |
| $10^6$ | 0.5 | 0 | 72200 | 60.1 | 8 | 965 | 8.5 |
| | 0.5 | 2 | 75600 | 36.7 | 31 | 966 | 7.4 |
| | 1 | 0 | 71300 | 60.0 | 38 | 965 | 7.9 |
| | 1 | 2 | 74500 | 37.7 | 60 | 983 | 8.1 |
| | 2 | 0 | 76800 | 60.5 | 311 | | 8.2 |
| | 2 | 2 | 74900 | 39.0 | 198 | | 8.8 |

Table 3.1: Solutions used in film withdrawal experiments. All solutions contained 1 mM dye (erioglaucine disodium salt, a regular blue food dye). Concentrations are reported by % weight.

were measured using a rheometer with a double-walled Couette geometry. The pH was measured with a PHM220 pH meter which has disputable reliability, but in any case demonstrated that none of the solutions were strongly acidic which would degrade the polymer over time. Finally, the absorption coefficients $\epsilon_{eff}$ were measured using a cuvette with precisely defined path length of $\ell = 200$ $\mu$m. It is possible that there may be some difference in effective absorption coefficients between fluid contained in a glass cuvette versus fluid in a freely suspended film; since molecular scale arrangement of the absorbing species may be affected by the nature of the interfaces. We did not design a separate experiment to test this, since any possible difference is not expected to be large enough to matter for the interpretation of the film thickness data.

### 3.3.3 Typical results

Figure 3.11 shows a typical result for film withdrawal from a bath. In the top panel, light intensity is recorded over time, which is then translated into a film thickness versus time plot in the bottom panel. As discussed in §3.3.1 and shown in figure 3.10, we record the film thickness at $y = \sqrt{2}\ell_c$ as the 'initial' film thickness. A number of interesting observations can be made just from an initial inspection of figure 3.11. First of all note that this film was made without added surfactant, and that it is quite thick compared to films normally made *with* surfactant. Before the bath stops moving, the film thins quite rapidly, as evidenced by the steep slope in figure 3.11(B) between the blue and red dashed lines. The overall drainage process that follows after the bath has stopped is clearly much slower, and this is a trend that is reproduced in all films. The difference in thinning rate presumably marks the difference between *stretching* a film, and *draining* a film by capillarity and/or gravity.

A further feature of figure 3.11(B) is the swelling that is observed for the first 15 seconds or so following the moment that the bath stops moving. In section §3.3.5 we investigate this intriguing phenomenon in more detail. Finally, the film breaks when the average thickness at the point of measurement is still quite thick, around 50 $\mu$m. This large thickness at breakup, as well as the relatively short lifespan of many of the films we generated was quite typical. Indeed, this was one of the reasons why we chose to use absorption rather than interferometry to measure film thicknesses, since knowledge of the thickness at rupture is known in the latter method. The relatively short lifespans of films produced in our lab could be related to the size of the films which are quite a bit larger than previously studied films (Adelizzi & Troian 2004;

Berg *et al.* 2005); and/or to the reduction of vibrations and air currents around the film. To reduce vibrations, the entire experiment was placed on an actively damped optical table. Air currents were reduced as much as possible by placing a large plexiglass box over the entire experiment; and evaporation was minimized by placing containers with luke-warm water and large surface areas in the enclosure. Despite these precautions, films rarely survived beyond a minute.

One question one might ask of the data is how important it is to pick the right moment in the formation of the film to measure the initial thickness. In figure 3.12 we probed another fairly typical experiment to see what difference in trends one might observe if the film is not sampled at $y = \sqrt{2}\ell_c$, but rather 0.5 mm above or below that point (i.e. placing '$t = 0$' slightly earlier or later in the film's life). Figure 3.12 shows that at low withdrawal speeds, the film thickness is fairly independent of the exact time at which it is recorded. At higher withdrawal speeds the scatter in actual data points is still larger than the amount by which they are shifted by measuring slightly earlier or slightly later. In what is to follow, initial film thicknesses were always recorded for $y = \sqrt{2}\ell_c$.

### 3.3.4 Initial thickness vs. $C_a$

Figure 3.13 shows our entire data set, organized by presence of SDS (columns), concentration of PEO (rows), wire thicknesses (color of the symbols) and molecular weights of the PEO used (shape of the symbols).

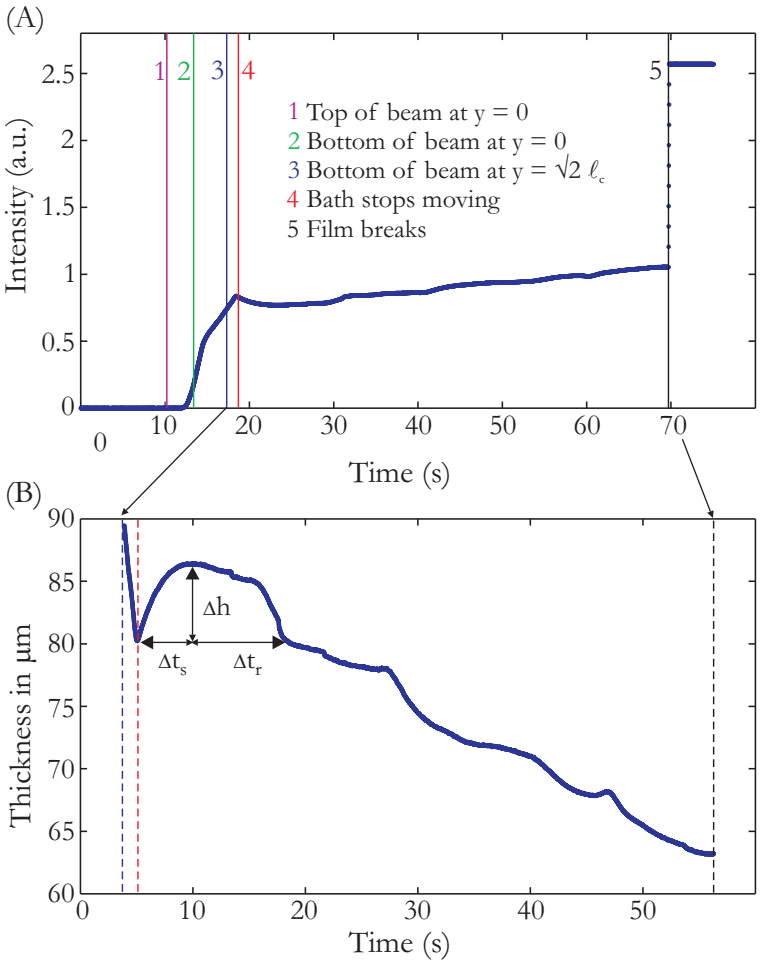


Figure 3.11: (A) Typical intensity measurement for determination of film thickness by absorbance, with various times of interest indicated, and (B) translation of the intensity to actual film thickness. This particular film was made with a solution of 2% PEO of $M_w = 10^6$ with 1 mM blue dye (no SDS), and pulled at a speed of 0.90 mm/s, using the thick wire. Also indicated: $\Delta h$, $\Delta t_s$ and $\Delta t_r$ which characterize the amount and duration of film swelling which often occured after the bath stopped moving.

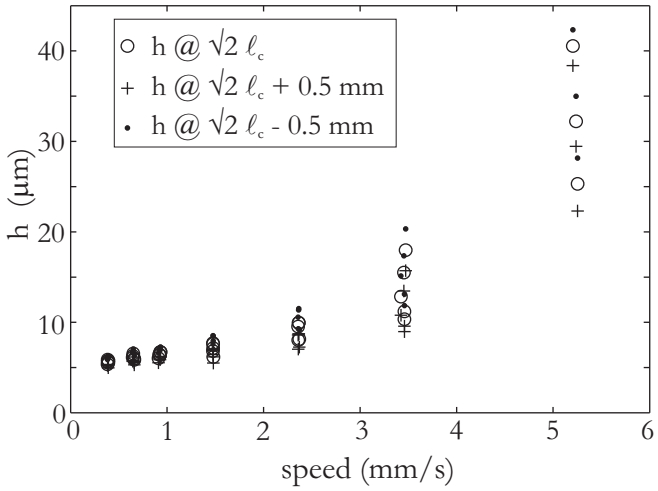


Figure 3.12: Effect of probing the film thickness slightly (0.5 mm) above or below the height of a static meniscus ($\sqrt{2}\ell_c$). For clarity, only three data points are shown at the fastest withdrawal speed. For this particular data, the solution contained 0.5% PEO of $M_w$ $10^6$ and 1 mM dye, without SDS.

**Influence of wire thickness**

Since all literature data to date was collected for films drawn in frames of very thin wires, we sought to see the influence of wire thickness. Figures 3.13(A)-(F) show that in most cases, the wire thickness plays no significant role in setting the initial film thickness. Interestingly, it was possible to make films with the 0.5% PEO solutions of low molecular weight, with and without SDS, using the thin wire. These solutions did not make films using the thick wire, which may be due to different wetting properties of the wires. Another feature of the data collected with the thin wires is that the scatter of initial thicknesses is smaller. It is often speculated that using thicker wires would induce stronger marginal regeneration and capillary drainage into the relatively large Plateau borders (Berg *et al.* 2005); and this scatter in the data may be some manifestation of those effects.

A final important feature of the experiments with thin wires, is that the film

thickness often *exceeded* the wire thickness. This is especially apparent for solutions without SDS involving 1% and 2% PEO of high molecular weight, for which the thickness sometimes exceeded twice the thickness of the wire. Clearly some experimental uncertainties for example in the determination of $\epsilon$ or $c_{\mathrm{dye}}$ could help explain a difference of order 10%, but a factor of 2 must be taken to indicate a physically significant result. The thick films are an indication of the non-Newtonian rheology of these solutions, and are reminiscent of the die-swell phenomenon.

**Influence of PEO and SDS concentrations**

Looking initially at panels (A), (C) and (E) in figure 3.13, we can discern the effect of PEO concentration on initial thickness in the absence of SDS. As the concentration is increased, the viscosity increases and thus all $C_a$ numbers will be larger for the same withdrawal speeds. However, at a given $C_a$ number, films tend to be slightly thicker with increasing concentration but it is not a strong effect. When SDS is added, precisely the opposite is observed, and film thicknesses decrease with increased polymer concentration. We note that there is no strong effect of molecular weight, other than to shift all the data points to lower $C_a$ values corresponding to the lower viscosities of those solutions.

When SDS is added, as in panels (B), (D) and (F) in figure 3.13, we note that film thicknesses are *thinner* than in the absence of SDS. For the lowest concentration of PEO, there is still a positive correlation between initial film thickness and capillary number. For 1% PEO the correlation disappears for the high $M_{\mathrm{w}}$ PEO, and for 2% films actually exhibit smaller initial thicknesses as the capillary number is increased,

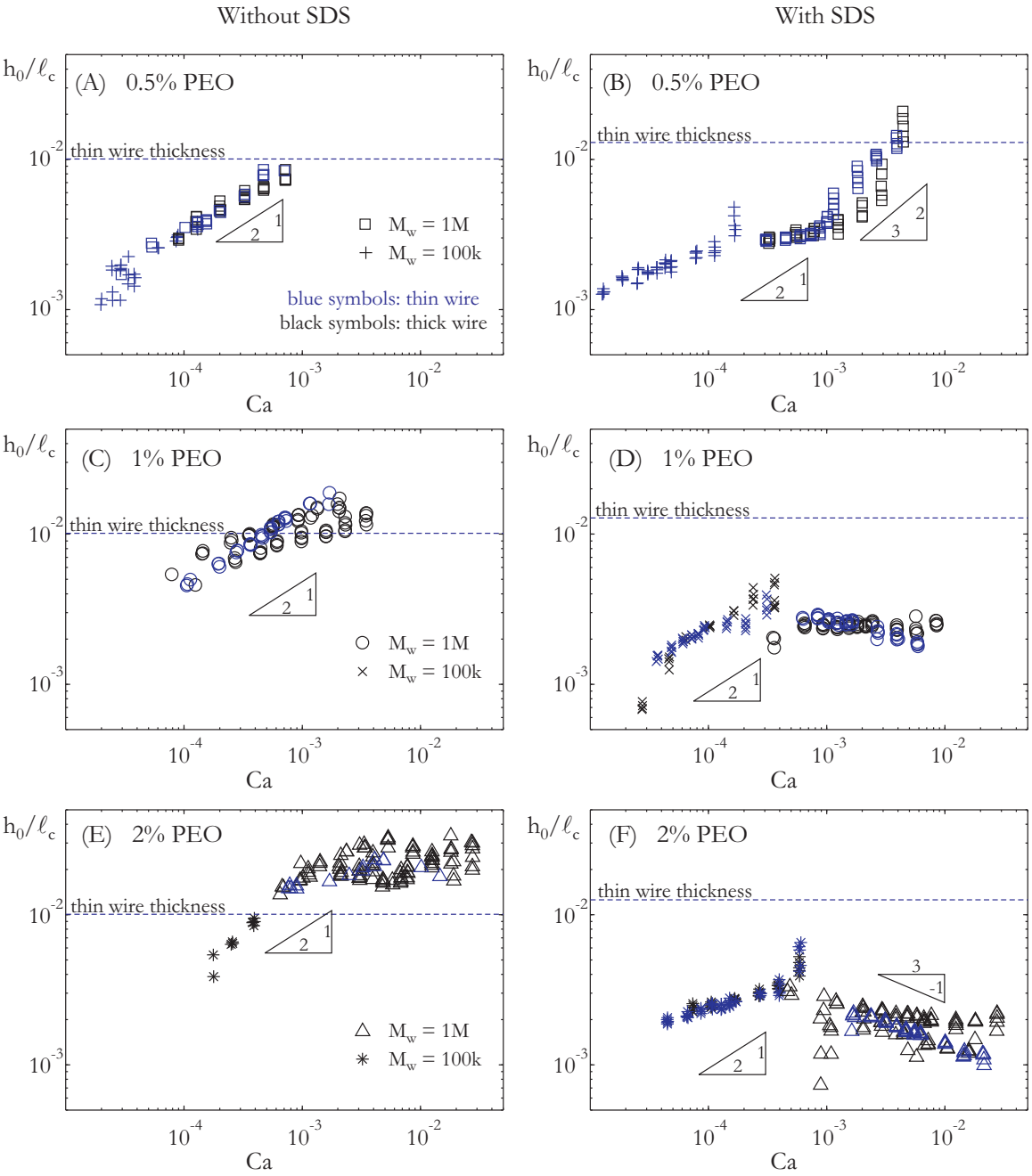


Figure 3.13: Left column of figures: solutions without SDS, right column of figures: same solutions, with SDS added. Molecular weights are distinguished by the symbols, while different wire thicknesses correspond to the color of the symbol. First row: 0.5% PEO, second row: 1% PEO, third row: 2% PEO. The various power-law slopes are shown as a guide to the eye. The thin wire thickness (25 $\mu$m) indication is approximate, as $\ell_c$ is different for each solution.

with an approximate power law dependence of $h/\ell_c \sim C_a^{-1/3}$. Experiments are ongoing with PEO concentrations of 0.25 and 0.75% to see if these will result in thicker or thinner films as a function of $C_a$. Bear in mind that when SDS is added to a solution of PEO, the chains tend to swell and the viscosity tends to increase. Hence, for a given concentration of PEO, and a given withdrawal speed, adding SDS will increase the capillary number. Since the polymer chains are already swollen, one might speculate that little further conformational change will occur as the polymer-SDS complexes are withdrawn from the bath. Additionally, the polymer-polymer interaction which could otherwise help to thicken a film could be decreased by the presence of SDS. However, it is at present unclear why a further increase in withdrawal speed would result in thinner films.

**Comparison with literature**

Comparing the data from our thin wire experiments with data from the literature as well as Frankel's law, we turn to figure 3.14. A striking feature of all of the data sets is that they overlap at similar capillary numbers, which gives us confidence in comparing results from our absorbance measurements to existing interferometric data. The thinning effect previously discussed in the context of figure 3.13 is seen more dramatically in figure 3.14.

In panel (A) we superpose existing data for soap films with PEO in the same molecular weights that we have used, i.e. 100k and 1M. Trends seem to be consistent; e.g. between our 0.5% PEO 1M data and that in the literature. In panel (B) we superpose all the data from figure 2.3 on our own. Note that in any case Frankel's

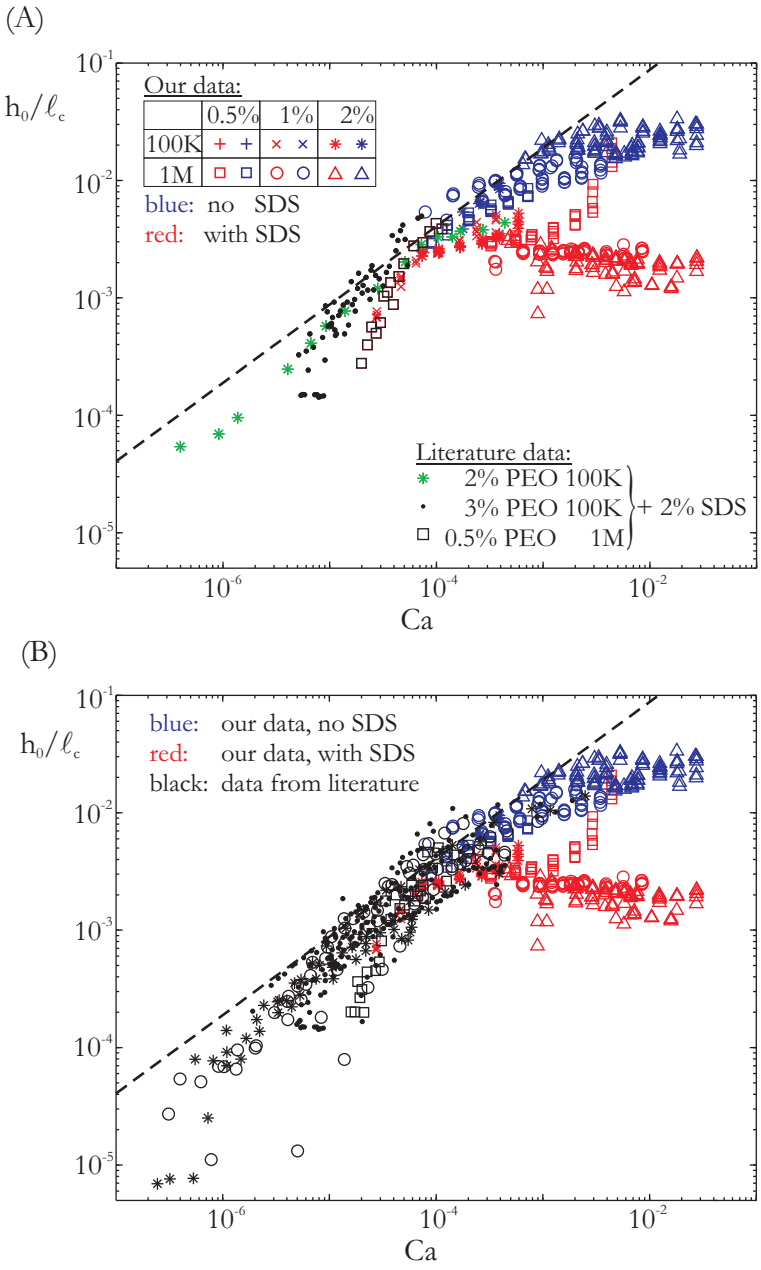


Figure 3.14: (A) Comparison of our thin wire data (red with SDS, blue without SDS, various concentrations and molecular weights) with data from literature that uses similar molecular weights. (B) Comparison of our data with all known data from literature for solutions with polymer/surfactant systems (see table 2.2 for more details on literature data).

law is inadequate to rationalize the results for these non-Newtonian fluids.

### 3.3.5 Film swelling

As shown in the typical result in figure 3.11, swelling of the film often occurs right after the bath stops moving. This swell is characterized by the total amount of swell $\Delta h$, the time it takes to reach that swell, $\Delta t_s$, and the time $\Delta t_r$ it takes to relax back down to the thickness that the film had at the moment the bath stopped. In figure 3.15 we show all of the experiments (all molecular weights, concentrations of PEO and SDS, all wire thicknesses) that displayed an unambiguous swell. There were many other withdrawn films that either showed no signs of swell, or displayed a very noisy thickness vs. time; too noisy to retrieve a reliable measure of $\Delta h$ and $\Delta t_s$. This 'noise' may be due to convective plumes in the film (which were visible by eye for some of the longer lived and thicker films), air currents, vibrations, or some other as yet unknown reason. For what is to follow, therefore, we restrict ourselves to unambiguous data sets with rich dynamics.

The left column of figures in figure 3.15 shows data collected for solutions without added SDS, while the right column features data collected for solutions with SDS. In each column, the first row shows the relationship between $\Delta h$ and $C_a$, where different colored symbols indicate different concentrations of PEO and the shape of the symbol indicates both the molecular weight and the wire thickness. It is immediately apparent that very large swells occur, up to 35 $\mu$m for solutions without SDS, and up to 8 $\mu$m when SDS is added. When taken as a percentage of the thickness the film had at the moment the bath stopped $h_{\text{stop}}$, figures 3.15(C) and (D) show that SDS does not

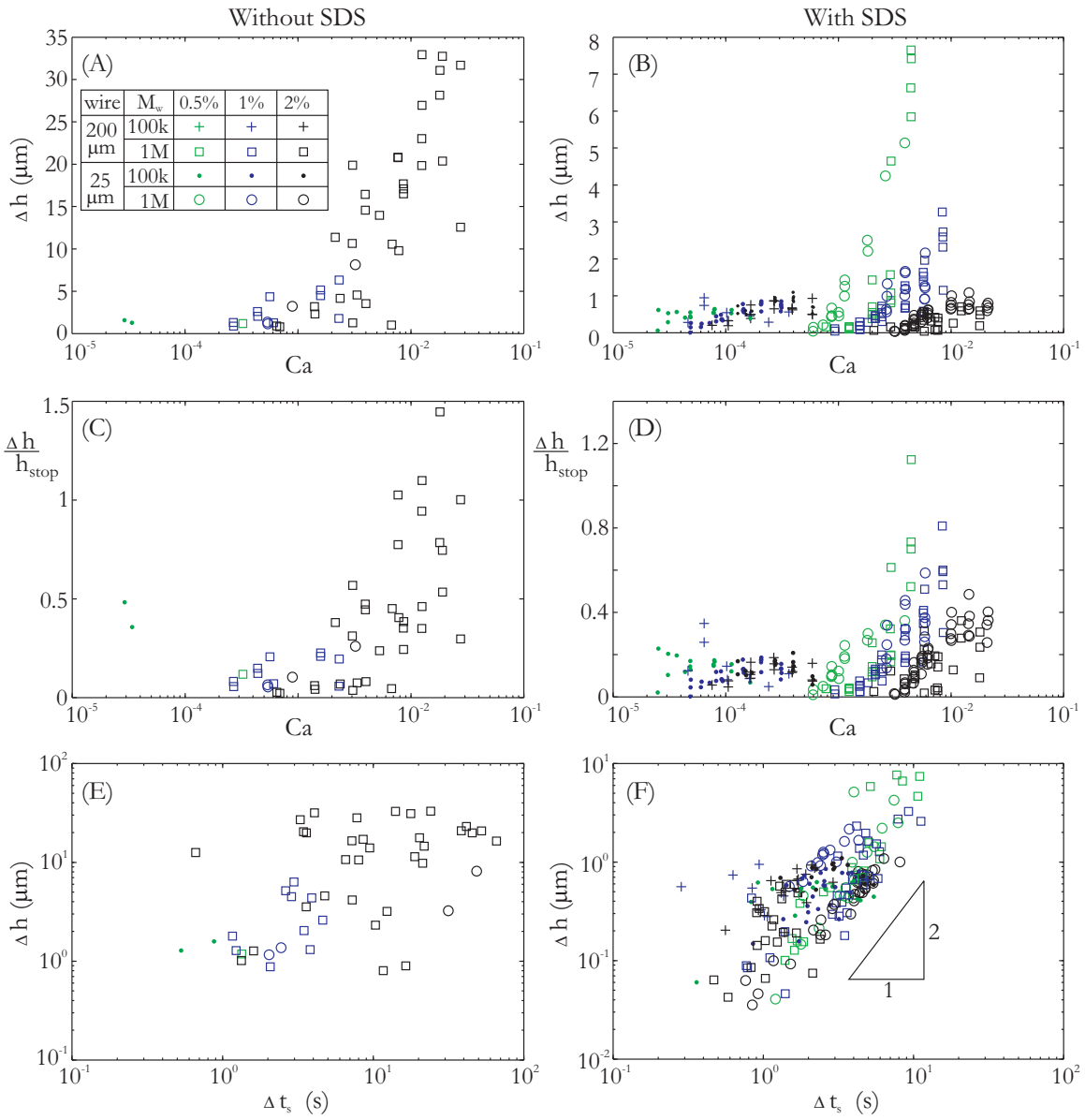


Figure 3.15: Left column of figures: solutions without SDS, right column of figures: same solutions, with SDS added. The legend in (A) is valid for all figures (A)-(F). First row: swell thickness as a function of $Ca$, second row: ratio of swell thickness to film thickness when bath stops moving $h_{\text{stop}}$, and third row: swell thickness as a function of time for the swell to reach maximum thickness.

have a large influence on the strength of the mechanism that leads to swell, but it does result in thinner films as also shown in figure 3.14. Addition of SDS leads to far more stable films that last long enough for the swelling to be observed, and hence there are far more data points in the right column than the left column of figure 3.15.

Figure 3.15 demonstrates that swelling is more pronounced, and more likely to occur at higher $C_a$ numbers and/or higher $M_{\mathrm{w}}$ PEO. However, at a given capillary number in the presence of SDS, increasing the concentration of PEO leads to a *decrease* in swell thickness. We plotted the same swelling data versus withdrawal speed instead of $C_a$, so as to probe the relative influence of changing $U$ instead of $\mu$ in $C_a$. Although that data is not shown here, we observed that for a given withdrawal speed, an increase in PEO concentration (and hence in $\mu$) led to a decrease in $\Delta h$. In the absence of SDS, there are fewer data points with more scatter amongst them, but they do show an opposite trend. That is, for a given withdrawal speed, an increase in PEO concentration leads to an *increase* in $\Delta h$, in the absence of SDS.

The time scale of swelling $\Delta t_s$ is plotted in the third row of figure 3.15, as a function of $\Delta h$. In the presence of SDS, a power-law like relationship appears of the form $\Delta h \sim \Delta t_s^2$, which may be a hint to the underlying mechanism that causes swell in the first place. Before turning to some potential explanations of swell, we note that the timescale for relaxation $\Delta t_r$ was typically very similar to $\Delta t_s$, although in some exceptional films relaxation took much longer than swell. Finally, we observe that wire thickness has no discernable effect on swell characteristics.

**Potential swell mechanisms**

The observation of swell leads to a natural question to ask, namely: where does the extra fluid come from? Two options present themselves, (i) either the volume of liquid in the film is conserved (or even decreases slowly with time), or (ii) the volume of liquid in the film initially increases when the bath stops moving. In the first case, the swelling observed at the point where we interrogate the film thickness must be due to redistribution of the fluid in the film, for example by some form of convective flow. In the second case, there must be some mechanism by which fluid is entrained into the film which was previously being stretched as the bath dropped.

Imagine first a mechanism by which the film would swell without an initial increase in film thickness. During bath motion, the film thins through stretching and drainage. It is potentially replenished to some degree by, for example, a reservoir of fluid in the Plateau border around the top wire suspending the film. The flux of fluid by stretching and drainage away from the point of film thickness interrogation initially exceeds any replenishing flux from elsewhere, and the film thins. When the stretching is stopped, the film thickness would increase if the flux of fluid from the top Plateau border exceeds the flux by drainage. This argument relies on the existence of some flux from the border to the middle of the film. On the one hand such an argument is supported by the observation that larger withdrawal speeds $U$ result in thicker swells. For larger $U$, drainage of fluid from the top border has had less time to proceed by the time the bath stops moving, and so there is more fluid to swell the film. Simultaneously, larger $U$ also means faster stretching, and so the difference in fluxes before and after the bath stops would be larger, leading to larger swell. On the other hand, it is unclear why

any body of liquid would exist in the first place, and indeed the results indicate that swelling is independent of wire thickness. We therefore turn to the second potential mechanism, which involves an increase in film volume just after the bath stops.

Since the film contains polymers, and these polymers are stretched to some degree in the process of film formation, they will necessarily start to relax when the bath stops moving. As the polymer chains relax, they 'suck' fluid into the film from regions where the fluid has experienced less stress, for example close to the wires and in the bath. As a result, the film swells until drainage by gravity and capillarity take over. This mechanism is analogous to die swell, or the expansion of a polymeric solution as it exits a pipe. Given the experimental data on relaxation timescales from Lance-Gomez & Ward (1986), swelling for a period of 1-10 seconds is not unreasonable. If the non-Newtonian nature of the solution is indeed the reason behind the swelling, then it would make sense for the effect to be larger as the fluid becomes more viscoelastic, i.e. as the concentration and $M_{\mathrm{w}}$ of the PEO in solution increase. In the absence of SDS, the data support this notion, even showing no swell at all for the lowest concentrations of PEO used. However, in the presence of SDS the trend is reversed, and lower concentrations of PEO surprisingly result in larger swells at similar $C_a$ or $U$. This is where the complexity of the rheology of a mixture of PEO, SDS, and dye, complicate matters. The same data from Lance-Gomez & Ward (1986) demonstrated that relaxation time scales can be either larger or smaller with the addition of surfactant, and in their experiments this was shown to depend on the polydispersity of the polymer used. Further modeling needs to be done to determine what might cause the swelling, and further experiments are in order to precisely

determine the role of the viscoelastic nature of PEO solutions in this mechanism.

### 3.3.6 Concluding remarks

To summarize our experiments, we briefly list the main points learned from studying films withdrawn from a bath. The main distinguishing feature of our experiments compared to the existing literature, is that we were able to measure absolute thicknesses using absorbance, and we were able to measure the film thickness of 'soapless' soap films, containing just polymer and the dye necessary for absorption. Listing the main points, we found:

- In the range of $C_a$ where our experiments overlap with experiments in the literature, our data matches well with existing data.
- We have extended the range of $C_a$ where films have been made.
- By using light absorption and a dye, we were able to measure the absolute thickness of a variety of films.
- Our experiments allow us to conclude that:
  - adding SDS to polymer solutions tends to make *thinner* films,
  - films can be made which are thicker than the wire that suspends them,
  - wire thickness does not have a large influence on the film thickness,
  - films can be made *in the absence of SDS*, although we note that PEO is somewhat surface active itself.

- We observe a novel feature of films made with solutions of PEO, namely 'film swell'.
- Films can swell to up to 150% of their initial thickness, and we found that
  - films with SDS are more stable, and swell more readily than those which lack SDS, but
  - films without SDS swell much more in absolute terms; we recorded swells up to 35 $\mu$m.
  - for a given $C_a$ or withdrawal speed, in the presence of SDS, more swelling occurs for lower concentrations of PEO.

As indicated throughout the discussion of the results, next steps to carry this research forward are required both in terms of more experiments, and in terms of some modeling efforts. Experiments with a larger range of PEO concentrations and perhaps also SDS concentrations would allow construction of a phase diagram of $c_{\mathrm{PEO}}$ versus $c_{\mathrm{SDS}}$ indicating under which circumstances films can be made at all, and at which concentrations of PEO / SDS the resulting film will be thinner with increasing $C_a$ rather than thicker.

It is also worth noting that one of the reasons we used very high concentrations of SDS, was to avoid Marangoni stresses. As pointed out in §2.2, the strength of surface stresses will set the flow type in a film. Whether the flow is of a shear-like nature or extensional nature is not known at this point, and this could have a profound impact on the way one should think about the role of the polymer: whether its extensional viscosity, or shear thinning quality dominates the dynamics.

# Chapter 4

# How bumps on whale flippers delay stall: an aerodynamic model

The majority of this chapter is reprinted with permission from van Nierop *et al.* (2008*a*), which was co-authored with Silas Alben and Michael Brenner (copyright (2008) by the American Physical Society). The work on humpback whale flippers started as a so-called ES299r, or reading & research course. During the initial reading for that course, we learned a lot about how wings generate lift, and how this lift can be modified by altering wing characteristics. Fortunately, we got carried away by the topic, and found a model to describe the aerodynamics of humpback whale flippers. We thank Frank Fish for many excellent references and interesting discussions, as well as the greater 'humpback aerodynamics' community in New England for sharing ideas and wind tunnel results.

## 4.1 Introduction

Humpback whales (*Megaptera novaeangliae*, see fig. 4.1(a)) are particularly agile whales, capable of performing rolls and loops under water (Hain *et al.* 1982; Woodward *et al.* 2006). Woodward *et al.* (2006) attribute their agility to the bumpy tubercles on the leading edge of their pectoral flippers. Inspired by this uncommon leading edge design, Miklosovic *et al.* (2004) tested model flippers in wind tunnels, and found that the bumps lead to an increase in stall angle of up to 40% without compromising lift or drag. Later experiments by Johari *et al.* (2007) and Stein & Murray (2005) showed that bumps make the onset of stall much more gradual. Model aircraft builders have already adjusted wing designs to take advantage of these desirable control properties (Goudeseune 2006), but the mechanism remains unclear. Here, we demonstrate that a model based on standard aerodynamic theory explains most of the experimentally observed phenomena.

Leading edge bumps on flippers or wings have been compared to vortex generators (Miklosovic *et al.* 2004), which are small objects placed on a wing that inject momentum into the boundary layer (i.e. making it turbulent) to delay flow separation (Thwaites 1960). However, it is implausible that bumps on the flippers act as vortex generators since both the wavelength and amplitude of the bumps are much larger than the boundary layer thickness. Here we propose a different mechanism: we demonstrate that the bumps alter the pressure distribution on the wing such that separation of the boundary layer is delayed behind bumps. This ultimately leads to a *gradual* onset of stall and larger stall angle.

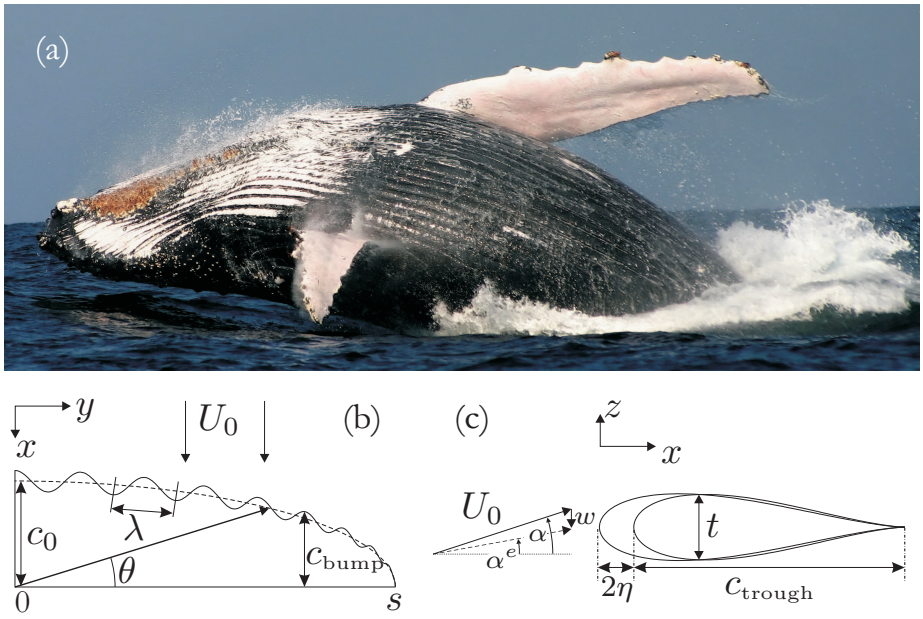


Figure 4.1: (a) Humpback whale lunging for food; note the bumps on the leading edge of the pectoral fins. Photograph by Brett Atkins, obtained from www.dreamstime.com. Sketch of the flipper geometry: (b) the planform from above; (c) cross section of a bump and trough of amplitude $\eta$.

## 4.2 Modeling

To understand the role of the bumpy tubercles, we consider a simple model of a smooth wing, and then show how the aerodynamic properties of the wing are modified when bumps are added. Our model considers a wing whose chord varies on a length scale large compared with its thickness. Working in this limit allows us to analytically capture the unseparated flow around the wing up to the attack angles where separation occurs. We employ an empirical separation criterion derived for flow around flat plates, which is approximately correct in the thin plate limit. Since in this long wavelength limit there is no spanwise flow, flow separation at each wing section is assumed to depend on the upstream flow conditions rather than the flow over neighboring sections.

### 4.2.1 Smooth wing

For the smooth wing we use a classical elliptic wing (see e.g. (Batchelor 1992)), where each cross section of the wing is described by a Joukowski profile, see fig. 4.1(c), (Acheson 1990). For a typical humpback whale lunging speed of $U_0 = 2.6$ m/s and ocean viscosity of $\nu = 1.35 \cdot 10^{-6}$ m$^2$/s, the flow around the wing has typical Reynolds number $R_e > 5 \cdot 10^5$ (Miklosovic *et al.* 2004), and is composed of two different regimes. Near the wing, there is a (turbulent) boundary layer while outside of the boundary layer the flow is well-approximated by potential flow, where the circulation $\Gamma$ is determined by the Kutta condition (Acheson 1990)

$$\Gamma = -\pi U_0 \left( c + \frac{4}{3\sqrt{3}} t \right) \alpha^e + O\left( (\alpha^e)^3, t^3 \right) \tag{4.1}$$

Here $U_0$ is the uniform flow velocity, $c$ is the chord length, $t$ is the thickness, and $\alpha^e$ is the effective angle of attack (see fig. 4.1(c)). Both the chord length and the wing thickness taper off from the root of the wing to the tip ($y = 0$ and $y = s$ or $\theta = \pi/2$ and $\theta = 0$ respectively, see fig. 4.1(b)) such that their ratio $t/c$ is constant. For an elliptic wing, $c(\theta) = c_0 \sin\theta$ and $t(\theta) = t_0 \sin\theta$.

Equation (4.1) implies that the variation of the chord and thickness along the wing causes a variation in the circulation $\Gamma$. Such spanwise changes in $\Gamma$ generate a sheet of streamwise vortices behind the wing, which causes a downwash $w$ – an oncoming downward flow – at each wing cross section (see fig. 4.1(c)). This downwash causes the effective angle of attack to *vary* along the wing,

$$\alpha^e = \alpha - \frac{w}{U_0}. \tag{4.2}$$

The magnitude of the downwash can be calculated using lifting-line theory, which allows us to represent the wing as a single vortex line of varying strength along the span (Batchelor 1992) viz.

$$w = \frac{1}{4\pi}\int_s^{-s} \frac{\mathrm{d}\Gamma/\mathrm{d}y'}{y' - y}\mathrm{d}y' \ . \tag{4.3}$$

By accounting for the coupling of wing sections through the downwash generated on the entire wing as in (4.3), the flow is three-dimensional. However the absence of spanwise flow in the long wavelength limit makes the flow at each wing section approximately two dimensional.

Writing equations (4.1)-(4.3) in terms of $\theta$ and expanding $\alpha^e(\theta)$ and $\Gamma(\theta)$ as two Chebyshev series,the integral equation reduces to a matrix equation which can be solved numerically. We then use $\Gamma$ to compute the lift $L$ by summing the circulation

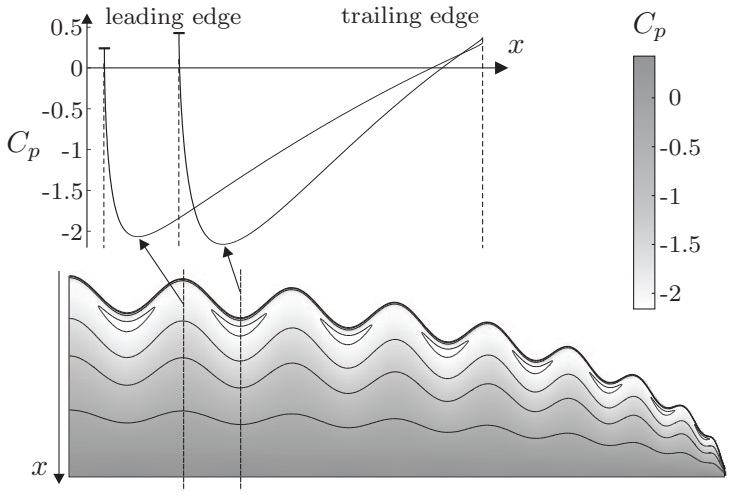


Figure 4.2: (a) Calculated pressure profiles on top of a typical bump and trough and (b) calculated pressure distribution on the top of a bumpy wing. Note the pressure minimum in the troughs near the leading edge. Here, $\alpha = 6°$, $\eta = 0.1$.

at each cross section,

$$L = -\rho\, U_0 \int_{-s}^{s} \Gamma(y)\, \mathrm{d}y. \tag{4.4}$$

This model of a smooth elliptic wing predicts that the lift increases continuously with angle of attack (Batchelor 1992). The top surface of the wing has an adverse pressure gradient $p_x = \mathrm{d}p/\mathrm{d}x > 0$ over a large part of the wing, since pressure is minimum near the leading edge where the flow velocity $u(x)$ is maximum, and then increases towards the trailing edge. As $\alpha$ increases, the magnitude of this adverse pressure gradient also increases, until at a critical angle of attack the boundary layer separates over a large part of the wing, and the wing stalls (Thwaites 1960). For angles of attack above this critical angle the lift on the wing is severely reduced. Experimentally, for a smooth flipper with $s = 3.6$ m and $t/c = 0.23$, the critical angle is approximately 12° (Miklosovic *et al.* 2004). At stall, the lift-coefficient $C_L = L/(\frac{1}{2}\rho U_0^2)$ on a wing section drops to about 0.6 (Johari *et al.* 2007), and results mainly

from the vertical component of form drag.

### 4.2.2 Bumpy wing

How are the aerodynamic characteristics of the wing changed when bumps are added? To investigate this we analyze our model with a spanwise oscillating chord, and solve the integral equation (4.1)-(4.3) both numerically and by a series perturbation. The latter allows us to clarify the relative roles of the physical parameters in the problem (e.g. bump amplitude, wavelength, thickness/chord, etc.). We define the chord as $c(\theta) = c_0 \sin\theta\,(1+\eta\,S)$ where $\eta$ is the amplitude of the bumps and $S = \frac{1}{c_0}\sum_{k=1}^{\infty} a_k \cos(k\,\theta)$ describes the perturbation of the wing from a smooth elliptical wing. Simultaneously expanding the effective angle of attack and circulation in orders of thickness/chord ratio $T = \frac{4}{3\sqrt{3}}\,t_0/c_0$ and bump amplitude $\eta$,

$$\begin{aligned} \alpha^e(\theta) &= \alpha^e_{0,0} + \eta\,\alpha^e_{1,0} + T\,\alpha^e_{0,1} + \eta\,T\,\alpha^e_{1,1} + \ldots \\ \Gamma(\theta) &= \Gamma_{0,0} + \eta\,\Gamma_{1,0} + T\,\Gamma_{0,1} + \eta\,T\,\Gamma_{1,1} + \ldots, \end{aligned} \tag{4.5}$$

where $\alpha^e$ is expressed as a Chebyshev series at each order of $\eta$ and $T$,

$$\alpha^e_{i,j} = \sum_{q=1}^{\infty} b_q^{i,j} \frac{\sin q\,\theta}{\sin\theta}, \tag{4.6}$$

and using (4.1) it can be shown that

$$\begin{aligned} \Gamma_{0,0} &= -\pi U_0 c_0 \alpha^e_{0,0}; \quad \Gamma_{1,0} = -\pi U_0 c_0 (\alpha^e_{1,0} + S(\theta)\alpha^e_{0,0}); \\ \Gamma_{0,1} &= -\pi U_0 c_0 (\alpha^e_{0,1} + \alpha^e_{0,0}); \quad \text{etc.} \end{aligned} \tag{4.7}$$

These equations can be solved to any desired order of $\eta$ and/or $T$. We mention the resulting coefficients $b_q^{i,j}$ here to first order (in subsequent calculations we go to

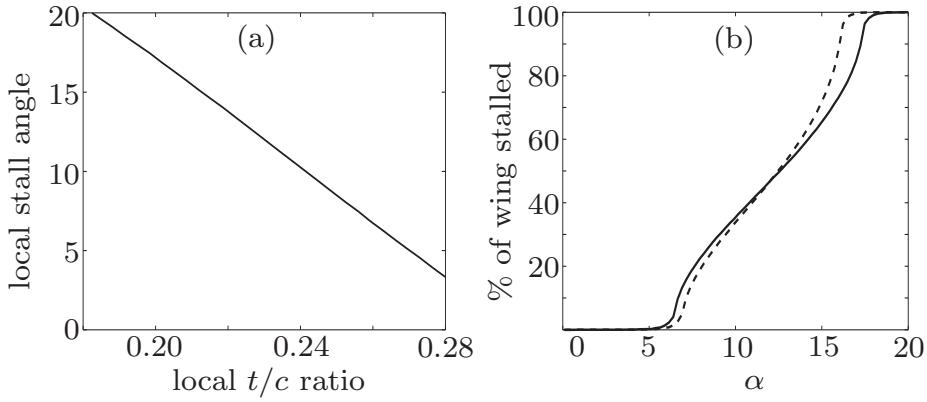


Figure 4.3: (a) Local stall angle on a wing section calculated as a function of thickness to chord ratio, showing a monotonic decrease. (b) Percentage of wing area in stall for: (dashed line) uniform downwash terms, i.e. including $\alpha^e_{0,0}$ and $\alpha^e_{0,1}$ in (4.6) only and neglecting the influence of the bumps in the downwash; (solid line) full downwash including all $\alpha^e_{i,j}$ and thus the influence of the bumps ($\eta = 0.1$, $s = 3.6$ m, $k = 36$).

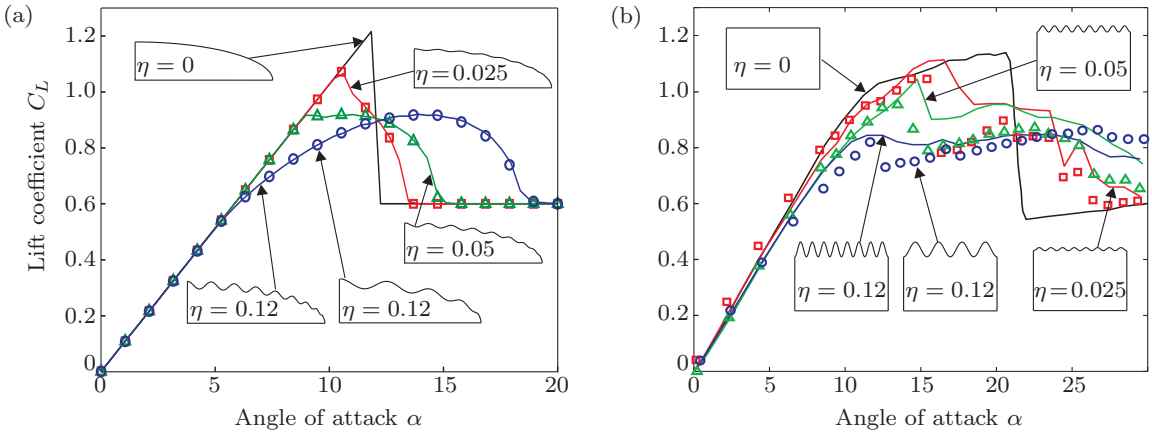


Figure 4.4: Lift curves from (a) our model and (b) wind tunnel data for wing sections from Johari *et al.* (2007). In both figures the black solid line corresponds to the base case, unperturbed wing; the other solid lines correspond to 8 bumps on the wing / section, while open symbols correspond to 4 bumps on a wing / section. Amplitudes are color coded: red $\eta = 0.025$; green $\eta = 0.05$; blue $\eta = 0.12$. In both (a) and (b), planform sketches are included for $\eta = 0, 0.025, 0.05$ and 0.12 for 8 bumps on a wing / section ($k = 36$), and only $\eta = 0.12$ for 4 bumps on a wing / section ($k = 18$).

second order, i.e. $O(\eta^2, T^2, \eta T)$),

$$\begin{aligned} b_1^{0,0} &= \frac{\alpha}{1+\frac{\pi c_0}{4s}}, & \text{all other } b_q^{0,0} = 0 \\ b_1^{0,1} &= -\frac{\pi c_0}{4s}\frac{b_1^{0,0}}{1+\frac{\pi c_0}{4s}} & \text{all other } b_q^{0,1} = 0 \\ b_1^{1,0} &= 0, & b_{q>1}^{1,0} = -\frac{\pi\, q}{8s}\, b_1^{0,0}\, \frac{a_{(q-1)\geq 1} - a_{q+1}}{1+q\frac{\pi c_0}{4s}}. \end{aligned}$$

This series perturbation reproduces the aforementioned result that lift is proportional to $\alpha$ for an elliptic wing for which only $b_1^{0,0}$ and $b_1^{0,1}$ are relevant. Also note how the role of wavelength $\lambda$ is introduced through the coefficients $b_{q>1}^{1,0}$, since $\lambda = 4s/q$. We restrict the choice of bump amplitude and wavelength to keep the total planform area constant.

**Limit of validity**

Since (4.3) is valid for a high aspect ratio wing (ratio of span to mean chord), errors are minimal as long as $s\,\frac{dC_L}{dy} \ll 1$ (Thwaites 1960). In our notation, this criterion becomes

$$4\pi \frac{\eta\,\alpha}{\sin\theta}\frac{s}{\lambda} \ll 1. \tag{4.8}$$

This model therefore operates in the small amplitude, small angle of attack, and long wavelength limit; errors are introduced near the tip where $\sin\theta$ is small.

### 4.2.3 Separation and stall

Figure 4.2 shows pressure contours for the top surface of a bumpy wing. Since neighboring bumps and troughs have similar thicknesses but different chords, the same pressure difference must be overcome over a shorter distance behind a trough

than behind a bump. Hence the pressure gradient is more adverse behind troughs than behind bumps, and separation occurs first behind troughs.

Given the location of the separation point, we transpose the stall criterion from a smooth wing to a bumpy wing. We use a well known criterion for turbulent boundary layer separation to compute the location of the separation point $x_s$ (Stratford 1959; Curle & Davies 1968; Takada 1975). Using the non-dimensional pressure coefficient $C_p = p(x)/(\frac{1}{2}\rho U_0^2)$, the criterion reads

$$F(x) = C_p \left( x \frac{\mathrm{d}C_p}{\mathrm{d}x} \right)^{1/2} \left( 10^{-6} R_e \right)^{-1/10} \tag{4.9}$$

where if $\max(F(x)) \geq 0.40$, then $F(x_s) = 0.40$; if $0.35 \leq \max(F(x)) < 0.40$, then $F(x_s) = \max(F(x))$ and finally if $\max(F(x)) < 0.35$, then separation does not occur. Note that the pressure coefficient $C_p$ depends on $x$, as well as the Reynolds number which is defined as $R_e = U_0\, x/\nu$. This criterion was originally derived by matching an arbitrary imposed outer flow to the flow in the boundary layer, where the overall flow is assumed to be turbulent. Flow separation starts at the trailing edge and creeps forward with increasing angle of attack, in accordance with experiments. Any reasonable separation criterion will lead to the same qualitative flow features. The strength of this particular criterion is that it does not require detailed knowledge of the flow in the boundary layer.

We thus find $(x_s/c)_{\text{elliptic}}$ for a smooth wing at stall ($\alpha = 12°$). To calculate when a bumpy wing is stalled, we assume that if at any cross section of the wing $x_s/c < (x_s/c)_{\text{elliptic}}$, this section is stalled. Sections stall independently of neighboring sections, which is reasonable in the long-wavelength limit since the flow is then predominantly chordwise and the cause of separation / stall will be the upstream flow

rather than the flow in neighboring sections. Behind troughs the adverse pressure gradient is larger, and $x_s$ is closer to the leading edge; therefore troughs stall at a lower angle of attack than the bumps.

In fact, the model shows that there is a strong relationship between the local thickness to chord ratio ($t/c$) and the local stall angle, as shown in figure 4.3(a). The bumps, with relatively small $t/c$, stall at higher angles of attack. Total lift on a partially stalled wing is computed by summing the lift at each cross section, where stalled sections contribute through the vertical component of the form drag as described before. The choice of post-stall lift characteristics is an empirical input into the model. Calculations show that the model is not very sensitive to these post-stall characteristics. Using a constant $C_L = 0.6$ as in figure 4.4(a) or a more complex behavior resembling e.g. the NACA 0018 post-stall lift curve (Goett & Bullivant 1939) does not significantly alter the results.

We thus obtain the lift curve shown in figure 4.4(a), which may be compared with data from Johari *et al.* (2007) as shown in figure 4.4(b). By design, the model shows a smooth wing stalling quite suddenly at $\alpha = 12°$. For small amplitude perturbations ($\eta$) of this smooth wing, the transition to stall becomes slightly less abrupt, and for large $\eta$ much of the wing near the troughs will be in stall at smaller angles of attack, so that the maximum lift coefficient of a smooth wing is never reached. Conversely, in order for the entire wing to be in stall even the most slender section near the bumps must stall. Hence the overall stall angle of the wing increases, in line with the experimental results. According to Fish & Battle (1995), a typical humpback whale flipper has $\eta \approx 0.06$. For such amplitudes the lift curve flattens out at a fairly

high $C_L$, and remains high until stall finally sets in at an angle of attack that is considerably larger than the stall angle of a smooth wing. Our model shows that the wavelength of the bumps has very little influence while the amplitude dominates the lift characteristics of a wing (figure 4.4); the wind tunnel data show a small dependence on wavelength.

## 4.3 Discussion

There are two contributions to the flattening of the lift curve. First, by averaging a distribution of thickness/chord ratios along the wing, the lift curve is flattened out as the trough-sections stall at lower angles of attack than the peak-sections, independent of the global flow coupling. A further flattening is caused by the global coupling between different wing sections that determine downwash as in (4.3). We may separate downwash into a spanwise uniform component which occurs for a smooth wing (i.e. including $\alpha^e_{0,0}$ and $\alpha^e_{0,1}$ in (4.6)) and an additional nonuniform component due to bumpiness (all other $\alpha^e_{i,j}$). In figure 4.3(b) we compare the proportion of wing area in stall with and without the nonuniform downwash component, and find that nonuniform downwash contributes to stall delay. The downwash is larger at the bumps relative to the troughs, leading to a decrease in effective angle of attack (see (4.2)), further delaying stall for the bumps. As a result, peak lift is decreased, but total stall is delayed until larger angles of attack. The variations in downwash along the wing are significant, especially when the wing is nearly in stall (see fig. 4.3(b)).

In addition to predicting delayed stall, our calculations agree with many other aspects of the experiments. The observation that flow separation occurs first behind

troughs is supported by wind tunnel experiments by Johari *et al.* (2007) and simulations by Fish & Lauder (2006). The pressure contours in figure 4.2 predict that absolute pressure is lowest in troughs; water tunnel experiments show cavitation occurring there first (Lebental 2006). Regarding drag, early simulations by Watts & Fish (2001) and wind tunnel experiments suggested that bumpy wings might generate slightly more lift than smooth wings, and lower drag at angles of attack larger than the stall angle of a smooth wing. Our calculations do not show any appreciable difference in the induced drag generated by bumpy wings, but for short enough wavelengths, a very slight improvement in $L/D_i$ can be observed, never much larger than 0.1% (see §4.4).

In conclusion, we note that our aerodynamic model captures the main features exhibited by wing section experiments, namely a more gradual stall and a higher overall stall angle. The original experiments by Miklosovic *et al.* (2004) showed a larger maximum lift coefficient and a somewhat sudden stall; neither our model nor the experimental work on wing sections reproduce these features. This discrepancy may be due to tip effects which cannot occur in the wing section experiments of Johari *et al.* (2007), and cannot be described accurately by our current model due to the approximation in (4.8). Future work should address these tip effects, as well as the potential role of leading edge vortices if these are found to be present.

It remains an open question why only humpback whales are observed to have these leading-edge bumps, and if indeed they are beneficial for the species. Gradual stalling and larger overall stall angles increase the range of $\alpha$ over which a wing or flipper contribute to maneuverability, while decreasing the unpredictability of lift forces near

the stall transition. It is possible that the lessons learned from humpback whale flippers will soon find their way into the design of special purpose wings, hydrofoils, as well as wind turbine and helicopter blades.

## 4.4 Details of Flipper Calculations

### 4.4.1 Flipper parameters

Parameterizing the flipper by $\theta$ as sketched in figure 4.1(b), the chord $c$ is given at each spanwise location $y = s\cos\theta$ by

$$c(\theta) = \sin\theta\left(c_0 + \eta\sum_{k=1}^{\infty} a_k \cos(k\theta)\right) = c_0 \sin\theta\,(1 + \eta S) \tag{4.10}$$

where $S = \frac{1}{c_0}\sum_{k=1}^{\infty} a_k \cos(k\theta)$ describes the perturbation of the flipper from an elliptical smooth flipper. For comparison of the performance of various perturbations, the planform area of the flipper must be kept constant, i.e.

$$\text{Area} = \int_0^s c(y)\,\mathrm{d}y = \int_0^{\pi/2} c(\theta)\, s\, \sin\theta\,\mathrm{d}\theta = \frac{\pi}{4}\, c_0\, s. \tag{4.11}$$

This restricts the choices of $k$ and $\eta$. In particular, any even value of $k$ will satisfy this condition, regardless of the associated $a_k$, except for $k = 2$.

The thickness $t$ of the flipper tapers off towards the tip, i.e. $t = t_0 \sin\theta$ where $t_0$ is the thickness at the root of the flipper such that a smooth elliptic flipper would have the same thickness/chord ratio at every spanwise section. Each flipper section profile is taken to be a Joukowski profile: If $z = (r + \lambda)\exp(i\gamma) - \lambda$ describes a circle in the $z$-plane of radius $(r + \lambda)$ and parameterized by $\gamma$, this maps to a symmetric

flipper profile in the $Z$ plane by the conformal map $Z = z + r^2/z$ (Acheson 1990). The chord $c$ and the thickness $t$ are related to the parameters $r$ and $\lambda$ as

$$c = 4r\frac{(1+\varepsilon)^2}{1+2\varepsilon} \tag{4.12}$$

$$t = 3\sqrt{3}\,\lambda\left(1-\varepsilon+\frac{7}{4}\varepsilon^2+O\left(\varepsilon^3\right)\right) \tag{4.13}$$

where $\varepsilon = \lambda/r$. Since we solve for the flow and circulation around the profile using $(\varepsilon, \lambda, r)$, but use experimental data $(t, c)$, we need to find $\varepsilon$ in terms of $t/c$,

$$\varepsilon = tc + tc^2 + \frac{5}{4}tc^3 + \frac{3}{2}tc^4 + O(tc^5) \tag{4.14}$$

where $tc = \frac{4}{3\sqrt{3}}\frac{t}{c}$. The flipper geometry is now completely determined in terms of known variables.

### 4.4.2 Derivation of circulation

The complex potential for flow around a circle (in the $z$-plane) at some angle of attack $\alpha^e$ and with some circulation at the circle's perimeter of strength $\Gamma$ is (Acheson 1990)

$$\mathrm{w}(z) = U_0\left[(z+\lambda)e^{-i\alpha^e} + \frac{(r+\lambda)^2}{z+\lambda}e^{i\alpha^e}\right] - \frac{i\Gamma}{2\pi}\ln(z+\lambda), \tag{4.15}$$

from which we find the flow velocity around the Joukowski profile using $U - iV = \mathrm{d\,w}/\mathrm{d}Z$, where $U$ and $V$ are the velocity components in the $x$ and $y$ direction respec-

tively. Solving for the flow on the surface of the flipper (parameterized by $\gamma$),

$$\begin{aligned} u(\gamma) &= \frac{H(\gamma)}{|G(\gamma)|}, \quad \text{where} && (4.16) \\ H(\gamma) &= -\frac{\Gamma}{2\pi(r+\lambda)} - 2U\sin(\alpha_e - \gamma), \quad \text{and} \\ G(\gamma) &= 1 - \frac{r^2}{z^2}. && (4.17) \end{aligned}$$

Applying the Kutta condition, which requires $u$ to be finite at the trailing edge ($\gamma = 0$), we find that the numerator ($H$) must be zero at the trailing edge. This determines the circulation around a Joukowski profile,

$$\Gamma(\theta) = -4\pi(r+\lambda)U_0 \sin\alpha^e \tag{4.18}$$

where $\alpha^e = \alpha - \frac{w}{U_0}$ by geometrical considerations (Acheson 1990). Expanding $\sin(\alpha^e) = \alpha^e + O\left((\alpha^e)^3\right)$ and $4(r+\lambda) = c_0 \sin\theta(1 + T + \eta S) + O(T^3)$ where $T = \frac{4}{3\sqrt{3}}\frac{t_0}{c_0}$, we obtain

$$\Gamma(\theta) = -\pi c_0 U_0 (1 + T + \eta S)\,\alpha^e. \tag{4.19}$$

where $c_0 = c_0 \sin\theta$. Note that this expression for circulation is correct to order $O\left((\alpha^e)^3, T^3\right)$.

### 4.4.3 Solving the integral equation

In order to solve the integral equations (4.1)-(4.3), we expand the effective angle of attack $\alpha^e = w(\theta)$ as a Chebyshev series,

$$\alpha^e(\theta) = \alpha - \frac{w}{U_0} = \sum_{p=1}^{\infty} b_p \frac{\sin p\,\theta}{\sin\theta}. \tag{4.20}$$

As a result, circulation is also expressed as a Chebyshev series with different prefactors. Proceeding, we fill in this general form of $\alpha^e(\theta)$ into $\Gamma(\theta)$, then calculate

$$w(\theta) = \frac{-1}{4\pi s}\int_0^\pi \frac{\mathrm{d}\Gamma/\mathrm{d}\theta'}{\cos\theta' - \cos\theta}\,\mathrm{d}\theta', \tag{4.21}$$

and using the identity (Mason & Handscomb 2002)

$$\frac{1}{\pi}\int_0^\pi \frac{\cos m\theta'}{\cos\theta' - \cos\theta}\,\mathrm{d}\theta' = \frac{\sin m\,\theta}{\sin\theta}, \tag{4.22}$$

we obtain a matrix equation which can be solved numerically for the coefficients $b_p$.

We also solve the integral equation by a series perturbation. Simultaneously expanding downwash and circulation in orders of thickness/chord ratio $T$ and bump amplitude $\eta$:

$$\begin{aligned} \alpha^e(\theta) &= \alpha^e_{0,0} + \eta\,\alpha^e_{1,0} + T\,\alpha^e_{0,1} + \eta\,T\,\alpha^e_{1,1} + \ldots \\ \Gamma(\theta) &= \Gamma_{0,0} + \eta\,\Gamma_{1,0} + T\,\Gamma_{0,1} + \eta\,T\,\Gamma_{1,1} + \ldots, \end{aligned} \tag{4.23}$$

where

$$\alpha^e_{i,j} = \sum_{p=1}^{\infty} b_p^{i,j}\frac{\sin p\,\theta}{\sin\theta} \tag{4.24}$$

and using (4.19) it can be shown that

$$\begin{aligned} \Gamma_{0,0} &= -\pi U_0 c_0 \alpha^e_{0,0}; \quad \Gamma_{1,0} = -\pi U_0 c_0(\alpha^e_{1,0} + S(\theta)\alpha^e_{0,0}); \\ \Gamma_{0,1} &= -\pi U_0 c_0(\alpha^e_{0,1} + \alpha^e_{0,0}); \quad \text{etc.} \end{aligned} \tag{4.25}$$

These equations can be solved to any desired order of $\eta$ and/or $T$. We mention the resulting coefficients $b_p^{i,j}$ here to first order (in subsequent calculations we go to second

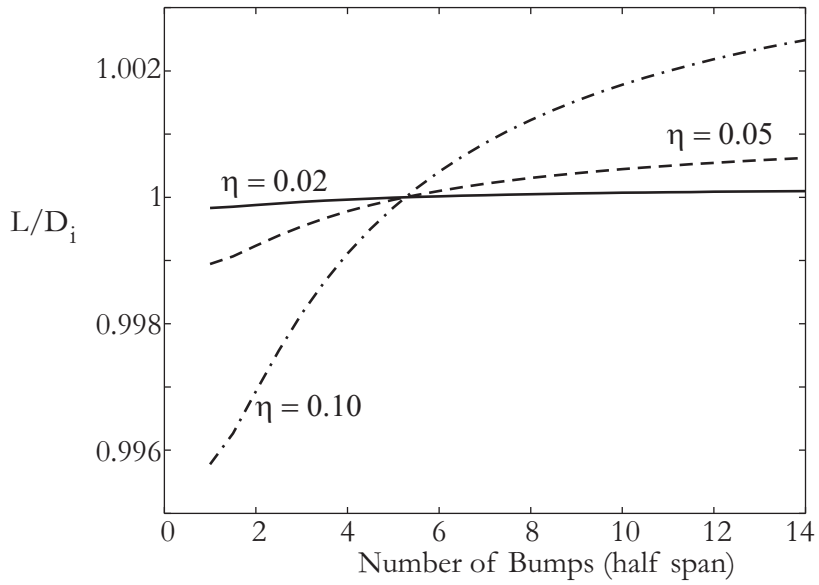


Figure 4.5: Lift-to-drag ratio dependence on wavenumber (expressed here as number of bumps on one flipper, i.e. half the span). $L/D$ has been normalized by $L/D$ for a smooth flipper of finite thickness. Solid line: $\eta = 0.02$, dashed line: $\eta = 0.05$, dash-dot line: $\eta = 0.1$.

order, i.e. $O(\eta^2, T^2, \eta T)$),

$$\begin{aligned} b_1^{0,0} &= \frac{\alpha}{1+\frac{\pi c_0}{4s}}, \qquad \text{all other } b_p^{0,0} = 0 \\ b_1^{0,1} &= -\frac{\pi c_0}{4s}\frac{b_1^{0,0}}{1+\frac{\pi c_0}{4s}} \qquad \text{all other } b_p^{0,1} = 0 \\ b_1^{1,0} &= 0, \qquad b_{p>1}^{1,0} = -\frac{\pi\, p}{8s}\, b_1^{0,0}\, \frac{a_{(p-1)\geq 1} - a_{p+1}}{1+p\frac{\pi c_0}{4s}}. \end{aligned}$$

### 4.4.4 Lift, induced drag

From the previous analysis, we can calculate lift and drag to any order of $\eta$ or $T$. Starting with lift,

$$L = -\rho U_0 \int_{-s}^{s} \Gamma \, \mathrm{d}y = L_{0,0} + \eta L_{1,0} + T L_{0,1} + \eta T L_{1,1} + \ldots \tag{4.26}$$

where

$$\begin{aligned} L_{0,0} &= \frac{1}{2}\rho U^2 \pi^2 c_0\, s\, b_1^{0,0}, \quad L_{1,0} = L_{1,1} = 0, \\ L_{0,1} &= L_{0,0}\frac{1}{1+\delta}, \qquad L_{0,2} = -L_{0,1}\frac{\delta}{1+\delta}, \\ \text{and} \quad L_{2,0} &= L_{0,0}\; f(a_k, k, \delta) \end{aligned}$$

where $\delta = \frac{c_0 \pi}{4s}$, which is a measure of the inverse aspect ratio of the flipper, and $k$ is the wavenumber of the perturbation (wavelength of bumps $\lambda = 4s/k$, number of bumps on one flipper is $k/4$).

Induced drag is calculated as

$$D_i = -\rho U_0 \int_{-s}^{s} \Gamma\, w(y)\, \mathrm{d}y = D_{0,0} + \eta D_{1,0} + T D_{0,1} + \ldots \tag{4.27}$$

where

$$\begin{aligned} D_{0,0} &= (\alpha - b_1^{0,0}) L_{0,0}, \quad D_{1,0} = D_{1,1} = 0, \\ D_{0,1} &= 2D_{0,0}\frac{1}{1+\delta}, \qquad D_{0,2} = -D_{0,1}\frac{1-2\delta}{1+\delta}, \\ \text{and} \quad D_{2,0} &= D_{0,0}\; g(a_k, k, \delta). \end{aligned}$$

From lift and induced drag, we calculate $L/D_i$, which determines the lifting performance of the flipper. When compared to $L/D_i$ for a smooth flipper, it is notable that performance is decreased for a small number of bumps (long wavelength), but increased slightly for shorter wavelengths; the changes scaling with $\eta^2$ (see figure 4.5). Note that the numbers are very small, there is at most a 0.2% improvement, and this is only including induced drag (i.e. not form drag or skin friction drag).

# Bibliography


Acheson, D. J. 1990 *Elementary Fluid Dynamics*. Oxford: Clarendon Press.

Adelizzi, E. A. & Troian, S. M. 2004 Interfacial slip in entrained soap films containing associating hydrosoluble polymer. *Langmuir* **20**, 7482–7492.

Afsar-Siddiqui, A.B., Luckham, P.F. & Matar, O.K. 2003 The spreading of surfactant solutions on thin liquid films. *Adv. Coll. and Int. Sci.* **106**, 183.

Amarouchene, Y., Bonn, D., Meunier, J. & Kellay, H. 2001 Inhibition of the finite-time singularity during droplet fission of a polymeric fluid. *Phys. Rev. Lett.* **86**, 3558–3561.

Bacri, L., Debrégeas, G. & Brochard-Wyart, F. 1996 Experimental study of the spreading of a viscous droplet on a nonviscous liquid. *Langmuir* **12**, 6708.

Bailey, F. E. & Koleske, J. V. 1976 *Poly(ethylene oxide)*. New York: Academic Press.

Batchelor, G. K. 1992 *An Introduction to Fluid Dynamics*. Cambridge: University Press.

Berg, S., Adelizzi, E. A. & Troian, S. M. 2005 Experimental study of entrainment and drainage flows in microscale soap films. *Langmuir* **21**, 3867–3876.

Braun, R. J., Murray, B. T., Boettinger, W. J. & McFadden, G. B. 1995 Lubrication theory for reactive spreading of a thin drop. *Phys. Fluids* **7**, 1797.

Breward, C. J. W. 1999 The mathematics of foam. PhD thesis, Oxford University.

Breward, C. J. W. & Howell, P. D. 2002 The drainage of a foam lamella. *J. Fluid Mech.* **458**, 379–406.

Brochard-Wyart, F., Martin, P. & Redon, C. 1993 Liquid/liquid dewetting. *Langmuir* **9**, 3682.

Bruinsma, R., di Meglio, J. M., Quéré, D. & Cohen-Addad, S. 1992 Formation of soap films from polymer solutions. *Langmuir* **8**, 3161–3167.

Chari, K., Antalek, B., Lin, M. Y. & Sinha, S. K. 1994 The viscosity of polymer-surfactant mixtures in water. *J. Chem. Phys.* **100**, 5294–5300.

Chowdhury, D., Sarkar, S. P., Kalita, D., Sarma, T. K., Paul, A. & Chattopadhyay, A. 2004 Spreading and recoil of a surfactant-containing water drop on glass-supported alcohol films. *Langmuir* **20**, 1251.

Cohen-Addad, S. & di Meglio, J.-M. 1994 Stabilization of aqueous foam by hydrosoluble polymers 2. Role of polymer/surfactant interactions. *Langmuir* **10**, 773–778.

Cooper-White, J. J., Crooks, R. C., Chockalingam, K. & Boger, D. V. 2002 Dynamics of polymer-surfactant complexes: elongational properties and drop impact behaviour. *Ind. Eng. Chem. Res.* **41**, 6443–6459.

Curle, N. & Davies, H. J. 1968 *Modern Fluid Dynamics, Vol 1.: Incompressible Flow*. London: Van Nostrand.

Devanand, K. & Selser, J. C. 1991 Asymptotic behavior and long-range interactions in aqueous solutions of poly(ethylene oxide). *Macromolecules* **24**, 5943–5947.

Durand, M. & Stone, H. A. 2006 Relaxation time of the topological T1 process in a two-dimensional foam. *Phys. Rev. Lett.* **97**, 226101.

Dussaud, A. D., Troian, S. M. & Harris, S. R. 1998 Fluorescence visualization of a convective instability which modulates the spreading of volatile surface films. *Phys. Fluids* **10**, 1588.

Edwards, D. A., Brenner, H. & Wasan, D. T. 1991 *Interfacial Transport Processes and Rheology*. Boston: Butterworth-Heinemann.

Fernandez, J. M. & Homsy, G. M. 2003 Viscous fingering with chemical reaction: effect of in-situ production of surfactants. *J. Fluid Mech.* **480**, 267.

Fernandez, J. M. & Homsy, G. M. 2004 Chemical reaction-driven tip-streaming phenomena in a pendant drop. *Phys. Fluids* **16**, 2548.

Fish, F. E. & Battle, J. M. 1995 Hydrodynamic design of the humpback whale flipper. *J. Morphology* **225**, 51.

Fish, F. E. & Lauder, G. V. 2006 Passive and active flow control by swimming fishes and mammals. *Annu. Rev. Fluid Mech.* **38**, 193–224.

Foda, M. & Cox, R. G. 1980 The spreading of thin liquid films on a water-air interface. *J. Fluid Mech.* **101**, 33.

Francois, J., Dayantis, J. & Sabbadin, J. 1985 Hydrodynamical behaviour of the poly(ethylene oxide)-sodium dodecylsulphate complex. *Eur. Polym. J.* **21**, 165–174.

Fruhner, H., Wantke, K.-D. & Lunkenheimer, K. 1999 Relationship between surface dilational properties and foam stability. *Colloids Surfaces A* **162**, 193–202.

Gaver, D. P. & Grotberg, J. B. 1992 Droplet spreading on a thin viscous film. *J. Fluid Mech.* **235**, 399.

Geethakrishnan, T. & Palanisamy, P. K. 2006 Optical phase-conjugation in erioglaucine dye-doped thin film. *Pramana - J. Phys.* **66**, 473 – 478.

de Gennes, P. G. 1985 Wetting: statics and dynamics. *Rev. Mod. Phys.* **57**, 827.

de Gennes, P. G., Brochard-Wyart, F. & Quéré, D. 2004 *Capillarity and Wetting Phenomena: Drops, Bubbles, Pearls, Waves*. New York: Springer-Verlag.

Gilányi, T., Varga, I., Gilányi, M. & Mészáros, R. 2006 Adsorption of poly(ethylene oxide) at the air/water interface: a dynamic and static surface tension study. *J. Colloid Interf. Sci.* **301**, 428 – 435.

Goett, H. J. & Bullivant, W. K. 1939 Tests of NACA 0009, 0012, and 0017 airfoils in the full-scale tunnel. *Tech. Rep.* NACA-TR-647. NASA.

Goudeseune, C. 2006 Put teeth on it and take a bite out of your airplane's stall. *Quiet Flyer* **11**, 18.

Graessley, W. W. 1980 Polymer chain dimensions and the dependence of viscoelastic properties on concentration, molecular weight and solvent power. *Polymer* **21**, 258–262.

Greffier, O., Amarouchene, Y. & Kellay, H. 2002 Thickness fluctuations in turbulent soap films. *Phys. Rev. Lett.* **88**, 194101.

Hain, J. H. W., Carter, G. R., Kraus, S. D., Mayo, C. A. & Winn, H. E. 1982 Feeding behaviour of the humpback whale, *Megaptera Novaeangliae*, in the western north atlantic. *Fish. Bull.* **80**, 259.

Heo, Y. & Larson, R. G. 2005 The scaling of zero-shear viscosities of semidilute polymer solutions with concentration. *J. Rheol.* **49**, 1117–1128.

Howell, P. D., Wylie, J. J., Huang, H. & Miura, R. M. 2007 Stretching of heated threads with temperature-dependent viscosity: asymptotic analysis. *Discrete Cont. Dyn.-B* **7**, 553–572.

Hua, X. Y. & Rosen, M. J. 1988 Dynamic surface tension of aqueous surfactant solutions. *J. Colloid Interf. Sci.* **124**, 652–659.

Hutzler, S., Verbist, G., Weaire, D. & van der Steen, J. A. 1995 Measurement of foam density profiles using AC capacitance. *Europhys. Lett.* **31**, 497.

Isenberg, C. 1992 *The Science of Soap Films and Soap Bubbles*. New York: Dover Publications.

Jensen, O.E. 1994 Self-similar, surfactant-driven flows. *Phys. Fluids* **6**, 1084.

Johari, H., Henoch, C., Custodio, D. & Levshin, A. 2007 Effects of leading-edge protuberences on airfoil performance. *AIAA Journal* **45**, 2634.

Lal, J. & di Meglio, J.-M. 1994 Formation of soap films from insoluble surfactants. *J. Colloid Interf. Sci.* **164**, 506–509.

Lance-Gomez, E. T. & Ward, T. C. 1986 Viscoelastic character of poly(ethylene oxide) in aqueous solutions: effect of shear rate, concentration, salt, and anionic surfactant. *J. Appl. Polym. Sci.* **31**, 333–340.

Lebental, S. 2006 Cavitation onset prediction and verification on rudders with leading edge tubercles. Master's thesis, Duke University.

Lee, J. K. & Berman, N. S. 1996 Tensile stress measurements of dilute polymer solutions containing traces of salts and dyes. *J. Rheol.* **40**, 1015–1025.

Lionti-Addad, S. & di Meglio, J.-M. 1992 Stabilization of aqueous foam by hydrosoluble polymers 1. Sodium dodecyl sulfate – poly(ethylene oxide) system. *Langmuir* **8**, 324–327.

Lister, J. R. & Kerr, R. C. 1989 The propagation of two-dimensional and axisymmetirc viscous gravity curents at a fluid interface. *J. Fluid Mech.* **203**, 215.

Liu, X. & Duncan, J. H. 2006 An experimental study of surfactant effects on spilling breakers. *J. Fluid Mech.* **567**, 433–455.

Mason, J. C. & Handscomb, D. C. 2002 *Chebyshev Polynomials*. New York: Chapman & Hall/CRC.

Miklosovic, D. S., Murray, M. M., Howle, L. E. & Fish, F. E. 2004 Leading-edge tubercles delay stall on humpback whale (megaptera novaeangliae) flippers. *Phys. Fluids* **16**, L39.

Mysels, K. J. & Cox, M. C. 1962 An experimental test of Frankel's law of film thickness. *J. Colloid Sci.* **17**, 136–145.

Mysels, K. J., Shinoda, K. & Frankel, S. 1959 *Soap Films: Studies of Their Thinning*. New York: Pergamon Press.

Naire, S., Braun, R. J. & Snow, S. A. 2001 An insoluble surfactant model for a vertical draining free film with variable surface viscosity. *Phys. Fluids* **13**, 2492–2502.

van Nierop, E. A., Ajdari, A. & Stone, H. A. 2006 Reactive spreading and recoil of oil on water. *Phys. Fluids* **18**, 038105.

van Nierop, E. A., Alben, S. & Brenner, M. P. 2008*a* How bumps on whale flippers delay stall: an aerodynamic model. *Phys. Rev. Lett.* **100**, 054502.

van Nierop, E. A., Scheid, B. & Stone, H. A. 2008*b* On the thickness of soap films: an alternative to Frankel's law. *J. Fluid Mech.* **602**, 119–127.

Nishiyama, H. & Nakamura, M. 1993 Capacitance of disk capacitors. *IEEE Trans. Comp., Hybrids, Manuf. Technol.* **16**, 360.

Ortiz, M., Kee, D. De & Carreau, P. J. 1994 Rheology of concentrated poly(ethylene oxide) solutions. *J. Rheol.* **38**, 519–539.

Péron, N., Mészáros, R., Varga, I. & Gilányi, T. 2007 Competitive adsorption of sodium dodecyl sulfate and polyethylene oxide at the air/water interface. *J. Colloid Interf. Sci.* **313**, 389–397.

Poulard, C., Bénichou, O. & Cazabat, A.M. 2003 Freely receding evaporating droplets. *Langmuir* **19**, 8828.

Ramé, E. 2007 The stagnation point in Marangoni-thickened Landau-Levich type flows. *Phys. Fluids* **19**, 078102–4.

Rubinstein, M. & Colby, R. H. 2003 *Polymer Physics*. Oxford: Oxford University Press.

de Rycke, A. 1997 Fragmentation of a spreading drop. *Europhys. Lett.* **40**, 305.

Scheid, B., Quiligotti, S., Tran, B., Gy, R. & Stone, H. A. 2009 On the (de)stabilization of draw resonance due to cooling. *submitted to J. Fluid Mech.* .

Schwartz, L. W. & Roy, R. V. 1999 Modeling draining flow in mobile and immobile soap films. *J. Colloid Interf. Sci.* **218**, 309–323.

Scriven, L. E. 1960 Dynamics of a fluid interface: Equation of motion for Newtonian surface fluids. *Chem. Eng. Sci.* **12**, 98–108.

Sebba, F. 1975 Macrocluster gas-liquid and biliquid foams and their biological significance. *Adv. in Chem. Series* **9**, 18.

Shen, A. Q., Gleason, B., McKinley, G. H. & Stone, H. A. 2002 Fiber coating with surfactant solutions. *Phys. Fluids* **14**, 4055.

Skoog, D. A. & Leary, J. J. 1992 *Principles of Instrumental Analysis*. New York: Harcourt Brace College Publishers.

Smitter, L. M., Guédez, J. F., Müller, A. J. & Sáez, A. E. 2001 Interactions between poly(ethylene oxide) and sodium dodecyl sulfate in elongational flows. *J. Colloid Interf. Sci.* **236**, 343–353.

Stein, B. & Murray, M. M. 2005 Stall mechanism analysis of humpback whale flipper models. In *Proc. of the Intl. Symp. on Unmanned Untethered Submersible Technol.*. Autonomous Undersea Systems Inst., Durham, New Hampshire.

Stocker, R. & Bush, J. W. M. 2007 Spontaneous oscillations of a sessile lens. *J. Fluid Mech.* **583**, 465475.

Stratford, B. S. 1959 The prediction of separation of the turbulent boundary layer. *J. Fluid Mech.* **5**, 1.

Sumino, Y., Magome, N., Hamada, T. & Yoshikawa, K. 2005 Self-running droplet: emergence of regular motion from nonequilibrium noise. *Phys. Rev. Lett.* **94**, 068301.

Takada, H. 1975 An extension to the critical flow of stratford's theory for predicting the turbulent separation position. *J. Phys. Soc. of Japan* **39**, 1106.

Thwaites, B. 1960 *Incompressible Aerodynamics*. New York: Dover Publications.

Tirtaatmadja, V., McKinley, G. H. & Cooper-White, J. J. 2006 Drop formation and breakup of low viscosity elastic fluids: effects of molecular weight and concentration. *Phys. Fluids* **18**, 043101–18.

Torres, M. F., Müller, A. J., Szidarovszky, M. A. & Sáez, A. E. 2008 Shear and extensional rheology of solutions of mixtures of poly(ethylene oxide) and anionic surfactants in ionic environments. *J. Colloid Interf. Sci.* **326**, 254–260.

Touhami, Y., Hornof, V. & Neale, G.H. 1998 Dynamic interfacial tension behavior of acidified oil/surfactant enhanced alkaline systems 1. experimental studies. *Colloids Surf. A* **132**, 61.

Watts, P. & Fish, F. E. 2001 The influence of passive, leading edge tubercles on wing performance. In *Proc. of the Intl. Symp. on Unmanned Untethered Submersible Technol.*. Autonomous Undersea Systems Inst., Lee, New Hampshire.

Woodward, B. L., Winn, J. P. & Fish, F. E. 2006 Morphological specializations of baleen whales associated with hydrodynamic performance and ecological niche. *J. Morph.* **267**, 1284.